

Chiral symmetry breaking and catalytic effect induced by monopole and instanton creations in QCD

Masayasu Hasegawa^a

Bogoliubov Laboratory of Theoretical Physics, Joint Institute for Nuclear Research, Dubna, Moscow 141980, Russia

Received: date / Revised version: date

Abstract. In QCD, magnetic monopoles are crucial elements for the mechanism of color confinement, and instantons induce spontaneous chiral symmetry breaking. However, showing the relations among the monopoles, instantons, and chiral symmetry breaking is difficult because of the strong interaction in the low-energy QCD. Therefore, we perform numerical simulations and show the relations that experiments can detect. First, we add a monopole and an anti-monopole varying their magnetic charges to the QCD vacua by applying the monopole creation operator. Second, we estimate the monopole and instanton effects on observables using the eigenvalues and eigenvectors of the overlap Dirac operator. Finally, we compare the outcomes with the predictions. In the previous research, we found that the added monopoles and anti-monopoles create instantons and anti-instantons. We have discovered the following effects on the observables by increasing the number density of instantons and anti-instantons. First, the chiral condensate (negative values) decreases. Second, the masses of light quarks and mesons become heavy, and the decay constants of light mesons increase. Third, the decay width of the charged pion becomes wide; therefore, its lifetime becomes short. We have demonstrated quantitative relations among these observables and the number density of instantons and anti-instantons. These results, however, were obtained using the QCD vacuum of one lattice volume of one lattice spacing. Therefore, this research examines the influences of finite lattice volume and discretization. Finally, we obtain the interpolated results at the continuum limit and show the quantitative relations.

PACS. 11.15.Ex Spontaneous breaking of gauge symmetries – 11.15.Ha Lattice gauge theory – 11.30.Rd Chiral symmetries – 12.38.Aw General properties of QCD (dynamics, confinement, etc.) – 12.38.Gc Lattice QCD calculations – 13.20.Cz Decay of π mesons

1 Introduction

There are two interesting phenomena of the low-energy QCD. These are color confinement and chiral symmetry breaking. Proving color confinement is one of the most important assignments in elementary particle physics and nuclear physics [1]. To illuminate the mechanism of color confinement, a great number of studies based on the ideas of the dual superconductor picture of Mandelstam [2] and 't Hooft [3] has already been carried out. The achieved results support the theoretical explanation that magnetic monopoles condensing in QCD vacuum are the key ingredient for causing the dual Meissner effect and confining color-charged particles [4, 5, 6, 7, 8, 9, 10, 11, 12, 13, 14, 15].

Currently, experiments to discover magnetic monopoles have been attempted. In condensed matter physics, a research group makes the Dirac monopole in a Bose-Einstein condensate and observes it [16, 17]. P. A. M. Dirac first referred to an isolated magnetic pole or Dirac monopole in 1931. This outcome shows the possibility that a Dirac monopole exists in the real world.

In high-energy physics, the "Monopole and Exotics Detector at the LHC (MoEDAL)" experiment, which aims to search for magnetic monopoles and other highly-ionizing particles in proton-proton collisions at the Large Hadron Collider (LHC), has begun. The magnetic monopoles that are produced in high-energy collisions were explored [18, 19].

These experiments are significant challenges to advance the frontiers of science.

Spontaneous breaking of chiral symmetry is another interesting phenomenon of the low-energy QCD [20, 21, 22, 23, 24, 25]. When chiral symmetry is spontaneously broken, the NG (Nambu-Goldstone) boson that is the pion appears through the axial-vector current. The chiral condensate is an order parameter of chiral symmetry breaking and has a nonzero value, and the quarks obtain small masses. Once the quarks obtain the masses, the pion obtains the mass from the assumption of PCAC [26].

The instanton [27] is a configuration of QCD that breaks chiral symmetry [28, 29]. The instanton model demonstrates that in the instanton vacuum, the effective mass of a quark is non-zero, and the massless pole of the NG boson appears

^a Present address: hasegawa@theor.jinr.ru

as a pion; moreover, the chiral condensate and the pion decay constant are reasonably estimated from the number density of instantons and anti-instantons in the QCD vacuum [30,31,32,33].

These magnetic monopoles and instantons in the QCD vacuum are strongly tied to each other and are closely related to quarks and gluons in the QCD vacuum. We suppose that the mechanism of color confinement and the spontaneous breaking of chiral symmetry are connected through magnetic monopoles and instantons. Investigating the relations among the magnetic monopoles, instantons, quarks, and gluons by phenomenological calculations is challenging because of the strong interaction in the low-energy region of the QCD. On the other hand, it is fascinating to demonstrate the effects of magnetic monopoles and instantons on physical quantities that can be detected by experiments. Therefore, we first carry out lattice gauge theory simulations and investigate the effects.

In lattice gauge theory, various kinds of research on monopoles and instantons have already been attempted. However, fermions that do not preserve chiral symmetry have been mainly used as quarks.

Accordingly, we carry out numerical calculations using overlap fermions [34,35,36,37,38] that preserve the exact chiral symmetry in lattice gauge theory and quantitatively demonstrate the monopole and instanton effects in QCD on chiral symmetry breaking and hadrons.

First, we add one pair of monopole and anti-monopole with the magnetic charges in the QCD vacuum of the quenched SU(3) by applying the monopole creation operator to the vacuum [39]. We increase the number of monopoles and antimonopoles by varying the monopole and antimonopole magnetic charges and generate QCD vacua. Second, we calculate the eigenvalues and eigenvectors of the overlap Dirac operator using the normal vacua and the vacua with the added monopoles and anti-monopoles. Finally, we compute observables using eigenvalues and eigenvectors and quantitatively evaluate the effects of the monopoles and instantons on the observables by comparing them with the predictions.

In the previous research [39,41], we found that the added monopole with a magnetic charge of +1 and anti-monopole with a magnetic charge of -1 make one instanton or anti-instanton. The value of the chiral condensate, which is an order parameter of symmetry breaking, is defined as a negative number and decreases in direct proportion to the square root of the number density of the instantons and anti-instantons. The light quark masses increase in direct proportion to the square root of the number density of the instantons and anti-instantons. The masses and decay constants of the pion and kaon increase in direct proportion to the one-fourth root of the number density of instantons and anti-instantons. We analytically estimated the catalytic effect on the charged pion using these outcomes as input values. The lifetime of the charged pion becomes shorter than the experimental result because the decay width of the charged pion becomes wider with increasing number density of instantons and

anti-instantons. We have confirmed that these results are consistent with the predictions.

However, we performed simulations using only one lattice of volume $V = 18^3 \times 32$ and parameter $\beta = 6.0522$ for the lattice spacing in our previous research. Therefore, this research aims to inspect the influences of the finite lattice volume and discretization, obtain more precise and reliable results by interpolating to the continuum limit than our previous outcomes, and quantitatively evaluate the effects caused by the monopole and instanton creation in the QCD on the observables.

For this purpose, first, we add the monopole and anti-monopole to the QCD vacua of two different lattice volumes $V = 14^3 \times 28$ ($V_{\text{phys}} = 5.7845 \text{ [fm}^4\text{]}$) and $V = 16^3 \times 32$ ($V_{\text{phys}} = 9.8682 \text{ [fm}^4\text{]}$) of the parameter $\beta = 6.0000$ for the lattice spacing and inspect the effects of the finite lattice volume on the numerical results. The results of $V = 14^4$, $\beta = 6.0000$ have already been reported in our previous research [39].

Next, we set a physical volume to $V_{\text{phys}} = 9.8682 \text{ [fm}^4\text{]}$. We add the monopole and anti-monopole to the QCD vacua of five sets of lattice volumes V and parameters β as follows: (i) $V = 12^3 \times 24$ of $\beta = 5.8457$. (ii) $V = 14^3 \times 28$ of $\beta = 5.9256$. (iii) $V = 16^3 \times 32$ of $\beta = 6.0000$. (The preliminary results were reported in [42].) (iv) $V = 18^3 \times 32$ of $\beta = 6.0522$. (The numerical results were given in [41].) (v) $V = 20^3 \times 40$ of $\beta = 6.1356$. We investigate the discretization influence and interpolate the numerical results obtained using these QCD vacua to the continuum limit. The details of the simulation parameters are in Table 1.

Finally, this article obtains quantitative relations between observables and number density of the instantons and anti-instantons.

The article is composed of six sections, and each content of the section is as follows:

In section 2, we calculate the monopole density and confirm that the monopole creation operator produces monopoles and anti-monopoles. We then compute the number of instantons and anti-instantons created by the added monopoles and anti-monopoles and compare the results with the predictions.

In section 3, we examine the effects of the additional monopoles and anti-monopoles on the spectrum of the overlap Dirac operator by comparing them with the random matrix theory (RMT).

In section 4, we first calculate the correlations of the pseudoscalar density and scalar density and confirm the PCAC relation. We then compute the renormalization constant for the scalar density and evaluate the normalized chiral condensate in the $\overline{\text{MS}}$ at 2 [GeV] using the scale parameter obtained by comparison with chiral random matrix theory (chRMT).

In section 5, to compare the numerical results with the experimental results, we determine the normalization factor for the pion mass and decay constant by matching the numerical results with the experimental outcomes. We re-evaluate the renormalized chiral condensate in the $\overline{\text{MS}}$ -scheme at 2 [GeV] and estimate the average mass of the light quarks in the $\overline{\text{MS}}$ -scheme at 2 [GeV], the pion mass,

Table 1. The simulation parameters. The results of the lattice spacing a are calculated using the analytic formula [40]. The Sommer scale is $r_0 = 0.5$ [fm]. The locations of the monopole and anti-monopole are indicated as the four-dimensional coordinates $(\frac{x}{a}, \frac{y}{a}, \frac{z}{a}, \frac{t}{a})$ in the lattice unit.

β	a [fm]	$V (V_s \times T)$	V_{phys} [fm ⁴]	m_c	Monopole	Anti-monopole	D [fm]
5.8457	0.1242	$12^3 \times 24$	9.8682	0-5	(12, 9.5, 9.5, 6.5)	(12, 3.5, 3.5, 5.5)	1.06
5.9256	0.1065	$14^3 \times 28$	9.8682	0-5	(14, 11.5, 11.5, 7.5)	(14, 4.5, 4.5, 6.5)	1.06
6.0000	9.315×10^{-2}	$14^3 \times 28$	5.7845	0-5	(14, 12.5, 12.5, 8.5)	(14, 4.5, 4.5, 7.5)	1.06
6.0000	9.315×10^{-2}	$16^3 \times 32$	9.8682	0-5	(16, 12.5, 12.5, 8.5)	(16, 4.5, 4.5, 7.5)	1.06
6.0522	8.527×10^{-2}	$18^3 \times 32$	9.8682	0-5	(18, 14.5, 14.5, 9.5)	(18, 5.5, 5.5, 8.5)	1.09
6.1366	7.452×10^{-2}	$20^3 \times 40$	9.8682	4-5	(20, 15.5, 15.5, 10.5)	(20, 5.5, 5.5, 9.5)	1.06

and decay constants. Finally, we evaluate the catalytic effect on the charged pion.

In section 6, we give a summary and conclusions.

We have already presented the preliminary results at the 38th international symposium on lattice field theory [43].

2 Monopoles and instantons

In this section, we first explain the monopole and anti-monopole creation in the QCD vacuum. We then estimate the number of instantons and anti-instantons in the QCD vacuum from the topological charges in the spectrum of the overlap Dirac operator. Finally, we demonstrate increases in the monopole density and instanton density by varying the magnetic charges of monopoles and anti-monopoles.

2.1 The creation of monopoles and anti-monopoles

We generate the normal configurations and the configurations with an additional monopole and an anti-monopole of the quenched SU(3) using the standard techniques of the heat-bath and overrelaxation methods. In this study, a pair of monopoles and anti-monopoles is added by applying the monopole creation operator to the vacuum of the quenched SU(3) by using the same technique as in our previous study [39].

The additional monopole and anti-monopole are three-dimensional objects. The additional monopole has a positive integer charge from 0 to 5, and the additional anti-monopole has a negative integer charge from 0 to -5. The total magnetic charges of the additional monopoles and anti-monopoles are added to the vacuum to be zero. The magnetic charges are varied to increase the numbers of monopoles and anti-monopoles in the vacuum. Hereafter, the magnetic charge m_c indicates that both the magnetic charge m_c of the monopole and the magnetic charge $-m_c$ of the anti-monopole are added.

We put the monopole and anti-monopole on the dual-sites in the spatial volume V_s at the time-slice $\frac{T}{2}$, maintaining the three-dimensional distance D between them to be approximately 1.1 [fm]. T is the time component of the lattice volume V . This proper distance is determined by checking the stability of the density of the monopoles

and anti-monopoles, which is explained in our previous study [39].

We confirm that the added monopole and anti-monopole do not affect the numerical results of the lattice spacing $a^{(1)}$ and $a^{(2)}$, which are calculated from the static potential, as shown in Table 26 in A. Therefore, we use the outcomes of the lattice spacing computed using the analytic formula [40] and Sommer scale $r_0 = 0.5$ [fm] in this study.

The simulation parameters of β for the lattice spacing a , lattice volumes V , magnetic charges m_c , locations of the monopole and anti-monopole, and distances D are given in Table 1.

To confirm whether we correctly add the monopole and anti-monopole to the configurations, we diagonalize the SU(3) matrices under the condition of the maximal Abelian gauge and perform the Abelian projection [44]. We restrain the Gribov copy from influencing the numerical results using the simulated annealing algorithm and analyze the Abelian monopoles.

Our previous study confirmed that the monopole creation operator makes only long monopole loops [39], which condense in the vacua and are closely related to the mechanism of color confinement. We first count the number of monopoles and anti-monopoles that compose the closed long loops C in the four-dimensional volumes V [45]. The monopole is a three-dimensional object. Therefore, we define the three-dimensional number densities of the monopoles and anti-monopoles by counting the number of monopole currents composing the long monopole loops as follows:

$$\rho_m^{\text{long}} \equiv \left(\sum_{i,\mu} \sum_{*n \in C} \frac{|k_\mu^i(*n)|}{12V} \right)^{\frac{3}{4}} [\text{GeV}^3] \quad (1)$$

$k_\mu^i(*n)$ is the monopole current defined on the dual-sites $*n$ [4, 46, 47]. It satisfies the current conservation law and forms closed loops [45]. The indices i and μ indicate the color $i = 1, 2, \text{ and } 3$ and directions $\mu = 1, 2, 3, \text{ and } 4$, respectively.

First, we calculate the number density of the monopoles and anti-monopoles using the standard configurations. The numerical results of the standard configurations are in Table 27 in B.

To check the finite lattice volume effect on the numerical results, we set the values of the parameter β to $\beta =$

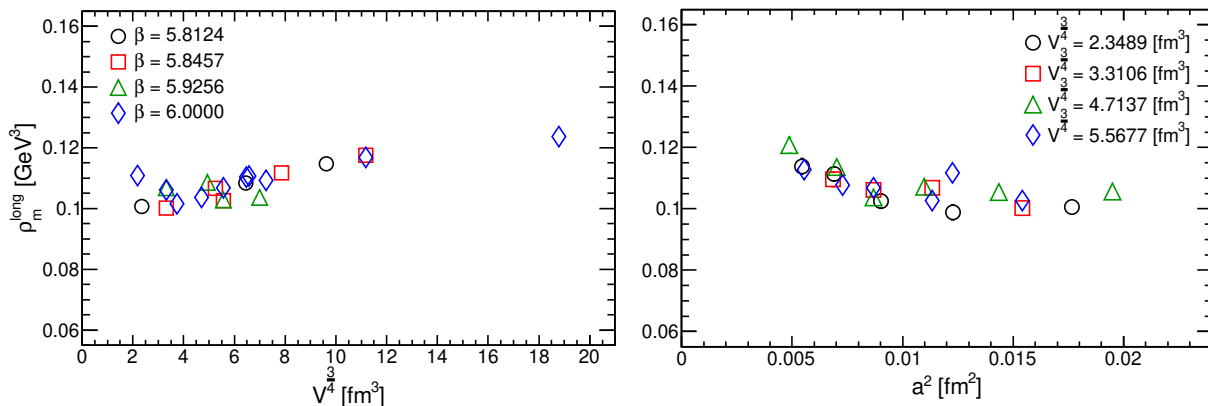


Fig. 1. The number density of the monopoles and anti-monopoles of the standard configurations. The left panel shows the effects of the finite lattice volume on the numerical results of the configurations of $\beta = 5.8124, 5.8457, 5.9256,$ and 6.0000 . The right panel shows the discretization effects on the numerical results of three-dimensional physical volumes $V_{\text{phys}}^{\frac{3}{4}} = 2.3489, 3.3106, 4.7137,$ and 5.5677 [fm^3].

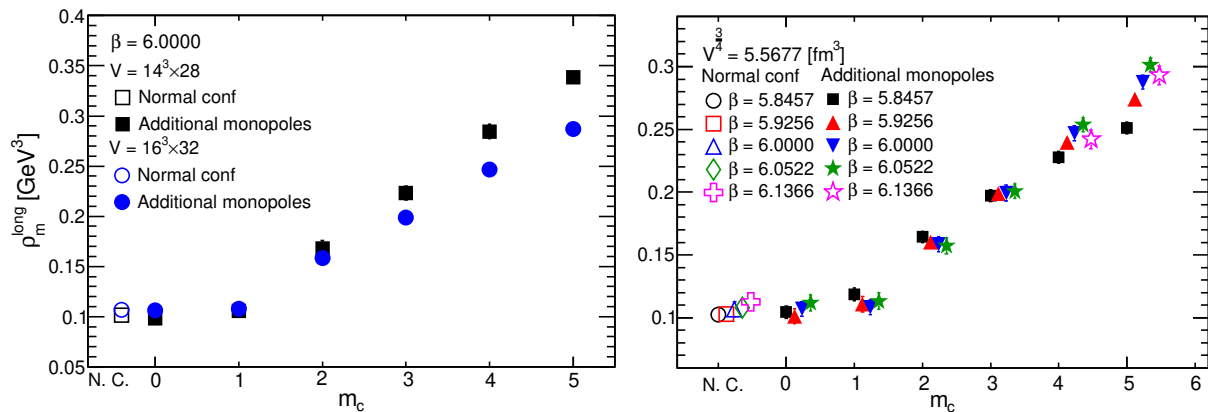


Fig. 2. The number density of the additional monopoles and anti-monopoles. The left panel shows the results of the configurations of $V = 14^3 \times 28$ and $V = 16^3 \times 32$, and the right panel compares the numerical results of the additional monopoles and anti-monopoles of three-dimensional physical volume $V_{\text{phys}}^{\frac{3}{4}} = 5.5677$ [fm^3] with the results of the standard configurations. The symbols in the right panel are slightly shifted along the horizontal axis to show the difference clearly.

5.8124, 5.8457, 5.9256, and 6.0000, and vary the lattice volumes. The left panel of Fig. 1 shows that the effects of the finite lattice volume appear when we use the fine lattice spacing ($\beta = 6.0000$) and three-dimensional physical volumes $V_{\text{phys}}^{\frac{3}{4}}$ from 2 to 4 [fm^3]; moreover, the calculated results slightly become larger as the physical volumes become larger.

Then, to inspect the discretization effects, we set the values of the parameter β and the lattice volumes V so that three-dimensional physical volumes are $V_{\text{phys}}^{\frac{3}{4}} = 2.3489, 3.3106, 4.7137,$ and 5.5677 and vary the values of the lattice spacing and the lattice volumes. The right panel of Fig. 1 shows that the numerical results of the different physical volumes are consistent; the results, however, slightly rise near the continuum limit. Therefore, in this study, we add the monopoles and anti-monopole to the vacua of the three-dimensional physical volume $V_{\text{phys}}^{\frac{3}{4}} =$

5.5677 [fm^3] ($V_{\text{phys}} = 9.8682$ [fm^4]) and vary the values of the parameter β to confirm the discretization effects and obtain the results at the continuum limit by interpolation.

The monopole creation operator, which has a certain number of magnetic charges, makes a certain number of monopoles and anti-monopoles in vacua; therefore, when the lattice volumes of $\beta = 6.0000$ increase from $V = 14^3 \times 28$ to $V = 16^3 \times 32$, the number densities of the monopoles and anti-monopoles of each magnetic charge reduce as shown in the left panel of Fig. 2.

The number densities of the monopoles and anti-monopoles computed from the configurations of the same three-dimensional physical volume $V_{\text{phys}}^{\frac{3}{4}} = 5.5677$ [fm^3] are shown in the right panel of Fig. 2. The figure shows that the finite lattice volume effects appear when we add the magnetic charges $m_c = 4$ and 5 to the lattice volume $V = 12^3 \times 24$. Therefore, we generate configurations of the larger lattice volume $V = 20^3 \times 40$ of the

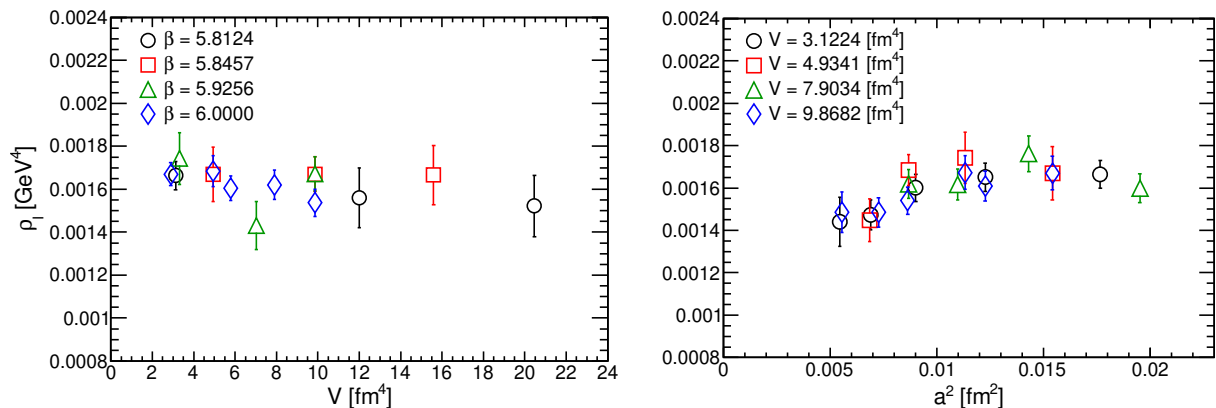


Fig. 3. The number density of the instanton and anti-instantons of the standard configurations. The left panel shows the numerical results of the parameter $\beta = 5.8124, 5.8457, 5.9256,$ and 6.0000 , and the right panel shows the numerical results of the physical volumes $V_{\text{phys}} = 3.1224, 4.9341, 7.9034,$ and 9.8682 [fm^4].

magnetic charges $m_c = 4$ and 5 and obtain the interpolated results at the continuum limit by fitting the curves.

The numerical results of the number density of the additional monopoles and anti-monopoles are shown in Table 29 in B.1.

Hereafter, we do not diagonalize the $SU(3)$ matrices under any conditions. We do not perform the Abelian projection or smearing to the $SU(3)$ gauge links. We directly calculate the overlap Dirac operator from the $SU(3)$ non-Abelian gauge links in the sections below.

2.2 The number density of the instantons and anti-instantons of standard configurations

The overlap Dirac operator preserves exact chiral symmetry at the continuum limit, and there are fermion zero modes in its spectrum [34, 35, 36, 37].

We calculate the low-lying eigenvalues λ_i and eigenvectors of the massless overlap Dirac operator to count the number of instantons and anti-instantons from the number of fermion zero modes in the vacua. We use the numerical technique [48] and calculate approximately 100 pairs of low-lying eigenvalues and eigenvectors for each configuration by using the subroutines (ARPACK). The numbers of configurations N_{conf} used for the calculations of the eigenvalues and eigenvectors are in Table 28 in B and Table 30 in C. The definition and parameters of the massless overlap Dirac operator are the same as those in our previous studies [39, 41].

To detect the zero modes in the spectrum, we first find eigenvalues with absolute values smaller than 1.0×10^{-7} , calculate their chiralities by multiplying γ_5 by their eigenvectors, and count the number of eigenvalues for each chirality. We define the number of zero modes as follows: when the chirality is a positive sign, the number of zero modes is n_+ . When the chirality is a negative sign, the number of zero modes is n_- . Let the number of instantons be n_+ and the number of anti-instantons be n_- .

In our studies, we, however, have never observed zero modes of positive chirality and negative chirality from the

same configuration. The observed zero modes are consistent with the topological charges Q , which are defined as follows:

$$Q = n_+ - n_- \quad (2)$$

Therefore, we estimate the number of instantons and anti-instantons in the vacua N_I from the topological charges Q as follows [39]:

$$N_I = \langle Q^2 \rangle \quad (3)$$

The value of the brackets $\langle \mathcal{O} \rangle$ indicates that the average value given by the sum of the numerical results is divided by the number of configurations. The number density of the instantons and anti-instantons ρ_I is calculated as follows:

$$\rho_I = \frac{N_I}{V_{\text{phys}}} [\text{GeV}^4] \quad (4)$$

This formula indicates that the number density of the instantons and anti-instantons equals the topological susceptibility.

The phenomenological model [29] predicts that the instanton (or anti-instanton) density is 8×10^{-4} [GeV^4]; accordingly, the number density of the instantons and anti-instantons of the standard configuration is

$$\rho_I^{\text{sta}} = 1.6 \times 10^{-3} [\text{GeV}^4], \quad (5)$$

and the number of instantons and anti-instantons of the standard configuration in the physical volume V_{phys} is

$$N_I^{\text{sta}} = \rho_I^{\text{sta}} V_{\text{phys}}. \quad (6)$$

Similar to the computations of the number density of the monopoles and anti-monopoles, we estimate the number density of the instantons and anti-instantons of the standard configurations. The calculated results are listed in Table 28 in B.

First, to confirm the effects of the finite lattice volume on the calculated results, we set the value of the parameter β to $5.8124, 5.8457, 5.9256,$ and 6.0000 and vary the lattice volumes as shown in the left panel of Fig. 3. This

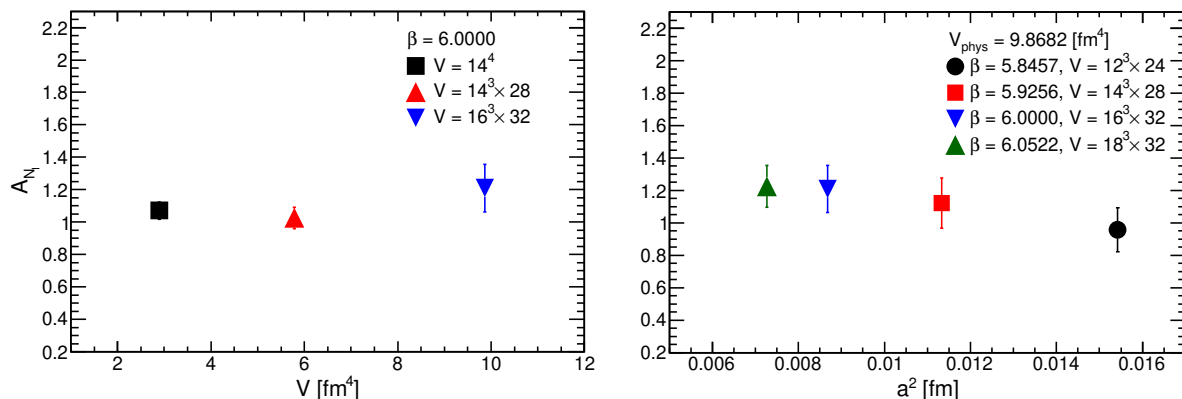


Fig. 4. Examining the effects of the finite lattice volume (left) and the discretization (right) on the fitting results of the slope A_{N_I} . The outcomes of $\beta = 6.0000$, $V = 14^4$ and $\beta = 6.0522$, $V = 18^3 \times 32$ are reported in our previous research [39,41]

shows that the numerical results are consistent with the prediction (5) and that the effects of the finite lattice volume are negligible.

Second, to confirm the discretization effects, we set the values of the parameter β and the lattice volumes V so that the physical volumes are $V_{\text{phys}} = 3.1224, 4.9341, 7.9034, \text{ and } 9.8682 \text{ [fm}^4\text{]}$ and vary the values of the lattice spacing a and the lattice volumes. The right panel of Fig. 3 shows that the discretization effects are small and that the calculated results are reasonably consistent with the prediction (5).

These results show that we can correctly estimate the number density of the instantons and anti-instantons, and the effects of the finite lattice volume and the discretization on the number density of the instantons and anti-instantons are small enough and negligible.

2.3 The creation of instantons and anti-instantons

Our previous studies quantitatively demonstrate that a pair of additional monopole and anti-monopole of the magnetic charges $m_c = 1$ makes one instanton or anti-instanton by fitting a linear curve. To confirm the influences of the finite lattice volume and discretization on this result, we quantitatively evaluate the increases in the number of instantons and anti-instantons N_I to the increases in the number of magnetic charges m_c from the results obtained by fitting the following linear curve:

$$N_I = A_{N_I} m_c + B_{N_I}. \quad (7)$$

The fitting results are listed in Table 2.

The prediction of the slope $A_{N_I}^{\text{Pre}}$ is one because a pair of additional monopole and anti-monopole of the magnetic charges $m_c = 1$ makes one instanton or anti-instanton. The predictions of the intercept $B_{N_I}^{\text{Pre}}$ are consistent with the numbers of instantons and anti-instantons of the normal configurations $N_I^{\text{sta}} = 6.1044$ for $V_{\text{phys}} = 5.7845 \text{ [fm}^4\text{]}$ ($V = 14^3 \times 28$, $\beta = 6.0000$) and $N_I^{\text{sta}} = 10.414$ for $V_{\text{phys}} = 9.8682 \text{ [fm}^4\text{]}$ (apart from $V = 14^3 \times 28$, $\beta = 6.0000$). These predictions are calculated from the function (6).

Table 2. The fitting results A_{N_I} , B_{N_I} , and χ^2/dof obtained by fitting the curve $N_I = A_{N_I} m_c + B_{N_I}$ to the results of N_I .

β	V	A_{N_I}	B_{N_I}	FR: m_c	$\frac{\chi^2}{\text{dof}}$
5.8457	$12^3 \times 24$	0.96(14)	10.7(4)	0-5	2.7/4.0
5.9256	$14^3 \times 28$	1.12(16)	11.2(4)	0-5	4.5/4.0
6.0000	$14^3 \times 28$	1.03(7)	6.09(16)	0-5	21.0/4.0
	$16^3 \times 32$	1.21(15)	10.1(4)	0-5	11.1/4.0

We compare the fitting results of the slope A_{N_I} together with our previous outcomes of lattices $\beta = 6.0000$, $V = 14^4$ and $\beta = 6.0522$, $V = 18^3 \times 32$, as shown in Fig. 4. Figure 4 and the fitting results in Table 2 indicate that the slope A_{N_I} and intercept B_{N_I} are consistent with our previous outcomes and predictions $A_{N_I}^{\text{Pre}}$ and $B_{N_I}^{\text{Pre}}$, respectively.

Furthermore, Fig. 4 shows that the influences of the finite lattice volume and discretization on the increases in the numbers of instantons and anti-instantons are negligible and one pair of additional monopole and anti-monopole of the magnetic charges $m_c = 1$ makes one instanton or anti-instanton.

Therefore, we give a prediction concerning the number of instantons and anti-instantons being in the configurations of the additional monopoles and anti-monopoles with the magnetic charges as follows:

$$N_I^{\text{Pre}}(m_c) = N_I^{\text{sta}} + m_c \quad (8)$$

Similarly, the prediction of the number density of the instantons and anti-instantons in the configurations of the additional monopoles and anti-monopoles with the magnetic charges is

$$\rho_I^{\text{Pre}}(m_c) = \left(\rho_I^{\text{sta}} + \frac{m_c}{V_{\text{phys}}} \right) [\text{GeV}^4]. \quad (9)$$

Next, we investigate the effects of the finite lattice volume and discretization on the calculated results of the number density of the instantons and anti-instantons of

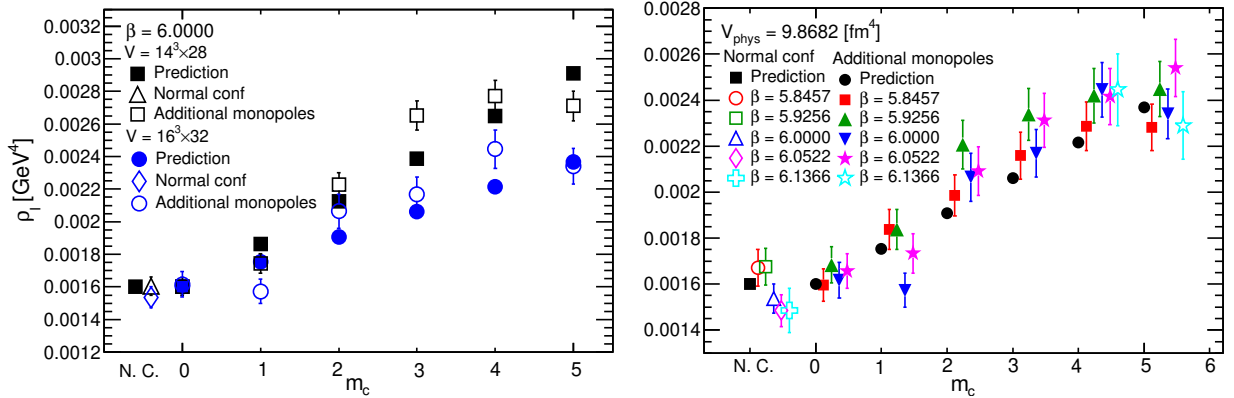


Fig. 5. Comparing the calculated results of the number density of the instantons and anti-instantons ρ_I using the configurations of the additional monopoles and anti-monopoles with the predictions. The left panel shows the results of the lattice volumes $V = 14^3 \times 28$ and $16^3 \times 32$, $\beta = 6.0000$. The right panel shows the results of $V_{\text{phys}} = 9.8682$ [fm⁴]. The symbols in the right panel are slightly shifted along the horizontal axis to show the difference clearly.

the additional monopoles and anti-monopoles and compare the numerical results with the predictions.

Figure 5 demonstrates that the number density of the instantons and anti-instantons increases with increasing the magnetic charges m_c , which shows that the numerical results are reasonably consistent with the predictions. Thus, the effects of the finite lattice volume and discretization on the calculated results are reasonably small.

The calculated results of the number of observed zero modes $N_Z = |Q|$, number of instantons and anti-instantons N_I , number density of instantons and anti-instantons ρ_I , and number of configurations N_{conf} together with the predictions are in Table 30 in C.

Table 3. The fitting results of the number density ρ_I of the instantons and anti-instantons by interpolation.

m_c	A_{ρ_I} [GeV ⁴ · fm ⁻²] $\times 10^{-2}$	B_{ρ_I} [GeV ⁴] $\times 10^{-3}$	FR: a^2 [fm ²] $\times 10^{-2}$	$\frac{\chi^2}{\text{dof}}$
N. C.	2.2(1.0)	1.35(11)	5.5-15.5	1.1/4.0
0	-0.5(1.2)	1.69(13)	7.2-15.5	0.6/2.0
1	2.5(1.4)	1.47(15)	7.2-15.5	4.2/2.0
2	-1.2(1.5)	2.21(18)	7.2-15.5	2.0/2.0
3	-1.1(1.7)	2.4(2)	7.2-15.5	1.8/2.0
4	-0.3(3.1)	2.5(3)	5.5-11.4	0.0/2.0
5	1.3(3.1)	2.3(3)	5.5-11.4	2.1/2.0

Last, we interpolate the number density of the instantons and anti-instantons ρ_I at the continuum limit for each magnetic charge m_c by fitting the following curve to the calculated results:

$$\rho_I = A_{\rho_I} x + B_{\rho_I}, \quad x = a^2 \text{ [fm}^2\text{]}. \quad (10)$$

We do not include the numerical results obtained using the lattice $V = 12^3 \times 24$ of $\beta = 5.8457$ of the magnetic

Table 4. The interpolated results of the number density of the instantons and anti-instantons ρ_I , square root of the number density $\rho_I^{\frac{1}{2}}$, and one-fourth root of the number density $\rho_I^{\frac{1}{4}}$. The fitting results of χ^2/dof are for ρ_I .

m_c	ρ_I^{int} [GeV ⁴] $\times 10^{-3}$	$\left(\rho_I^{\frac{1}{2}}\right)^{\text{int}}$ [GeV ²] $\times 10^{-2}$	$\left(\rho_I^{\frac{1}{4}}\right)^{\text{int}}$ [MeV] $\times 10^2$	FR: a^2 [fm ²] $\times 10^{-3}$	$\frac{\chi^2}{\text{dof}}$
N. C.	1.57(3)	3.97(4)	1.993(10)	5.5-15.5	6.1/5.0
0	1.64(4)	4.04(5)	2.011(12)	7.2-15.5	0.8/3.0
1	1.73(4)	4.17(5)	2.042(12)	7.2-15.5	7.5/3.0
2	2.08(5)	4.56(5)	2.136(13)	7.2-15.5	2.6/3.0
3	2.24(5)	4.73(6)	2.175(13)	7.2-15.5	2.2/3.0
4	2.43(6)	4.93(6)	2.220(14)	5.5-11.4	0.0/3.0
5	2.41(7)	4.91(6)	2.216(14)	5.5-11.4	2.3/3.0

charges 4 and 5 in the fitting ranges. The fitting results are in Table 3, which indicates that the errors of the slope A_{ρ_I} of the normal configuration and configuration of the magnetic charge $m_c = 1$ are larger than 45%. The fitting results of the slope apart from those results are zero because the errors are larger than the slope values. Moreover, we have shown that the influences of the finite lattice volume and discretization on the increases in the number of instantons and anti-instantons and their number density are small, as shown in Figs. 4 and 5. Therefore, we fit a constant function to the calculated results of the number density ρ_I , the square root of the number density $\rho_I^{\frac{1}{2}}$, and the one-fourth root of the number density $\rho_I^{\frac{1}{4}}$. The fitting results are given in Table 4.

The interpolated result of the number density of the normal configuration is $\rho_I^{\text{int}} = 1.57(3) \times 10^{-3}$ [GeV⁴], and the fitting result of χ^2/dof is 1.2. This interpolated result is consistent with the outcome of the phenomenological model (5). This indicates that we can adequately inter-

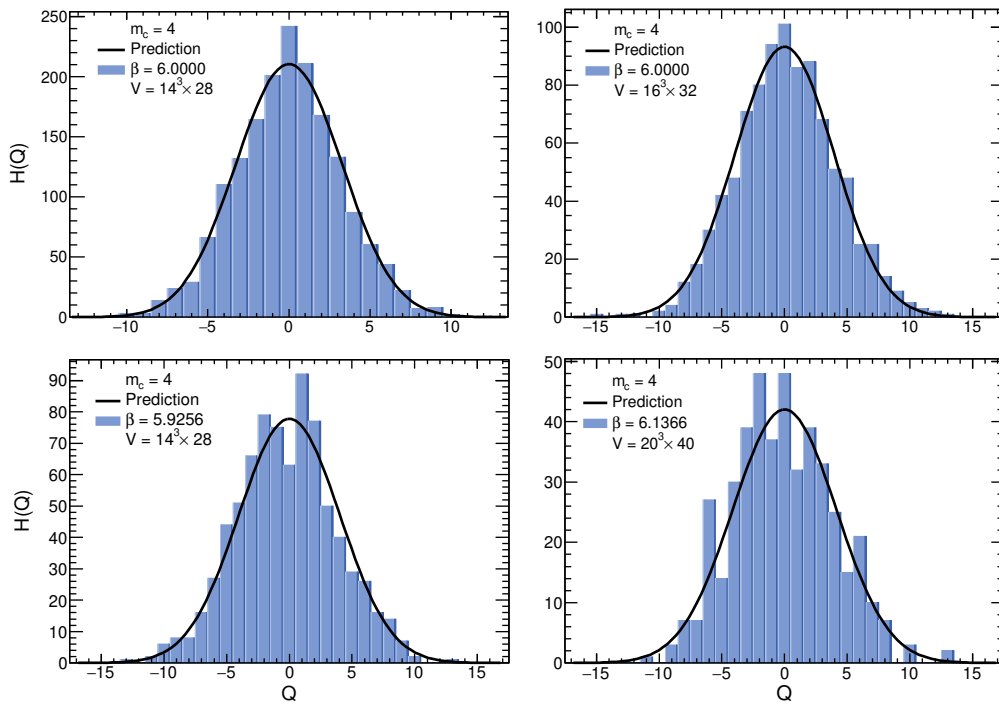


Fig. 6. The histograms $H(Q)$ of the topological charges Q . The magnetic charges are $m_c = 4$. The lattices are $\beta = 6.0000$, $V = 14^3 \times 28$ (upper left), $\beta = 5.9256$, $V = 14^3 \times 28$ (lower left), $\beta = 6.0000$, $V = 16^3 \times 32$ (upper right), and $\beta = 6.1366$, $V = 20^3 \times 40$ (lower right). The black lines indicate the fitting results by the prediction function of the topological charges.

Table 5. The fitting results of the distributions of the topological charges by the prediction functions. The fitting range FR is $-17 \leq Q \leq 17$. N. C. stands for the normal configuration.

β	V	m_c	$\langle \delta^2 \rangle$	$\mathcal{O}(V^{-1}) \times 10^{-2}$	$\frac{\chi^2}{\text{dof}}$
5.8457	$12^3 \times 24$	N. C.	10.3(5)	-2(3)	24.4/20.0
		0	10.0(5)	-2(3)	21.8/20.0
		1	10.8(6)	-0.9(3)	12.7/21.0
		2	10.3(6)	-2(3)	19.0/23.0
		3	10.2(7)	-3(3)	31.9/23.0
		4	10.3(8)	-2(3)	21.7/22.0
5.9256	$14^3 \times 28$	N. C.	10.9(6)	-1(3)	10.9/19.0
		0	10.8(6)	-2(3)	15.1/19.0
		1	10.1(5)	-2(3)	21.0/20.0
		2	11.9(8)	-3(3)	25.3/21.0
		3	11.8(8)	-2(3)	16.5/22.0
		4	12.0(9)	-2(4)	21.1/22.0
6.0000	$14^3 \times 28$	N. C.	5.9(2)	-1(2)	18.9/16.0
		0	6.1(2)	-0.6(2.4)	12.4/16.0
		1	5.5(2)	-0.8(2.4)	14.1/16.0
		2	6.2(3)	-0.9(2.4)	16.6/19.0
		3	7.1(4)	-0.5(2.4)	8.7/20.0
		4	6.3(4)	-1(2)	20.3/21.0
	$16^3 \times 32$	N. C.	10.1(5)	-0.6(3.1)	8.1/18.0
		0	10.2(5)	-2(3)	17.0/21.0
		1	8.9(5)	-2(3)	18.6/18.0
		2	10.6(7)	-2(3)	20.1/22.0
		3	11.2(8)	-2(3)	21.8/21.0
		4	11.3(8)	-1(3)	13.6/25.0
6.1366	$20^3 \times 40$	N. C.	8.4(6)	-6(5)	26.4/17.0
		4	12.8(1.5)	-3(5)	23.2/19.0
		5	9.0(1.1)	-4(5)	18.3/20.0
		5	9.0(1.1)	-4(5)	18.3/20.0

polate the numerical results of the number density of the instantons and anti-instantons to the continuum limit by fitting the constant function. Therefore, we use the interpolated results in Table 4 in the sections below. Hereafter, we do not include the numerical results obtained using the lattice $V = 12^3 \times 24$ of $\beta = 5.8457$ of the additional monopoles and anti-monopoles with the magnetic charges 4 and 5 in the fitting ranges for the interpolations to the continuum limit because of the reason we mentioned in subsection 2.1.

2.4 Distributions of the topological charge Q of additional monopoles and anti-monopoles

We add monopoles and anti-monopoles to the vacua by the monopole creation operator, and then the added monopoles and anti-monopoles create the zero modes of the positive chirality and negative chirality with the same probability because we assume the CP invariance. We cannot directly count the number of zero modes; therefore, when we add the monopoles and anti-monopoles to the vacuum, the difference in the topological charges between the standard configurations and the configurations with the added monopoles and anti-monopoles arises.

To confirm whether the added monopoles and anti-monopoles affect the vacuum structure, we predict the distribution functions of the topological charges for each magnetic charge and compare them with the histograms of the topological charges $H(Q)$, as shown in Fig. 6. The dis-

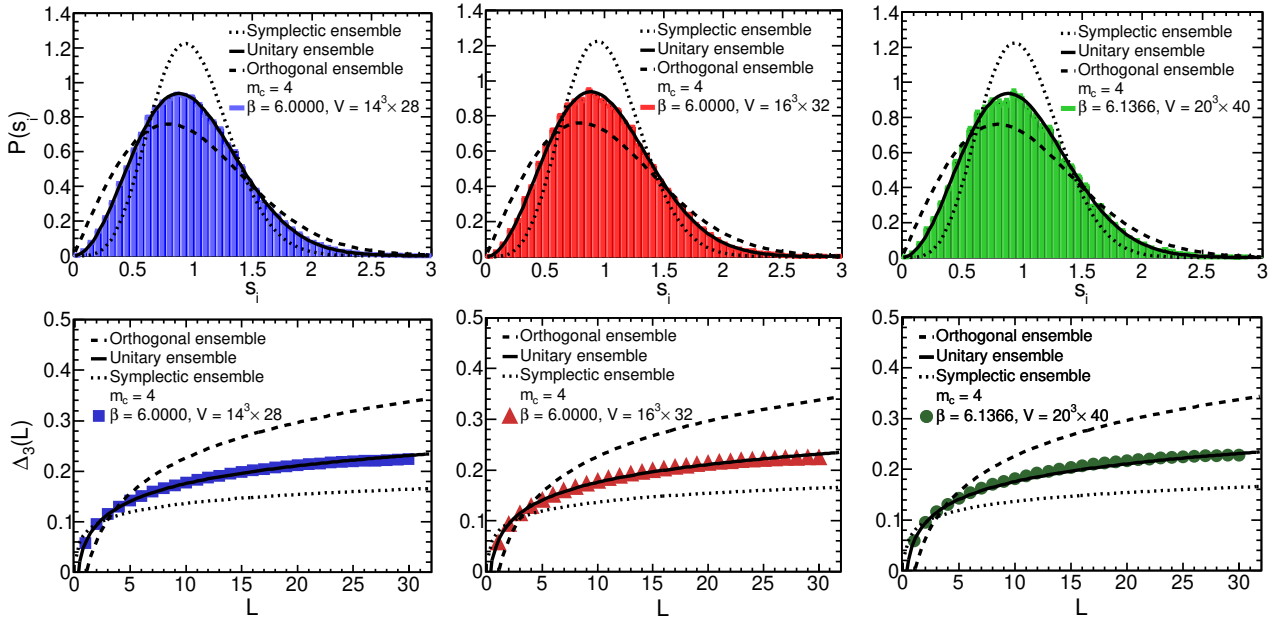


Fig. 7. The distributions of the nearest neighbor spacing $P(s_i)$ (upper figures) and the spectral rigidity $\Delta_3(L)$ (lower figures) compared with the GRMT. The magnetic charges are $m_c = 4$. The lattices are $\beta = 5.8457$, $V = 12^3 \times 24$ (upper and lower left), $\beta = 6.0000$, $V = 14^3 \times 28$ (upper and lower middle), and $\beta = 6.0000$, $V = 16^3 \times 32$ (upper and lower right). The black dotted, full, and dashed lines represent the prediction functions of the GSE, GUE, and GOE of the GRMT, respectively. The colored lines and symbols indicate the numerical results.

tribution functions for each magnetic charge which comprise the Gaussian distributions and probabilities of the zero-mode creations are given in reference [39,41]. The fitting results of the normal configurations and the configurations with the added monopoles and anti-monopoles are listed in Table 5.

If the prediction functions are consistent with the distributions of the topological charges that are numerically calculated, the fitting results $\langle \delta^2 \rangle$ are consistent with the analytical results $N_I^{\text{sta}} = 6.1044$ for $V_{\text{phys}} = 5.7845$ [fm^4] and $N_I^{\text{sta}} = 10.414$ for $V_{\text{phys}} = 9.8682$ [fm^4], as presented in Table 30 in C. Moreover, the fitting results of $\mathcal{O}(V^{-1})$ that are the correction terms of the distribution functions are zero.

The fitting results $\langle \delta^2 \rangle$ in Table 5 are consistent with the predictions N_I^{sta} and outcomes N_I of the standard configurations in Table 30 in C. The fitting results of the correction terms $\mathcal{O}(V^{-1})$ are zero, and χ^2/dof are small enough. Therefore, these results indicate that the effects of the finite lattice volume and discretization on detecting topological charges are negligible, and the added monopoles and anti-monopoles create instantons and anti-instantons without affecting the vacuum structure.

3 Comparisons of the Dirac spectrum with the random matrix theory

We add the monopoles and anti-monopoles by applying the monopole creation operator to the vacuum. Therefore, to inspect whether the added monopoles and anti-

monopoles affect the low-lying eigenvalues of the overlap Dirac operator, we compare the low-lying eigenvalues with the predictions of the RMT.

The Gaussian random matrix theory (GRMT) universally predicts the distributions of the short-range fluctuations and the mean-square deviations of the staircase function from the linear function. The predictions of the GRMT are classified into the following three Gaussian ensemble classes obeying the symmetries [50,51]: (i) Gaussian symplectic ensemble. (ii) Gaussian unitary ensemble. (iii) Gaussian orthogonal ensemble.

We first improve the eigenvalues λ_k of the massless overlap Dirac operator to be near the continuum limit [52]. The improved eigenvalues are the pure imaginary numbers and come in positive and negative pairs. The subscript k indicates the k th eigenvalue. We put the improved nonzero and positive eigenvalues in ascending order as follows: $a\bar{\lambda}_1 < \dots < a\bar{\lambda}_k < \dots < a\bar{\lambda}_n$.

We use the unfolding procedure techniques as follows [53]: First, we plot the improved eigenvalues $a\bar{\lambda}_k$ on the horizontal axis against their numbers k on the vertical axis for each configuration. We then fit the polynomial function of order $d = 3$ to the plot and obtain the smooth curve N_{poly} using the fitting results of the coefficients for each configuration. Next, we obtain the following unfolded eigenvalues E_k by substituting the improved eigenvalues $a\bar{\lambda}_k$ into the smooth curve N_{poly} for each configuration:

$$E_k = N_{\text{poly}}(a\bar{\lambda}_k). \quad (11)$$

First, we calculate the nearest-neighbor spacing s_i using the unfolded eigenvalues E_k to inspect the influence of

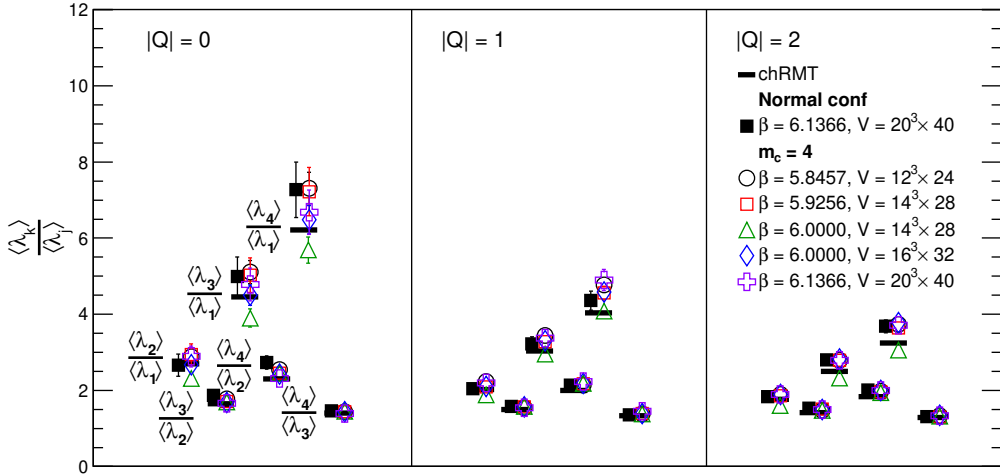


Fig. 8. Comparing the ratios of the low-lying eigenvalues $\frac{\langle \lambda_k^{|Q|} \rangle}{\langle \lambda_j^{|Q|} \rangle}$ in each topological charge sector $|Q| = 0, 1,$ and 2 with the prediction of chRMT and examining the effects of the finite lattice volume and the discretization. The black and colored symbols indicate the numerical results of the normal configuration and magnetic charge $m_c = 4$. The black horizontal lines indicate the predictions of chRMT.

Table 6. Comparing the numerical results of $\frac{\langle \lambda_k^{|Q|} \rangle}{\langle \lambda_j^{|Q|} \rangle}$ with the prediction of chRMT. The normal configurations and configurations of the magnetic charges $m_c = 4$ are used. The prediction of chRMT is given in Table 3 [49].

$ Q $	k/j	$\beta = 5.8457$ $V = 12^3 \times 24$		$\beta = 5.9256$ $V = 14^3 \times 28$		$\beta = 6.0000$ $V = 14^3 \times 28$		$\beta = 6.0000$ $V = 16^3 \times 32$		$\beta = 6.1366$ $V = 20^3 \times 40$		RMT
		N. C.	$m_c = 4$	N. C.	$m_c = 4$	N. C.	$m_c = 4$	N. C.	$m_c = 4$	N. C.	$m_c = 4$	
0	2/1	2.90(18)	2.88(19)	2.8(2)	2.9(3)	2.32(14)	2.31(15)	3.1(2)	2.67(17)	2.7(3)	2.9(3)	2.70
	3/1	5.0(3)	5.1(3)	5.0(4)	5.0(4)	4.1(2)	3.9(2)	5.3(3)	4.5(3)	5.0(5)	4.8(4)	4.46
	4/1	7.3(4)	7.3(4)	7.1(5)	7.2(6)	6.0(3)	5.7(3)	7.9(5)	6.5(4)	7.3(7)	6.7(6)	6.22
	3/2	1.74(6)	1.77(8)	1.78(9)	1.71(9)	1.79(12)	1.70(10)	1.70(7)	1.68(7)	1.87(13)	1.66(10)	1.65
	4/2	2.53(8)	2.54(11)	2.56(12)	2.45(12)	2.57(16)	2.46(17)	2.53(9)	2.43(9)	2.73(17)	2.31(13)	2.30
	4/3	1.46(4)	1.43(5)	1.44(6)	1.44(5)	1.44(9)	1.45(10)	1.49(5)	1.44(4)	1.46(8)	1.40(7)	1.40
1	2/1	2.20(7)	2.23(8)	2.16(8)	2.09(9)	1.95(7)	1.88(8)	2.18(8)	2.10(8)	2.04(12)	2.19(14)	2.02
	3/1	3.44(11)	3.44(11)	3.46(13)	3.28(13)	2.99(11)	2.95(12)	3.35(12)	3.30(12)	3.22(19)	3.4(2)	3.03
	4/1	4.74(14)	4.76(15)	4.81(17)	4.56(18)	4.00(14)	4.09(16)	4.72(16)	4.59(16)	4.4(2)	4.9(3)	4.04
	3/2	1.56(4)	1.55(4)	1.60(5)	1.56(5)	1.53(6)	1.57(7)	1.54(4)	1.57(4)	1.58(6)	1.54(7)	1.50
	4/2	2.16(5)	2.14(5)	2.23(6)	2.18(6)	2.05(8)	2.18(10)	2.17(5)	2.18(6)	2.13(8)	2.24(9)	2.00
	4/3	1.38(2)	1.38(3)	1.39(3)	1.39(3)	1.34(5)	1.39(6)	1.41(3)	1.39(3)	1.36(4)	1.50(5)	1.33
2	2/1	1.90(6)	1.89(6)	1.88(7)	1.86(7)	1.75(6)	1.58(7)	1.90(7)	1.89(7)	1.84(9)	1.87(10)	1.76
	3/1	2.81(8)	2.79(8)	2.85(10)	2.79(10)	2.59(8)	2.32(11)	2.83(10)	2.82(10)	2.80(13)	2.79(13)	2.50
	4/1	3.76(11)	3.74(11)	3.80(13)	3.64(12)	3.39(11)	3.06(14)	3.77(12)	3.78(13)	3.68(17)	3.72(17)	3.24
	3/2	1.48(4)	1.48(4)	1.52(4)	1.51(4)	1.48(5)	1.47(8)	1.49(4)	1.49(4)	1.53(6)	1.49(6)	1.42
	4/2	1.98(5)	1.98(5)	2.03(5)	1.96(5)	1.93(6)	1.94(11)	1.99(5)	2.00(5)	2.01(7)	1.99(8)	1.83
	4/3	1.34(3)	1.34(3)	1.33(3)	1.30(3)	1.31(4)	1.32(7)	1.33(3)	1.34(3)	1.31(4)	1.33(5)	1.29

additional monopoles and anti-monopoles on short-range fluctuations as follows:

$$s_i = E_{i+1} - E_i. \tag{12}$$

We make distributions of the nearest-neighbor spacing $P(s_i)$, which are normalized to unity, and show the comparisons with the predictions of the GRMT in the upper panels in Fig. 7. The distribution of the nearest-neighbor spacing for each Gaussian ensemble class is given in reference [54].

Next, we inspect the influence of additional monopoles and anti-monopoles on the fluctuations of the eigenvalues of the interval L on the unfolded scale by calculating the spectral rigidity $\Delta_3(L)$. The spectral rigidity $\Delta_3(L)$ is defined as the mean-square deviation of the staircase function from the linear function [51]. We use formula (I-39)

of reference [55] and almost all unfolded eigenvalues E_k and evaluate the spectral rigidity by calculating the spectral and ensemble averages. The calculated results of the spectral rigidity compared with the predictions of three Gaussian ensemble classes are shown in the lower panels in Fig. 7. The predictions of the spectral rigidity are given in reference [54].

Figure 7 shows that the numerical results of the configurations of $m_c = 4$ of the different lattice volumes and values of the lattice spacing are consistent with the predictions of the Gaussian unitary ensemble. We have already shown that the outcomes of the different magnetic charges are compatible with the Gaussian unitary ensemble in our previous studies.

Therefore, additional monopoles and anti-monopoles, finite lattice volume, and discretization do not affect the

fluctuations of the nearest-neighbor spacing and eigenvalues of the interval L on the unfolded scale.

Next, chiral random matrix theory (chRMT) universally predicts the distribution of low-lying eigenvalues of the Dirac operator for each eigenvalue number k [56, 57] of each topological charge sector $|Q|$. The following relation exists between the k th scaled eigenvalue of chRMT $z_k^{|Q|}$ and the k th eigenvalue of the Dirac operator $a\lambda_k^{|Q|}$ of the topological charge sector $|Q|$:

$$z_k^{|Q|} = \Sigma V \lambda_k^{|Q|}. \quad (13)$$

The parameter Σ is the scale parameter of eigenvalue distributions.

We compute the ratios of the eigenvalues $\frac{\langle z_k^{|Q|} \rangle}{\langle z_j^{|Q|} \rangle}$ [49] using the improved eigenvalues $a\bar{\lambda}_k$ to remove the uncertainty coming from the scale parameter Σ and compare the numerical results with the predictions of chRMT for each topological charge sector as shown in Fig. 8. The numerical results and the predictions of chRMT are listed in Table 6. We have already shown that the ratios of the numerical results of the different magnetic charges using the lattice $V = 18^3 \times 32$, $\beta = 6.0522$ are consistent with the predictions of chRMT in our previous study.

These results indicate that the numerical results are reasonably consistent with the predictions of chRMT and that the finite lattice volume and discretization do not affect the ratios of the low-lying eigenvalues of the overlap Dirac operator.

4 PCAC relation, renormalization constant \hat{Z}_S , and renormalized chiral condensate

We calculate the correlations of the pseudoscalar and scalar densities using the eigenvalues and eigenvectors of the overlap Dirac operator and the renormalization constant for the scalar density. We then evaluate the renormalized chiral condensate in chRMT using the analytic results of the scale parameter Σ of eigenvalue distributions of the overlap Dirac operator.

4.1 PCAC relation

This subsection briefly explains the calculations of the correlation functions. The computations of the correlation functions and the notation are the same, as those in our previous study [41].

We calculate the massive eigenvalues λ_k^{mass} of the massive overlap Dirac operator using the eigenvalues λ_k of the massless overlap Dirac operator D as follows:

$$a\lambda_k^{\text{mass}} = a \left(1 - \frac{\bar{m}_{ud}}{2\rho} \right) \lambda_k + a\bar{m}_{ud} \quad (14)$$

In this study, we set the mass parameter ρ for the massless overlap Dirac operator to $a\rho = 1.4$. We define the input

quark mass \bar{m}_{ud} for the pion as follows:

$$a\bar{m}_{ud} \equiv \frac{a(m_u + m_d)}{2} \quad (15)$$

The operators of the scalar density \mathcal{O}_S and pseudoscalar density \mathcal{O}_P are defined as follows:

$$\mathcal{O}_S = a^3 \bar{\psi}_1 \left(1 - \frac{D}{2\rho} \right) \psi_2 \quad (16)$$

$$\mathcal{O}_P = a^3 \bar{\psi}_1 \gamma_5 \left(1 - \frac{D}{2\rho} \right) \psi_2 \quad (17)$$

The quark propagator is defined as

$$\mathcal{G}(\vec{y}, y^0; \vec{x}, x^0) \equiv a^3 \sum_k \frac{\psi_k(\vec{x}, x^0) \psi_k^\dagger(\vec{y}, y^0)}{\lambda_k^{\text{mass}}}. \quad (18)$$

The correlation function of the scalar density is

$$\mathcal{C}_S(\Delta t) = \frac{a^3}{V} \sum_{\vec{x}_1} \sum_{\vec{x}_2, t} \langle \mathcal{O}_S^C(\vec{x}_2, t) \mathcal{O}_S(\vec{x}_1, t + \Delta t) \rangle. \quad (19)$$

The correlation function of the pseudoscalar density is

$$\mathcal{C}_P(\Delta t) = \frac{a^3}{V} \sum_{\vec{x}_1} \sum_{\vec{x}_2, t} \langle \mathcal{O}_{PS}^C(\vec{x}_2, t) \mathcal{O}_{PS}(\vec{x}_1, t + \Delta t) \rangle. \quad (20)$$

The superscript C stands for the Hermitian conjugate. We write the functions (18), (19), and (20) omitting the dimension a of the lattice sites for convenience.

We want to precisely evaluate the effects of the monopoles and instantons on observables near the chiral limit; however, unphysical zero modes near the chiral limit affect the observables. Therefore, to remove undesirable influences caused by unphysical zero modes, we calculate the following subtracted correlation function [58, 59]:

$$\mathcal{C}_{P-S} \equiv \mathcal{C}_P - \mathcal{C}_S. \quad (21)$$

Suppose that the following formula can approximate the subtracted correlation function (21):

$$\mathcal{C}_{P-S}(t) = \frac{a^4 G_{P-S}}{am_{PS}} \exp\left(-\frac{m_{PS}}{2} T\right) \cosh\left[m_{PS} \left(\frac{T}{2} - t\right)\right]. \quad (22)$$

We vary the input quark mass (15) of the massive eigenvalues from 30 to 150 [MeV] and calculate the subtracted correlation function (21). We fit formula (22) to the numerical results of the correlations, obtain the fitting results of the pseudoscalar mass am_{PS} and coefficient $a^4 G_{P-S}$, and calculate the observables using them in the later sections. The fitting ranges are determined so that the fitting results of χ^2/dof are approximately 1.

We list the fitting results of am_{PS} , $a^4 G_{P-S}$, and χ^2/dof and the numerical results of $(am_{PS})^2$ and the decay constant of the pseudoscalar meson aF_{PS} in the tables in E as follows: (i) The results of $V = 12^3 \times 24$ of $\beta = 5.8457$ are

in Tables 32, 33, and 34. (ii) The results of $V = 14^3 \times 28$ of $\beta = 5.9256$ are in Tables 35, 36, 37, and 38. (iii) The results of $V = 14^3 \times 28$ of $\beta = 6.0000$ are in Tables 39, 40, 41, and 42. (iv) The results of $V = 16^3 \times 32$ of $\beta = 6.0000$ are in Tables 43, 44, 45, and 46. (v) The results of $V = 20^3 \times 40$ of $\beta = 6.1366$ are in Tables 47 and 48. The fitting results and the numerical results of $V = 18^3 \times 32$ of $\beta = 6.0522$ are given in reference [41].

First, we confirm the effects of the additional monopoles and anti-monopoles on the partially conserved axial current (PCAC) relation between the numerical results of the square mass of the pseudoscalar meson $(am_{PS})^2$ and the input quark mass (15). The PCAC relation is defined as follows:

$$m_{PS}^2 \equiv A\bar{m}_{ud} \tag{23}$$

We fit the following linear function to the numerical results:

$$(am_{PS})^2 = a^2 A_{PCAC}^{(1)} \bar{m}_{ud} + a^2 B_{PCAC}. \tag{24}$$

The fitting ranges are determined so that the fitting results of χ^2/dof are approximately 1. The fitting results of $a^2 B_{PCAC}$ are non-zero; however, the values are small enough, as indicated in Table 49 in F.

The fitting results of the slope $aA_{PCAC}^{(1)}$ of each magnetic charge calculated using the same lattice are reasonably consistent, except that the fitting results of the lattice $V = 12^3 \times 24$ gradually decrease when the number of magnetic charges m_c is larger than 3, as shown in the same table. The decrease comes by adding the monopoles and anti-monopoles with high magnetic charges to the small lattice volume, which we have already mentioned in subsection 2.1. Moreover, we detect the influence of the finite lattice volume on the slope $aA_{PCAC}^{(1)}$ by comparing the fitting results of $V = 14^3 \times 28$ of $\beta = 6.0000$ with $V = 16^3 \times 32$.

To reduce the errors of the renormalization constant \hat{Z}_S for the scalar density, we remove the intercept from the fitting curve (24) and fit the following curve to the numerical results:

$$(am_{PS})^2 = a^2 A_{PCAC}^{(2)} \bar{m}_{ud}. \tag{25}$$

The fitting results of the slopes $aA_{PCAC}^{(2)}$ and parameter χ^2/dof are shown in Table 49 in F. The fitting ranges are the same as fitting by the curve (24). In the sections below, we use the fitting results of the slope $A_{PCAC}^{(2)}$ for computing the renormalization constant Z_S for the scalar density and the average mass of the up and down quarks.

4.2 Renormalization constant \hat{Z}_S for the scalar density

We obtain the renormalization constant \hat{Z}_S for the scalar density by the nonperturbative calculations [60,61] using the fitting results of the slope $aA_{PCAC}^{(2)}$. We list the calculated results of \hat{Z}_S in Table 49 in F. Comparing the renormalization constant \hat{Z}_S computed using the lattice

volume $V = 14^3 \times 28$ of $\beta = 6.0000$ with the result of the lattice volume $V = 16^3 \times 32$ of $\beta = 6.0000$ indicates that there is an influence of the finite lattice volume.

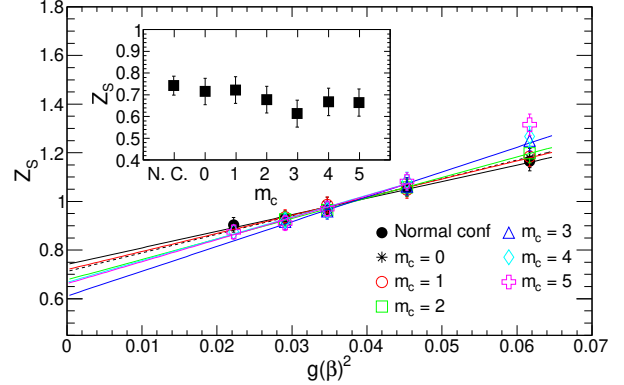


Fig. 9. The interpolations at the continuum limit of the numerical results of the renormalization constant \hat{Z}_S for the scalar density. The colored symbols and the colored lines indicate the numerical results and the fitting results, respectively. The small window in the figure shows the interpolated results of \hat{Z}_S .

The renormalization constant \hat{Z}_S depends on the bare coupling $g(\beta)$ [61]; therefore, we interpolate the calculated results of the renormalization constant \hat{Z}_S to the continuum limit by fitting the following linear function as shown in Fig. 9:

$$Z_S = A_{\hat{Z}_S} x + \hat{Z}_S^{\text{int}}, \quad x = g(\beta)^2. \tag{26}$$

The fitting results are in Table 7. The small window in Fig. 9 demonstrates that the interpolated results \hat{Z}_S^{int} are consistent except that the result of the magnetic charge $m_c = 3$ shows a minor effect caused by the finite lattice volume. This indicates that the additional monopoles and anti-monopoles do not affect the renormalization constant for the scalar density at the continuum limit.

Table 7. The fitting results of the slope $A_{\hat{Z}_S}$ and the interpolated results \hat{Z}_S^{int} of the renormalization constant.

m_c	$A_{\hat{Z}_S}$	\hat{Z}_S^{int}	FR: $g(\beta)^2 \times 10^{-2}$	$\frac{\chi^2}{\text{dof}}$
N. C.	6.8(1.1)	0.74(4)	2.2-6.2	0.4/3.0
0	7.6(1.4)	0.71(6)	2.8-6.2	0.2/2.0
1	7.4(1.4)	0.72(6)	2.8-6.2	0.1/2.0
2	8.4(1.5)	0.68(6)	2.8-6.2	0.0/2.0
3	10.2(1.5)	0.61(6)	2.8-6.2	0.3/2.0
4	8.9(1.9)	0.67(6)	2.2-4.6	0.4/2.0
5	9.0(1.9)	0.66(6)	2.2-4.6	0.5/2.0

4.3 The renormalized chiral condensate in chRMT

Suppose that the following relationship in $N_f = 3$ between the chiral condensate and the scale parameter of the eigenvalue distribution in chRMT holds [61]:

$$\langle \bar{\psi}\psi \rangle_{\text{RMT}} = -\Sigma. \quad (27)$$

We evaluate the renormalized chiral condensate $\langle \bar{\psi}\psi \rangle_{\text{RMT}}^{\overline{\text{MS}}}$ in the $\overline{\text{MS}}$ -scheme at 2 [GeV] using the outcomes of the scale parameter Σ and renormalization constant \hat{Z}_S for the scalar density.

First, we derive the scale parameter by substituting the scaled eigenvalues $z_k^{|Q|}$ that are analytically calculated and the numerical results of the improved eigenvalues $\lambda_k^{|Q|}$ into formula (13) [49]. We presume that the scale parameter computed for each eigenvalue number k of each topological charge sector $|Q|$ is independent, and then calculate the average of the scale parameter using the results of the eigenvalue numbers k from 1 to 4 of each topological charge sector $|Q|$ from 0 to 2.

Finally, the renormalized chiral condensate in the $\overline{\text{MS}}$ -scheme at 2 [GeV] is evaluated as follows:

$$\langle \bar{\psi}\psi \rangle_{\text{RMT}}^{\overline{\text{MS}}} (2 \text{ [GeV]}) = \frac{\hat{Z}_S}{0.72076} \langle \bar{\psi}\psi \rangle_{\text{RMT}} \quad (28)$$

We use each numerical result of the renormalization constant calculated for each lattice and configuration type (for each magnetic charge or standard configuration). The numerical results of the scale parameter and renormalized chiral condensate in the $\overline{\text{MS}}$ -scheme at 2 [GeV] are given in Table 31 in D.

Table 8. Comparing the prediction $\langle \bar{\psi}\psi \rangle^{\text{Pre}}$ with the interpolated results $\langle \bar{\psi}\psi \rangle_{\text{RMT}}^{\overline{\text{MS}},\text{int}}$ at the continuum limit, and their fitting results.

m_c	$\langle \bar{\psi}\psi \rangle^{\text{Pre}}$ [GeV ³] $\times 10^{-2}$	$\langle \bar{\psi}\psi \rangle_{\text{RMT}}^{\overline{\text{MS}},\text{int}}$ [GeV ³] $\times 10^{-2}$	FR: a^2 [fm ²] $\times 10^{-2}$	$\frac{\chi^2}{\text{dof}}$
N. C.	-2.0280	-2.52(4)	5.5-15.5	2.1/4.0
0	-2.0280	-2.52(4)	7.2-15.5	1.6/3.0
1	-2.1231	-2.66(5)	7.2-15.5	1.0/3.0
2	-2.2142	-2.89(5)	7.2-15.5	0.6/3.0
3	-2.3016	-3.01(5)	7.2-15.5	1.1/3.0
4	-2.3859	-3.11(5)	5.5-11.4	0.9/3.0
5	-2.4672	-3.16(6)	5.5-11.4	4.8/3.0

We first interpolate the calculated results of the renormalized chiral condensate in the $\overline{\text{MS}}$ -scheme at 2 [GeV] to the continuum limit by fitting a linear function. The fitting results of the slope are zero considering their errors, except that the error of the slope value of the magnetic charge $m_c = 5$ is 52%. Therefore, we fit a constant function and list the interpolated results of $\langle \bar{\psi}\psi \rangle_{\text{RMT}}^{\overline{\text{MS}}}$ in Table 8. The fitting results of χ^2/dof are less than 1.6. This shows

that the discretization influence on the numerical results is insignificant.

We have already reported that the renormalized chiral condensate in the $\overline{\text{MS}}$ -scheme at 2 [GeV] decreases in direct proportion to the square root of the number density of the instantons and anti-instantons by comparing with the following prediction concerning the chiral condensate [41]:

$$\langle \bar{\psi}\psi \rangle^{\text{Pre}}(m_c) = -\frac{1}{\bar{\rho}} \left(\frac{\pi N_c}{13.2} \right)^{\frac{1}{2}} \left(\rho_I^{\text{sta}} + \frac{m_c}{V_{\text{phys}}} \right)^{\frac{1}{2}}. \quad (29)$$

Here the predictions of the number density of the instantons and anti-instantons $\rho_I^{\text{Pre}}(m_c)^{\frac{1}{2}}$ are given in Table 30 in C. The number of colors is $N_c = 3$. The inverse of the average size of the instanton is

$$\frac{1}{\bar{\rho}} = 6 \times 10^2 \text{ [MeV]}. \quad (30)$$

The predictions of the chiral condensate $\langle \bar{\psi}\psi \rangle^{\text{Pre}}$ are given in Table 8 and Table 51 in H.

We then fit the following linear function to the numerical results to quantitatively evaluate the decreases in the chiral condensate by comparing the fitting results with the prediction shown in Fig. 10:

$$\langle \bar{\psi}\psi \rangle = -A_{\langle \bar{\psi}\psi \rangle}^{\text{RMT}} x, \quad x = \rho_I^{\frac{1}{2}} \text{ [GeV}^2\text{]}. \quad (31)$$

The slope of the prediction is $A_{\langle \bar{\psi}\psi \rangle}^{\text{Pre}} = 0.5070 \text{ [GeV]}$. The fitting results are listed in Table 9.

Table 9. The fitting results obtained by the linear curves $\langle \bar{\psi}\psi \rangle = -A_{\langle \bar{\psi}\psi \rangle}^{\text{RMT}} x$, ($x = \rho_I^{\frac{1}{2}}$, [GeV²]). The configurations of the lattice volumes $V = 14^3 \times 28$ and $V = 16^3 \times 32$ of $\beta = 6.0000$ and the interpolated results are used.

Conf	$A_{\langle \bar{\psi}\psi \rangle}^{\text{RMT}}$ [GeV]	FR: $\rho_I^{\frac{1}{2}}$ [GeV ²] $\times 10^{-2}$	$\frac{\chi^2}{\text{dof}}$
$14^3 \times 28$	0.559(8)	3.99-5.27	2.7/6.0
$16^3 \times 32$	0.644(10)	3.92-4.95	1.7/6.0
Interp.	0.635(5)	3.97-4.93	1.4/6.0

Figure 10 and the fitting results of the slope in Table 9 demonstrate that the renormalized chiral condensate that is calculated from the scale parameter Σ decreases in direct proportion to the square root of the number density of the instantons and anti-instantons; however, the fitting results of the slope indicate that the effects of the finite lattice volume on the slope values appear and the interpolated results are not consistent with the prediction (29). Therefore, in the sections below, we improve the calculations of the observables by matching the numerical results with the experimental results.

5 Instanton effects

We perform simulations in the quenched QCD. Therefore, to compare the observables that are numerically computed

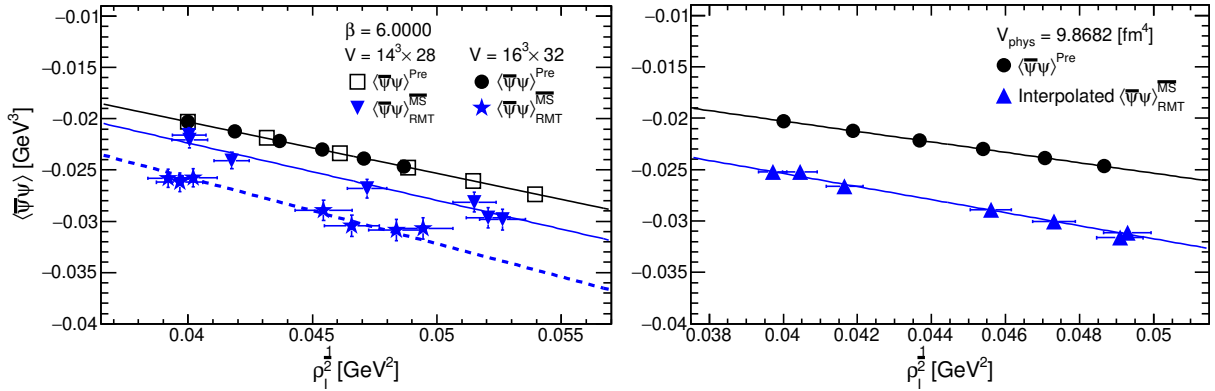


Fig. 10. Comparisons of the renormalized chiral condensate $\langle \bar{\psi}\psi \rangle_{\text{RMT}}^{\overline{\text{MS}}}$ in the $\overline{\text{MS}}$ -scheme at 2 [GeV] of the configurations of $\beta = 6.0000$, $V = 14^3 \times 28$ and $V = 16^3 \times 32$ (left) and the interpolated results at the continuum limit (right) with the predictions $\langle \bar{\psi}\psi \rangle^{\text{Pre}}$. In the left figure, the black full, the blue full, and the blue dashed lines indicate the fitting results of the predictions, the numerical results of $V = 14^3 \times 28$, and $V = 16^3 \times 32$, respectively. In the right figure, the black full line and the blue full line indicate the fitting results of the prediction and the interpolated results, respectively.

with the experimental results, we determine the normalization factor by matching the experimental results with the numerical results. We quantitatively evaluate the effects of the instanton and anti-instantons created by the additional monopoles and anti-monopoles on the renormalized chiral condensate, the renormalized average mass of the light quarks, decay constants, and pion mass. Finally, the catalytic effect of the pion decay is estimated using the interpolated outcomes at the continuum limit of the pion mass and pion decay constant as input values.

5.1 Matching the decay constant and mass of the pseudoscalar meson with the experimental outcomes

We cannot determine the physical quantities or directly compare the numerical results with the experiments without using the outcomes of the chiral perturbation theory or experiments because our calculations are performed in the quenched SU(3). Therefore, we improve the computations in reference [59, 62] to remove the ambiguities coming from the determinations of the lattice scales. We use the calculated results of the lattice spacing by the analytic formula in Table 1 as lattice scales, determine the normalization factor Z_π using the experimental outcomes, and calculate the observables using the normalization factor.

In this study, we calculate the observables of the configurations with the additional monopoles and anti-monopoles using the normalization factor Z_π calculated for each standard configuration.

First, we calculate the decay constant of the pseudoscalar meson aF_{PS} using the fitting results of the coefficient a^4G_{P-S} and the results of the square mass of the pseudoscalar meson $(am_{PS})^2$ as follows:

$$aF_{PS} = \frac{2a\bar{m}_{ud}\sqrt{a^4G_{P-S}}}{(am_{PS})^2} \quad (32)$$

The pion decay constant is $F_\pi = 93$ [MeV] in this notation. The calculated results of the decay constant of aF_{PS} are

listed in the same tables as the fitting results of a^4G_{P-S} and am_{PS} mentioned in subsection 4.1. We define the decay constant of the pseudoscalar meson at the chiral limit f_0 as follows:

$$af_0 \equiv \lim_{a\bar{m}_{ud} \rightarrow 0} aF_{PS} = \lim_{(am_{PS})^2 \rightarrow 0} aF_{PS} \quad (33)$$

The third term holds because the PCAC relation holds even if we add the monopoles and anti-monopoles with the magnetic charges to the configurations.

In the studies using the overlap Dirac operator in the quenched SU(3), there is a linear relationship between the decay constant and square mass of the pseudoscalar meson. This behavior corresponds to the features of the SU(2) Lagrangian in the quenched chiral perturbation theory [63], which was reported by other groups [64, 65].

Therefore, we plot the numerical results of the decay constant and square mass of the pseudoscalar meson, confirm the linear relationship between them without divergence near the chiral limit, and then fit the following linear function to the numerical results:

$$aF_{PS} = a^{-1}A_{PS}(am_{PS})^2 + aB_{PS}. \quad (34)$$

The fitting results of the slope $a^{-1}A_{PS}$, intercept aB_{PS} , and χ^2/dof are presented in Table 50 in G. The fitting results of χ^2/dof are less than 1; thus, these results indicate that the decay constant of the pseudoscalar meson aF_{PS} linearly increases with its square mass $(am_{PS})^2$ without divergence near the chiral limit.

To determine the normalization factor Z_π , we first make a curve using the experimental outcomes of the pion decay constant and pion mass as follows:

$$aF_{PS} = am_{PS}C_\pi^{\text{Exp}}, \quad C_\pi^{\text{Exp}} = \frac{F_{\pi^-}^{\text{Exp}}}{m_{\pi^\pm}^{\text{Exp}}\sqrt{2}}. \quad (35)$$

Here we use the following outcomes of the pion decay constant and pion mass reported in reference [66]:

$$\frac{F_{\pi^-}^{\text{Exp}}}{\sqrt{2}} = \frac{130.50(12)}{\sqrt{2}} \text{ [MeV]}, \quad (36)$$

$$m_{\pi^\pm}^{\text{Exp}} = 139.5706(2) \text{ [MeV]}. \quad (37)$$

Next, we calculate the intersections aF_{PS}^π and am_{PS}^π between the curve (35) and the linear functions made using the fitting results of the slope $a^{-1}A_{PS}$ and intercept aB_{PS} . The normalization factor Z_π is determined for each lattice using the intersections of the standard configuration and the experimental outcomes of the pion decay constant (36) or pion mass (37) as follows:

$$Z_\pi = \frac{92.277}{F_{PS}^\pi} = \frac{139.5706}{m_{PS}^\pi} \quad (38)$$

Here we do not consider the errors of the experimental outcomes because their errors are substantially smaller than the errors of the numerical results. The computed results of the intersections aF_{PS}^π and am_{PS}^π are in Table 50 in G, and the normalization factor Z_π of the standard configurations are in Table 10.

Table 10. The calculated results of the normalization factor Z_π using the standard configurations.

β	V	Z_π
5.8457	$12^3 \times 24$	1.24(3)
5.9256	$14^3 \times 28$	1.26(2)
6.0000	$14^3 \times 28$	1.31(2)
	$16^3 \times 32$	1.294(19)
6.1366	$20^3 \times 40$	1.270(18)

Next, we define the decay constant at the chiral limit aF_0 using the normalization factor Z_π of the standard configuration and the fitting results of the intercept aB_{PS} as follows:

$$aF_0 \equiv Z_\pi a f_0 = Z_\pi a B_{PS} \quad (39)$$

The numerical results of the decay constant at the chiral limit in Table 51 in H show that there are no influences of the discretization or finite lattice volume on the numerical results. Therefore, that demonstrates that we can compute the observables using the normalization factor Z_π without harmful influences of the finite lattice volume or the discretization on the observables. We then fit the constant function to interpolate the results to the continuum limit and list the fitting results in Table 11.

The prediction of the decay constant F_0^{Pre} at the chiral limit using the Gell-Mann-Oakes-Renner (GMOR) relation [67] and the prediction of the chiral condensate (29) is given in [41] as follows:

$$F_0^{\text{Pre}}(m_c) = \frac{1}{m_\pi} \left(\frac{2\bar{m}_{ud}}{\bar{\rho}} \right)^{\frac{1}{2}} \left(\frac{\pi N_c}{13.2} \right)^{\frac{1}{4}} \left(\rho_I^{\text{sta}} + \frac{m_c}{V_{\text{phys}}} \right)^{\frac{1}{4}}. \quad (40)$$

Table 11. Comparing the interpolated results F_0^{int} of the decay constant at the continuum limit with the prediction F_0^{Pre} .

m_c	F_0^{Pre} [MeV]	F_0^{int} [MeV]	FR: a^2 [fm ²] $\times 10^{-2}$	$\frac{\chi^2}{\text{dof}}$
N. C.	85.366	90.6(9)	5.5-15.5	0.0/4.0
0	85.366	90.8(1.1)	7.2-15.5	0.2/3.0
1	87.345	92.6(1.1)	7.2-15.5	0.0/3.0
2	89.199	96.3(1.2)	7.2-15.5	0.4/3.0
3	90.943	97.5(1.2)	7.2-15.5	0.7/3.0
4	92.593	99.2(1.1)	5.5-11.4	2.3/3.0
5	94.159	100.0(1.1)	5.5-11.4	1.2/3.0

The prediction of the normal configuration calculated by this formula is $F_0^{\text{Pre}}(0) = 85.366$ [MeV]. This outcome is consistent with the prediction in the chiral perturbation theory $F_0^{\chi PT} = 86.2(5)$ [MeV] [68]. The prediction F_0^{Pre} of the decay constant at the chiral limit for each magnetic charge is given in Table 11 and Table 51 in H.

Last, we have already reported that the decay constant at the chiral limit increases in direct proportion to the one-fourth root of the number density of the instantons and anti-instantons in our previous study [41]; accordingly, to compare the computed results of the decay constant at the chiral limit with the predictions, we fit the following linear function as shown in Fig. 11:

$$F_0 = A_{F_0} x, \quad x = \rho_I^{\frac{1}{4}} \text{ [MeV]}. \quad (41)$$

The prediction of the slope is $A_{F_0}^{\text{Pre}} = 0.4268$. The fitting results of the slope of the numerical results are 5~7% steeper than the prediction indicated in Table 12; however, there is no influence of the finite lattice volume on the slope. Therefore, the results demonstrate that the decay constant at the chiral limit increases in direct proportion to the one-fourth root of the number density of the instanton and anti-instantons.

Table 12. Comparisons of the fitting results. The fitting results are obtained by the linear curves $F_0 = A_{F_0} x$, ($x = \rho_I^{\frac{1}{4}}$ [MeV]). The configurations of $\beta = 6.0000$, $V = 14^3 \times 28$ and $V = 16^3 \times 32$ and the interpolated results are used.

Conf	A_{F_0}	FR: $\rho_I^{\frac{1}{4}}$ [MeV] $\times 10^2$	$\frac{\chi^2}{\text{dof}}$
$14^3 \times 28$	0.450(4)	1.99-2.30	0.9/6.0
$16^3 \times 32$	0.457(4)	1.97-2.23	0.7/6.0
Interp.	0.451(2)	1.99-2.23	1.4/6.0

5.2 Instanton effects on chiral symmetry breaking

The chiral condensate at the chiral limit is derived using the fitting results of the slope $aA_{\text{PCAC}}^{(2)}$ of the PCAC relation and the decay constant of the pseudoscalar meson at

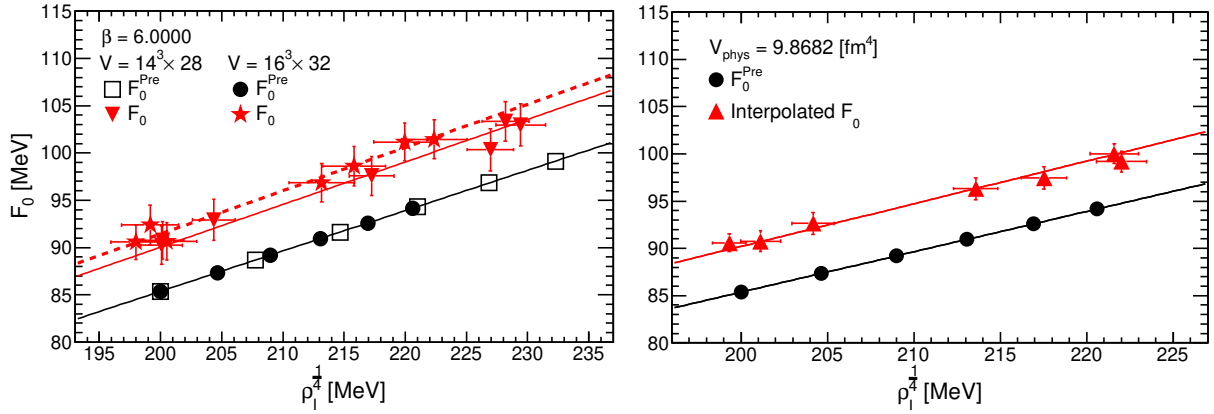


Fig. 11. Comparisons of the decay constant F_0 at the chiral limit of the configurations of $\beta = 6.0000$, $V = 14^3 \times 28$ and $V = 16^3 \times 32$ (left) and the interpolated results at the continuum limit (right) with the predictions F_0^{Pre} . In the left figure, the black full, the red full, and the red dashed lines indicate the fitting results of the predictions, the numerical results of $V = 14^3 \times 28$, and $V = 16^3 \times 32$, respectively. In the right figure, the black full line and the red full line indicate the fitting results of the prediction and the interpolated results, respectively.

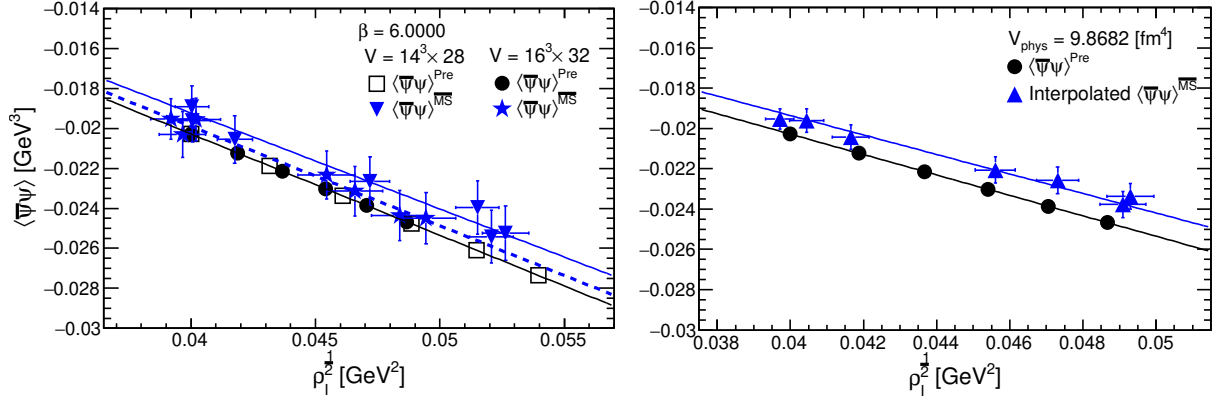


Fig. 12. Comparisons of the renormalized chiral condensate $\langle \bar{\psi}\psi \rangle^{\overline{\text{MS}}}$ in the $\overline{\text{MS}}$ -scheme at 2 [GeV] of the configurations of $\beta = 6.0000$, $V = 14^3 \times 28$ and $V = 16^3 \times 32$ (left) and the interpolated results at the continuum limit (right) with the predictions $\langle \bar{\psi}\psi \rangle^{\text{Pre}}$. In the left figure, the black full, the blue full, and the blue dashed lines indicate the fitting results of the predictions, the numerical results of $V = 14^3 \times 28$, and $V = 16^3 \times 32$, respectively. In the right figure, the black full line and the blue full line indicate the fitting results of the prediction and the interpolated results, respectively.

the chiral limit (39) as follows:

$$a^3 \langle \bar{\psi}\psi \rangle = -\frac{aA_{\text{PCAC}}^{(2)}}{2} (aF_0)^2 \quad (42)$$

The renormalized chiral condensate in the $\overline{\text{MS}}$ -scheme at 2 [GeV] is evaluated as follows:

$$\langle \bar{\psi}\psi \rangle^{\overline{\text{MS}}} (2 \text{ [GeV]}) = \frac{\hat{Z}_S}{0.72076} \langle \bar{\psi}\psi \rangle \quad (43)$$

We use each numerical result of the renormalization constant \hat{Z}_S calculated for each lattice and configuration type, as mentioned in subsection 4.3. The numerical results of the renormalized chiral condensate in the $\overline{\text{MS}}$ -scheme at 2 [GeV] are listed in Table 51 in H.

Table 51 in H shows that the numerical results of the renormalized chiral condensate are consistent without the

discretization influence by using the normalization factor; therefore, we interpolate the calculated results to the continuum limit by fitting the constant function. The fitting results are given in Table 13. This table shows that the fitting results of χ^2/dof are less than 0.5 and that the interpolated results are reasonably consistent with the prediction; therefore, the influence of the discretization is negligible.

To confirm that the influence of the finite lattice volume is improved, we compare the slope values of the numerical results with the prediction by fitting the following linear function as shown in the left panel of Fig. 12:

$$\langle \bar{\psi}\psi \rangle = -A_{\langle \bar{\psi}\psi \rangle} x, \quad x = \rho_I^{\frac{1}{2}} \text{ [GeV}^2\text{]}. \quad (44)$$

The fitting results of the slope $A_{\langle \bar{\psi}\psi \rangle}$ of the lattice volumes $V = 14^3 \times 28$ and $V = 16^3 \times 32$ of $\beta = 6.0000$ in Table 14 are consistent with the prediction $A_{\langle \bar{\psi}\psi \rangle}^{\text{Pre}} = 0.5070 \text{ [GeV]}$;

Table 13. The prediction $\langle\bar{\psi}\psi\rangle^{\text{Pre}}$, interpolated results $\langle\bar{\psi}\psi\rangle_{\overline{\text{MS}}}^{\text{int}}$ at the continuum limit by the constant function, and the fitting results.

m_c	$\langle\bar{\psi}\psi\rangle^{\text{Pre}}$ [GeV ³] $\times 10^{-2}$	$\langle\bar{\psi}\psi\rangle_{\overline{\text{MS}}}^{\text{int}}$ [GeV ³] $\times 10^{-2}$	FR: a^2 [fm ²] $\times 10^{-2}$	$\frac{\chi^2}{\text{dof}}$
N. C.	-2.0280	-1.95(5)	5.5-15.5	0.0/4.0
0	-2.0280	-1.96(6)	7.2-15.5	0.2/3.0
1	-2.1231	-2.04(6)	7.2-15.5	0.0/3.0
2	-2.2142	-2.21(6)	7.2-15.5	0.2/3.0
3	-2.3016	-2.26(7)	7.2-15.5	0.5/3.0
4	-2.3859	-2.34(6)	5.5-11.4	1.5/3.0
5	-2.4672	-2.38(6)	5.5-11.4	0.8/3.0

thus, there is no influence of the finite lattice volume on the renormalized chiral condensate in the $\overline{\text{MS}}$ -scheme at 2 [GeV].

Table 14. The fitting results of the slope $A_{\langle\bar{\psi}\psi\rangle}$ obtained by the linear curves $\langle\bar{\psi}\psi\rangle = -A_{\langle\bar{\psi}\psi\rangle}x$, ($x = \rho_I^{\frac{1}{2}}$ [GeV²]). The configurations of the lattice volumes $V = 14^3 \times 28$ and $V = 16^3 \times 32$ of $\beta = 6.0000$ and the interpolated results are used.

Conf	$A_{\langle\bar{\psi}\psi\rangle}$ [GeV]	FR: $\rho_I^{\frac{1}{2}}$ [GeV ²] $\times 10^{-2}$	$\frac{\chi^2}{\text{dof}}$
$14^3 \times 28$	0.481(10)	3.99-5.27	0.7/6.0
$16^3 \times 32$	0.497(11)	3.92-4.95	0.5/6.0
Interp.	0.484(6)	3.97-4.93	1.0/6.0

Next, we compare the slope value of the interpolated results with the prediction as shown in the right panel of Fig. 12. The slope value of the interpolated results that is presented in Table 14 is consistent with the prediction of the slope $A_{\langle\bar{\psi}\psi\rangle}^{\text{Pre}} = 0.5070$ [GeV].

These results demonstrate that the renormalized chiral condensate in the $\overline{\text{MS}}$ -scheme at 2 [GeV] decreases in direct proportion to the square root of the number density of the instantons and anti-instantons, with neither the influences of the finite lattice volume nor the discretization.

In addition, we estimate the inverse of the average size of the instanton from the slope value of the interpolated result as follows:

$$\frac{1}{\rho} = 5.73(7) \times 10^2 \text{ [MeV]} \quad (45)$$

This result is compatible with the outcome of the phenomenological model (30) and indicates that the additional monopoles and anti-monopoles do not change the average size of the instanton or anti-instanton. Moreover, we have already mentioned that the interpolated result of the number density of the instantons and anti-instantons computed using the standard configurations is consistent with the outcome (5) of the phenomenological model in subsection 2.3.

Finally, these results demonstrate that the instantons and anti-instantons created by the additional monopoles and anti-monopoles induce chiral symmetry breaking and the features are consistent with the phenomenological models concerning the instantons [28, 29].

5.3 Instanton effects on the light quark masses

We have quantitatively demonstrated that the absolute value of the renormalized chiral condensate in the $\overline{\text{MS}}$ -scheme at 2 [GeV] increases in direct proportion to the square root of the number density of the instantons and anti-instantons. The quark-mass generation is closely related to chiral symmetry breaking; therefore, suppose that the quark masses become heavy in direct proportion to the square root of the number density of the instantons and anti-instantons [41].

In this study, we estimate the average mass of the up and down quarks using the computed results of the intersection am_{PS}^{π} in Table 50 in G, normalization factor Z_{π} in Table 10, and the fitting results of the slope value $aA^{(2)}$ of the PCAC relation in Table 49 in F as follows:

$$a\bar{m}_{ud} = \frac{(Z_{\pi}am_{PS}^{\pi})^2}{aA^{(2)}} \quad (46)$$

The renormalized average mass of the up and down quarks is evaluated in the $\overline{\text{MS}}$ -scheme at 2 [GeV] using the renormalization constant \hat{Z}_S for the scalar density in Table 49 in F as follows:

$$\hat{m}_{ud}^{\overline{\text{MS}}} = \frac{0.72076}{\hat{Z}_S} \bar{m}_{ud} \quad (47)$$

We use each result of the renormalization constant for the scalar density calculated for each type of configuration. The calculated results of the renormalized average mass $\hat{m}_{ud}^{\overline{\text{MS}}}$ in the $\overline{\text{MS}}$ -scheme at 2 [GeV] are in Table 51 in H and they show no influence of the discretization. Therefore, we fit the calculated results by the constant function, obtain the interpolated results at the continuum limit, and list them in Table 15.

Table 15. Comparing the interpolated results $\hat{m}_{ud}^{\overline{\text{MS}},\text{int}}$ at the continuum limit with the prediction $\bar{m}_{ud}^{\text{Pre}}$ together with the fitting results.

m_c	$\bar{m}_{ud}^{\text{Pre}}$ [MeV]	$\hat{m}_{ud}^{\overline{\text{MS}},\text{int}}$ [MeV]	FR: a^2 [fm ²] $\times 10^{-2}$	$\frac{\chi^2}{\text{dof}}$
N. C.	$3.5_{-0.3}^{+0.7}$	4.09(10)	5.5-15.5	0.0/4.0
0	$3.5_{-0.3}^{+0.7}$	4.11(12)	7.2-15.5	0.2/3.0
1	$3.7_{-0.3}^{+0.7}$	4.28(13)	7.2-15.5	0.0/3.0
2	$3.8_{-0.3}^{+0.8}$	4.63(14)	7.2-15.5	0.2/3.0
3	$4.0_{-0.3}^{+0.8}$	4.74(14)	7.2-15.5	0.5/3.0
4	$4.1_{-0.4}^{+0.8}$	4.90(14)	5.5-11.4	1.4/3.0
5	$4.3_{-0.4}^{+0.9}$	4.98(14)	5.5-11.4	0.7/3.0

We assume that the average mass of the light quarks becomes heavy in direct proportion to the square root of

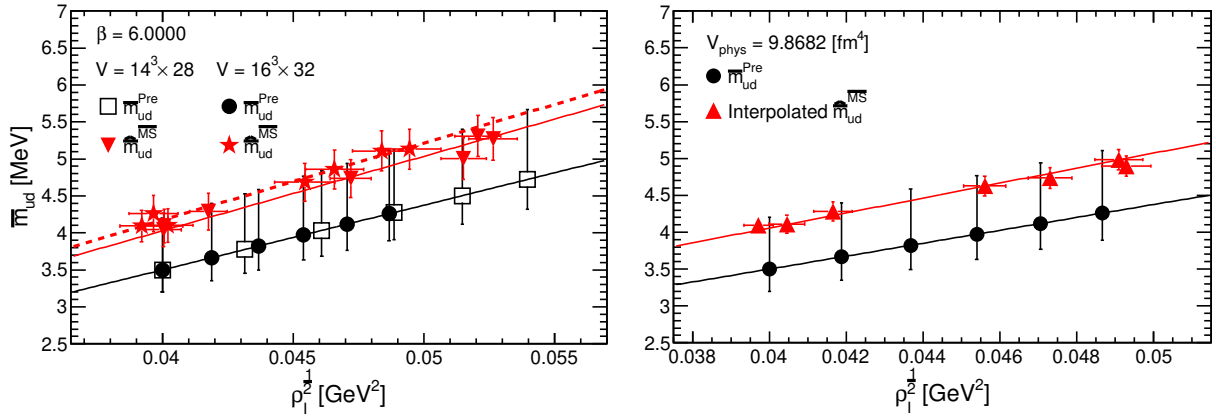


Fig. 13. Comparisons of the renormalized average quark mass $\hat{m}_{ud}^{\overline{\text{MS}}}$ in the $\overline{\text{MS}}$ -scheme at 2 [GeV] of the configurations of $V = 14^3 \times 28$ and $V = 16^3 \times 32$ of $\beta = 6.0000$ (left) and the interpolated results at the continuum limit (right) with the predictions $\bar{m}_{ud}^{\text{Pre}}$. In the left figure, the black full, the red full, and the red dashed lines indicate the fitting results of the predictions, the numerical results of $V = 14^3 \times 28$, and $V = 16^3 \times 32$, respectively. In the right figure, the black full line and the red full line indicate the fitting results of the prediction and the interpolated results, respectively.

the number density of the instantons and anti-instantons; accordingly, we give the following prediction concerning the average mass of the light quarks using the predictions (5), (9), and experimental outcome $\bar{m}_{ud}^{\text{Exp}}$ of the average mass of the light quarks:

$$\bar{m}_{ud}^{\text{Pre}}(m_c) = \bar{m}_{ud}^{\text{Exp}} \left[\frac{\rho_I^{\text{Pre}}(m_c)}{\rho_I^{\text{sta}}} \right]^{\frac{1}{2}}. \quad (48)$$

Here, the experimental outcome is $\bar{m}_{ud}^{\text{Exp}} = 3.5^{+0.7}_{-0.3}$ [MeV] [66]. The predictions are given in Table 15 and Table 51 in H.

In order to quantitatively demonstrate the increase in the average mass of the light quarks to the increase in the square root of the number density of the instantons and anti-instantons, we plot the numerical results and predictions and fit them by the following linear function, as shown in Fig. 13:

$$\bar{m}_{ud} = A_{\bar{m}_{ud}} x, \quad x = \rho_I^{\frac{1}{2}} \text{ [GeV}^2\text{]}. \quad (49)$$

The slope values $A_{\bar{m}_{ud}}$ of the lattice volumes $V = 14^3 \times 28$ and $V = 16^3 \times 32$ and the interpolated results are 15% steeper than the prediction, as shown in Table 16; however, there are no influences of the finite lattice volume on the slope values.

Thus, the renormalized average mass of the up and down quarks in the $\overline{\text{MS}}$ -scheme at 2 [GeV] becomes heavy in direct proportion to the square root of the number density of the instantons and anti-instantons, without any influences of the finite lattice volume or discretization. The increase in the average mass of the quarks is almost the same as the increase in the absolute value of the chiral condensate. We will quantitatively evaluate the decrease and increases in the observables in subsection 5.5.

Table 16. The fitting results of the numerical results and prediction. The linear curve is $\bar{m}_{ud} = A_{\bar{m}_{ud}} x$, ($x = \rho_I^{\frac{1}{2}}$ [GeV²]). The configurations of the lattice volumes $V = 14^3 \times 28$ and $V = 16^3 \times 32$ of $\beta = 6.0000$ and the interpolated results are used.

Conf	$A_{\bar{m}_{ud}}$ [MeV ⁻¹] $\times 10^{-4}$	FR: $\rho_I^{\frac{1}{2}}$ [GeV ²]	$\frac{\chi^2}{\text{dof}}$
Pred.	0.88(4)	3.99-5.40	0.0/5.0
$14^3 \times 28$	1.01(2)	3.99-5.27	0.6/6.0
$16^3 \times 32$	1.04(2)	3.92-4.95	0.5/6.0
Interp.	1.014(12)	3.97-4.93	1.1/6.0

5.4 Instanton effects on the pion mass and pion decay constant

The pion mass am_π and pion decay constant aF_π are estimated using the normalization factor Z_π in Table 10 and the intersections am_{PS}^π and aF_{PS}^π in Table 50 in G as follows:

$$am_\pi = Z_\pi am_{PS}^\pi \quad (50)$$

$$aF_\pi = Z_\pi aF_{PS}^\pi \quad (51)$$

The discretization does not affect the numerical results of the pion mass, pion decay constant, and ratio of the decay constants $\frac{F_\pi}{F_0}$, as shown in Table 51 in H. Moreover, the table shows that the calculated results of the ratio $\frac{F_\pi}{F_0}$ do not change even if we add the monopoles and anti-monopoles to the configurations; therefore, we fit the constant function to the numerical results of the pion mass and pion decay constant. The fitting results in Tables 17 and 18 show that the values of χ^2/dof are small enough and the interpolated results of the pion mass and decay constant are reasonably consistent with their predictions.

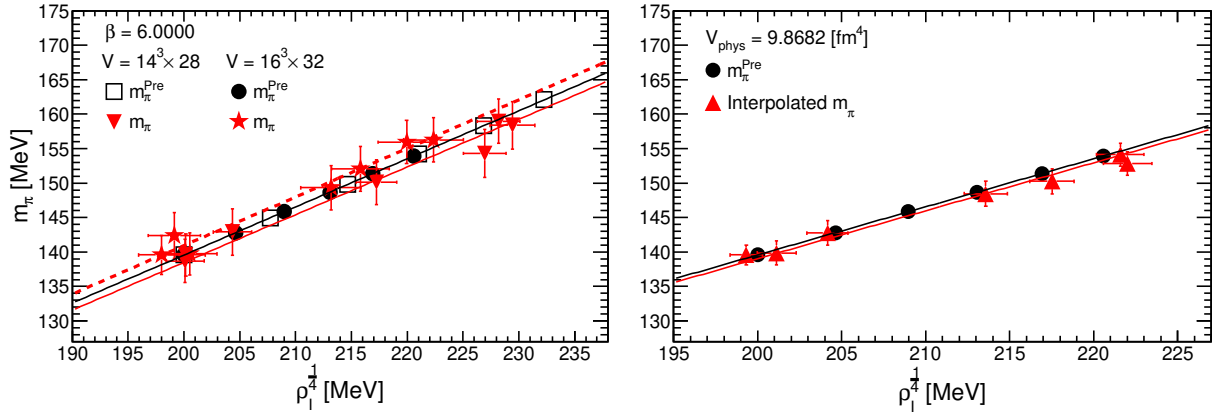


Fig. 14. Comparisons of the pion mass m_π of the configurations of $\beta = 6.0000$, $V = 14^3 \times 28$ and $V = 16^3 \times 32$ (left) and the interpolated results at the continuum limit (right) with the predictions m_π^{Pre} . In the left figure, the black full line, the red full line, and the red dashed line indicate the fitting results of the predictions, the numerical results of $V = 14^3 \times 28$, and $V = 16^3 \times 32$, respectively. In the right figure, the black full line and the red full line indicate the fitting results of the prediction and the interpolated results, respectively.

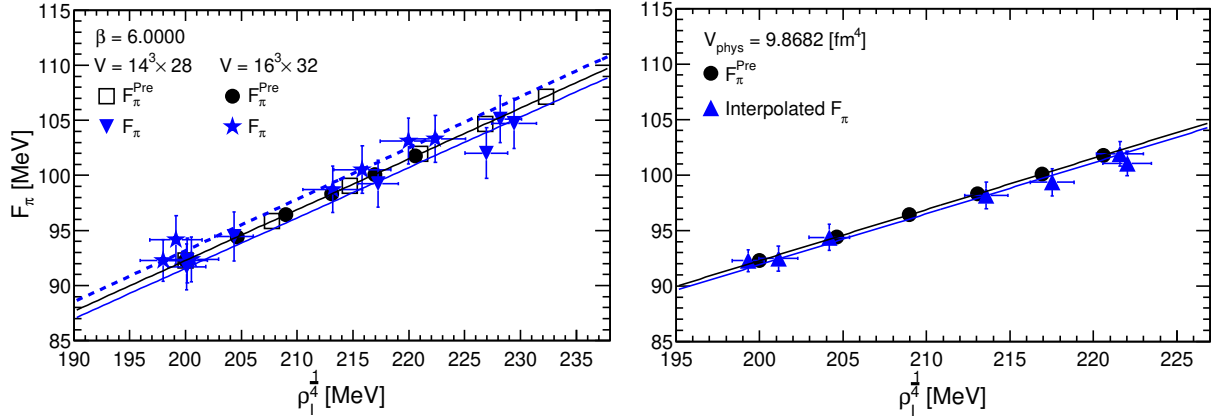


Fig. 15. Comparisons of the pion decay constant F_π of the configurations of $\beta = 6.0000$, $V = 14^3 \times 28$ and $V = 16^3 \times 32$ (left) and the interpolated results at the continuum limit (right) with the predictions F_π^{Pre} . In the left figure, the black full, the blue full, and the blue dashed lines indicate the fitting results of the predictions, the numerical results of $V = 14^3 \times 28$, and $V = 16^3 \times 32$, respectively. In the right figure, the black full and the blue full lines indicate the fitting results of the prediction and the interpolated results, respectively.

We have shown that the average mass of the up and down quarks becomes heavy in direct proportion to the square root of the number density of the instantons and anti-instantons. Moreover, the PCAC relation holds even if the monopoles and anti-monopoles are added to the configurations. These outcomes predict that the pion mass becomes heavy in direct proportion to the one-fourth root of the number density of the instantons and anti-instantons. Therefore, similar to the prediction concerning the average mass of the light quarks, we give the following prediction concerning the pion mass using the experimental outcome (37):

$$m_\pi^{\text{Pre}}(m_c) = m_{\pi^\pm}^{\text{Exp}} \left[\frac{\rho_I^{\text{Pre}}(m_c)}{\rho_I^{\text{sta}}} \right]^{\frac{1}{4}}. \quad (52)$$

In addition, we have demonstrated that the decay constant of the pseudoscalar meson linearly increases with the increase in the square of the pseudoscalar mass. The decay constant of the pseudoscalar meson at the chiral limit increases in direct proportion to the one-fourth root of the number density of the instantons and anti-instantons. These quantitative relations indicate that the pion decay constant also increases in direct proportion to the one-fourth root of the number density of the instantons and anti-instantons. Therefore, we give the following prediction concerning the pion decay constant using the experimental outcome (36):

$$F_\pi^{\text{Pre}}(m_c) = \frac{F_{\pi^-}^{\text{Exp}}}{\sqrt{2}} \left[\frac{\rho_I^{\text{Pre}}(m_c)}{\rho_I^{\text{sta}}} \right]^{\frac{1}{4}}. \quad (53)$$

Table 17. The prediction of the pion mass m_π^{Pre} , interpolated results of the pion mass m_π^{int} , and fitting results.

m_c	m_π^{Pre} [MeV] $\times 10^2$	m_π^{int} [MeV] $\times 10^2$	FR: a^2 [fm ²] $\times 10^{-2}$	$\frac{\chi^2}{\text{dof}}$
N. C.	1.395706(2)	1.396(14)	5.5-15.5	0.0/4.0
0	1.395706(2)	1.399(17)	7.2-15.5	0.3/3.0
1	1.428069(2)	1.428(18)	7.2-15.5	0.0/3.0
2	1.458370(2)	1.485(18)	7.2-15.5	0.4/3.0
3	1.486892(2)	1.503(18)	7.2-15.5	0.7/3.0
4	1.513862(2)	1.528(16)	5.5-11.4	2.2/3.0
5	1.539462(2)	1.541(17)	5.5-11.4	1.2/3.0

Table 18. The prediction of the pion decay constant F_π^{Pre} , interpolated results of the pion decay constant F_π^{int} , and fitting results.

m_c	F_π^{Pre} [MeV]	F_π^{int} [MeV]	FR: a^2 [fm ²] $\times 10^{-2}$	$\frac{\chi^2}{\text{dof}}$
N. C.	92.28(9)	92.3(1.0)	5.5-15.5	0.0/4.0
0	92.28(9)	92.5(1.1)	7.2-15.5	0.3/3.0
1	94.42(9)	94.4(1.2)	7.2-15.5	0.0/3.0
2	96.42(9)	98.2(1.2)	7.2-15.5	0.4/3.0
3	98.31(9)	99.3(1.2)	7.2-15.5	0.7/3.0
4	100.09(9)	101.1(1.1)	5.5-11.4	2.2/3.0
5	101.78(9)	101.9(1.1)	5.5-11.4	1.2/3.0

The predictions concerning m_π^{Pre} and F_π^{Pre} are listed in Table 17 and Table 51 in H.

Finally, we fit the following linear functions to the numerical results of the pion mass and pion decay constant and their predictions, as shown in Figs. 14 and 15:

$$m_\pi = A_{m_\pi} x, \quad x = \rho_I^{\frac{1}{4}} \text{ [MeV]}, \quad (54)$$

$$F_\pi = A_{F_\pi} x, \quad x = \rho_I^{\frac{1}{4}} \text{ [MeV]}. \quad (55)$$

The fitting results concerning the pion mass and the pion decay constant are presented in Tables 19 and 20, respectively.

The fitting results concerning the pion mass and the pion decay constant of the lattice volumes $V = 14^3 \times 28$ and $V = 16^3 \times 32$ of $\beta = 6.0000$ in Tables 19 and 20 indicate that there is no influence of the finite lattice volume and that the slope values are consistent with the predictions. Furthermore, the fitting results of the slopes of the interpolated results in Tables 19 and 20 are consistent with the slope values of the predictions. These results show that the pion mass and pion decay constant increase in direct proportion to the one-fourth root of the number density of the instantons and anti-instantons without the influence of the finite lattice volume or discretization.

5.5 Evaluations of the proportions

We calculate the ratios of the observables to quantitatively evaluate the decrease and increase in the observables to

Table 19. Comparisons of the fitting results of the slope A_{m_π} obtained by the linear function $m_\pi = A_{m_\pi} x$, ($x = \rho_I^{\frac{1}{4}}$ [MeV]). The configurations of the lattice volumes $V = 14^3 \times 28$ and $V = 16^3 \times 32$ of $\beta = 6.0000$ and the interpolated results are used.

Conf	A_{m_π}	FR: $\rho_I^{\frac{1}{4}}$ [MeV] $\times 10^2$	$\frac{\chi^2}{\text{dof}}$
Pred.	0.697853(4)	1.99-2.33	0.0/5.0
$14^3 \times 28$	0.693(6)	1.99-2.30	0.9/6.0
$16^3 \times 32$	0.705(6)	1.97-2.23	0.6/6.0
Interp.	0.695(3)	1.99-2.23	1.4/6.0

Table 20. Comparisons of the fitting results of the slope A_{F_π} obtained by the linear function $F_\pi = A_{F_\pi} x$, ($x = \rho_I^{\frac{1}{4}}$ [MeV]). The configurations of the lattice volumes $V = 14^3 \times 28$ and $V = 16^3 \times 32$ of $\beta = 6.0000$ and the interpolated results are used.

Conf	A_{F_π}	FR: $\rho_I^{\frac{1}{4}}$ [MeV] $\times 10^2$	$\frac{\chi^2}{\text{dof}}$
Pred.	0.46140(17)	1.99-2.33	0.0/5.0
$14^3 \times 28$	0.458(4)	1.99-2.30	0.9/6.0
$16^3 \times 32$	0.466(4)	1.97-2.23	0.6/6.0
Interp.	0.460(2)	1.99-2.23	1.4/6.0

the increase in the number density of the instantons and anti-instantons without suffering uncertainties from the renormalization constant, normalization factor, and lattice scale. The ratios are defined as follows:

$$R_{\text{obs}}(m_c) = \frac{\langle \mathcal{O}(m_c) \rangle}{\langle \mathcal{O}^{\text{sta}} \rangle} \quad (56)$$

The numerator $\langle \mathcal{O}(m_c) \rangle$ indicates the observables that are calculated using the configurations with the additional monopoles and anti-monopoles of the magnetic charges m_c . The denominator $\langle \mathcal{O}^{\text{sta}} \rangle$ refers to the observables that are calculated using the standard configurations.

The ratios are predicted using the predictions concerning the chiral condensate (29) and the decay constant of the pseudoscalar at the chiral limit (40) as follows:

1. When the observable increases in direct proportion to the square root of the number density of the instantons and anti-instantons, the ratio (56) equals

$$\left[\frac{N_I(m_c)}{N_I^{\text{sta}}} \right]^{\frac{1}{2}} \equiv R_{N_I}^{\frac{1}{2}}. \quad (57)$$

2. When the observable increases in direct proportion to the one-fourth root of the number density of the instantons and anti-instantons, the ratio (56) equals

$$\left[\frac{N_I(m_c)}{N_I^{\text{sta}}} \right]^{\frac{1}{4}} \equiv R_{N_I}^{\frac{1}{4}}. \quad (58)$$

We plot the ratios concerning the numbers of instantons and anti-instantons along the horizontal axis and the ratio

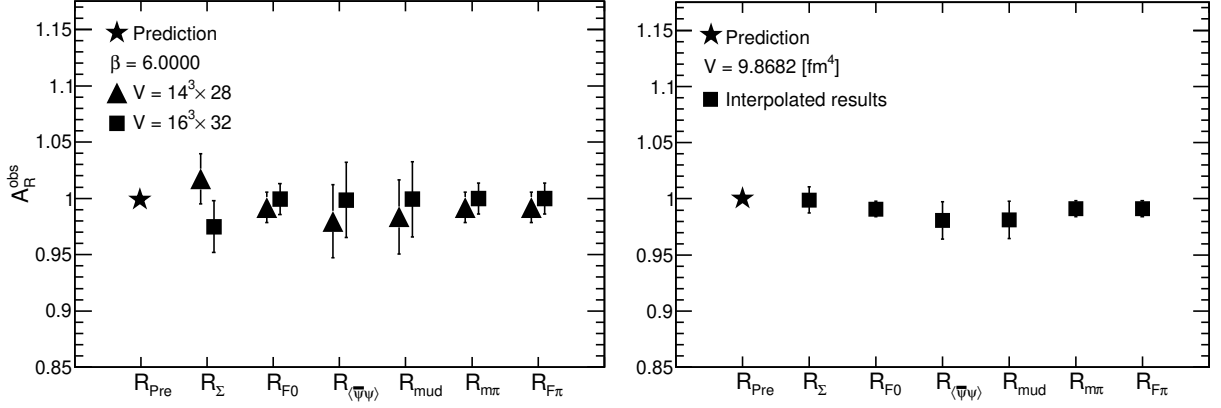


Fig. 16. Comparing the prediction with the fitting results of the slopes A_R^{obs} to the ratios R_{obs} . The configurations of $V = 14^3 \times 28$ and $V = 16^3 \times 32$ of $\beta = 6.0000$ (left) and the interpolated results (right).

Table 21. The fitting results of the slopes A_R^{obs} obtained by the linear functions $R_{\text{obs}} = A_R^{\text{obs}} R_{N_I}^{\frac{1}{2}}$ and $R_{\text{obs}} = A_R^{\text{obs}} R_{N_I}^{\frac{1}{4}}$. The ratios are computed using the results of the configurations of the lattice volumes $V = 14^3 \times 28$ and $V = 16^3 \times 32$ of $\beta = 6.0000$ and the interpolated results. The prediction of the slope values is $A_R^{\text{Pre}} = 1$.

Conf	Obs.	A_R^{obs}	FR	$\frac{\chi^2}{\text{dof}}$
$14^3 \times 28$	Σ_{RMT}	1.02(2)	$R_{N_I}^{\frac{1}{2}} : 0.99-1.32$	1.2/5.0
	F_0	0.992(13)	$R_{N_I}^{\frac{1}{4}} : 0.99-1.15$	0.4/5.0
	$\langle \bar{\psi}\psi \rangle$	0.98(3)	$R_{N_I}^{\frac{1}{2}} : 0.99-1.32$	0.3/5.0
	\hat{m}_{ud}	0.98(3)	$R_{N_I}^{\frac{1}{2}} : 0.99-1.32$	0.3/5.0
	m_π	0.992(14)	$R_{N_I}^{\frac{1}{4}} : 0.99-1.15$	0.4/5.0
	F_π	0.992(14)	$R_{N_I}^{\frac{1}{4}} : 0.99-1.15$	0.4/5.0
$16^3 \times 32$	Σ_{RMT}	0.97(2)	$R_{N_I}^{\frac{1}{2}} : 1.02-1.27$	0.7/5.0
	F_0	0.999(14)	$R_{N_I}^{\frac{1}{4}} : 1.00-1.13$	0.4/5.0
	$\langle \bar{\psi}\psi \rangle$	1.00(3)	$R_{N_I}^{\frac{1}{2}} : 1.02-1.27$	0.2/5.0
	\hat{m}_{ud}	1.00(3)	$R_{N_I}^{\frac{1}{2}} : 1.02-1.27$	0.2/5.0
	m_π	1.000(14)	$R_{N_I}^{\frac{1}{4}} : 1.00-1.13$	0.4/5.0
	F_π	1.000(14)	$R_{N_I}^{\frac{1}{4}} : 1.00-1.13$	0.4/5.0
Interp.	Σ_{RMT}	0.999(12)	$R_{N_I}^{\frac{1}{2}} : 1.01-1.25$	0.8/5.0
	F_0	0.991(7)	$R_{N_I}^{\frac{1}{4}} : 1.00-1.12$	0.5/5.0
	$\langle \bar{\psi}\psi \rangle$	0.981(17)	$R_{N_I}^{\frac{1}{2}} : 1.01-1.25$	0.4/5.0
	\hat{m}_{ud}	0.981(17)	$R_{N_I}^{\frac{1}{2}} : 1.01-1.25$	0.4/5.0
	m_π	0.991(7)	$R_{N_I}^{\frac{1}{4}} : 1.00-1.12$	0.5/5.0
	F_π	0.991(7)	$R_{N_I}^{\frac{1}{4}} : 1.00-1.12$	0.5/5.0

of the observables to the vertical axis, and fit the linear function

$$R_{\text{obs}} = A_R^{\text{obs}} R_{N_I}^{\frac{1}{2}} \quad (59)$$

to the numerical results of case 1. Similarly, we fit the linear function

$$R_{\text{obs}} = A_R^{\text{obs}} R_{N_I}^{\frac{1}{4}} \quad (60)$$

to the numerical results of case 2. The prediction of the slopes is $A_R^{\text{Pre}} = 1$. We compare the fitting results of the slope values with the predictions, as shown in Table 21 and Fig. 16. Fig. 16 shows no influence of the finite lattice volume on the slope values, and the slope values are consistent with the prediction. Therefore, the observables decrease or increase in direct proportion to the square root or the one-fourth root of the number density of the instantons and anti-instantons.

5.6 Catalytic effect on the pion decay

We have shown that the pion mass becomes heavy, and the pion decay constant increases. These are caused by increasing the number density of the instantons and anti-instantons created by the additional monopoles and anti-monopoles. We have quantitatively demonstrated that the increases in the pion mass and pion decay constant are directly proportional to the one-fourth root of the number density of the instantons and anti-instantons. This relation is confirmed by comparing the ratios of the predictions with the ratios of the numerical results.

The instanton and monopole creations increase the mass and decay constant of the pion, and the increases affect the pion decay. Therefore, we estimate the effects of the instanton and monopole creations on the pion decay using the numerical results and predictions of the pion mass and pion decay constant as the input values.

This study focuses on the following decay of the charged pions π^\pm , that is, more than 99.99% [66] of the charged pions decay into muons and neutrinos.

$$\pi^+ \rightarrow \mu^+ + \nu_\mu, \quad \pi^- \rightarrow \mu^- + \bar{\nu}_\mu$$

The partial decay width of the charged pions is estimated as follows [25]:

$$\Gamma(\pi^- \rightarrow \mu^- + \bar{\nu}_\mu) = \frac{(G_F F_\pi \cos \theta_c)^2}{4\pi m_\pi^2} m_\mu^2 (m_\pi^2 - m_\mu^2)^2. \quad (61)$$

Table 22. Comparisons of the computed results of the decay width $\Gamma^{14^3 28}$, $\Gamma^{16^3 32}$, and Γ^{int} with the predictions Γ^{Pre1} and Γ^{Pre2} . The outcomes of $\Gamma^{14^3 28}$, $\Gamma^{16^3 32}$, and Γ^{int} calculated using the lattice $V = 14^3 \times 28$, $V = 16^3 \times 32$, and interpolated results, respectively. The predictions Γ^{Pre1} and Γ^{Pre2} are for the lattice volumes $V = 14^3 \times 28$ ($V_{\text{phys}} = 5.7845$ [fm⁴]) and $V = 16^3 \times 32$ ($V_{\text{phys}} = 9.8682$ [fm⁴]), respectively.

m_c	Γ^{Pre1} [sec ⁻¹] $\times 10^7$	$\Gamma^{14^3 28}$ [sec ⁻¹] $\times 10^7$	Γ^{Pre2} [sec ⁻¹] $\times 10^7$	$\Gamma^{16^3 32}$ [sec ⁻¹] $\times 10^7$	Γ^{int} [sec ⁻¹] $\times 10^7$
N. C.	3.774(7)	3.8(3)	3.774(7)	3.8(3)	3.77(14)
0	3.774(7)	3.6(3)	3.774(7)	3.8(3)	3.84(17)
1	5.099(9)	4.6(4)	4.544(8)	4.4(4)	4.5(2)
2	6.471(12)	6.6(5)	5.333(10)	6.3(5)	6.1(3)
3	7.873(14)	7.9(6)	6.136(11)	7.2(6)	6.6(3)
4	9.294(17)	9.3(7)	6.951(13)	8.6(6)	7.4(3)
5	10.73(2)	9.5(7)	7.775(14)	8.5(6)	7.8(3)

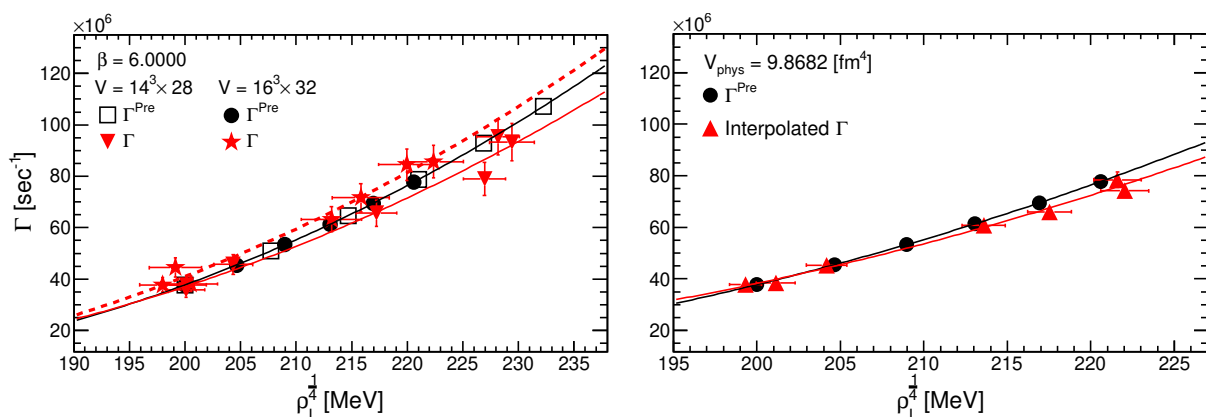


Fig. 17. Comparing the partial decay width of the charged pion Γ of the configurations $\beta = 6.0000$, $V = 14^3 \times 28$ and $V = 16^3 \times 32$ (left) and the interpolated results (right) with the predictions Γ^{Pre} . In the left figure, the black full line, the red full line, and the red dashed line indicate the fitting results of the predictions, the numerical results of $V = 14^3 \times 28$, and $V = 16^3 \times 32$, respectively. In the right figure, the full black line and red line indicate the fitting results of the prediction and the interpolated results, respectively.

Table 23. The fitting results of the partial decay width Γ by the curve $\Gamma = p_1 x^3 - p_2 x + \frac{p_3}{x}$, ($x = \rho_I^{-1/4}$ [MeV]). Pre1 stands for the fitting results of the prediction Γ^{Pre1} .

Conf	p_1 [sec ⁻¹ ·MeV ⁻³]	p_2 [sec ⁻¹ ·MeV ⁻¹] $\times 10^6$	p_3 [sec ⁻¹ ·MeV] $\times 10^{10}$	FR: $\rho_I^{-1/4}$ [MeV] $\times 10^2$	$\frac{\chi^2}{\text{dof}}$
Pre1	25.89(4)	1.187(3)	1.360(8)	1.99-2.33	0.0/3.0
$14^3 \times 28$	22.5(1.8)	1.00(14)	1.1(4)	1.99-2.30	1.9/4.0
$16^3 \times 32$	26(2)	1.11(17)	1.1(5)	1.97-2.23	1.7/4.0
Interp.	24.2(1.1)	1.16(8)	1.5(2)	1.97-2.23	1.5/4.0

Here, we use the experimental outcomes as follows: The Dirac constant is $\hbar = 6.582119514(40) \times 10^{-16}$ [eV·s], and the Fermi constant is $G_F = 1.1663787(6) \times 10^{-5}$ [GeV⁻²] [66]. We do not consider the errors of the experimental outcomes because they are negligibly more minuscule than the errors of the numerical results. When we matched the numerical results of the pion mass and pion decay constant with the experimental outcomes in subsection 5.1, we used the experimental outcomes of π^- ; therefore, suppose that the experimental outcomes of the decay of the charged pion π^- are the same as π^+ .

To check the consistency of formula (61) with the experimental result of the partial decay width, first, we substitute the interpolated results of the pion mass and pion decay constant of the normal configurations in Tables 18 and 17 and estimate the partial decay width. The result is $\Gamma^{\text{int}} = 3.77(14) \times 10^7$ [sec⁻¹].

The experimental result of the lifetime of the charged pion [66] is

$$\tau^{\text{Exp}} = 2.6033(5) \times 10^{-8} \text{ [sec]}. \quad (62)$$

The decay width of the charged pion, which is estimated using the experimental outcome of the lifetime of the charged

Table 24. Comparisons of the lifetimes $\tau^{14^3 \times 28}$, $\tau^{16^3 \times 32}$, and τ^{int} with the predictions τ^{Pre1} and τ^{Pre2} . The outcomes of $\tau^{14^3 \times 28}$, $\tau^{16^3 \times 32}$, and τ^{int} calculated using the lattice $V = 14^3 \times 28$, $V = 16^3 \times 32$, and the interpolated results, respectively. The predictions τ^{Pre1} and τ^{Pre2} are for the lattice volumes $V = 14^3 \times 28$ ($V_{\text{phys}} = 5.7845$ [fm⁴]) and $V = 16^3 \times 32$ ($V_{\text{phys}} = 9.8682$ [fm⁴]), respectively.

m_c	τ^{Pre1} [sec] $\times 10^{-8}$	$\tau^{14^3 \times 28}$ [sec] $\times 10^{-8}$	τ^{Pre2} [sec] $\times 10^{-8}$	$\tau^{16^3 \times 32}$ [sec] $\times 10^{-8}$	τ^{int} [sec] $\times 10^{-8}$
N. C.	2.649(5)	2.6(2)	2.649(5)	2.65(19)	2.65(10)
0	2.649(5)	2.8(2)	2.649(5)	2.6(2)	2.60(11)
1	1.961(4)	2.19(19)	2.201(4)	2.25(19)	2.21(10)
2	1.545(3)	1.52(12)	1.875(3)	1.58(12)	1.65(7)
3	1.270(2)	1.27(10)	1.630(3)	1.40(11)	1.51(7)
4	1.076(2)	1.07(8)	1.439(3)	1.17(9)	1.35(5)
5	0.9321(17)	1.05(7)	1.286(2)	1.18(9)	1.28(5)

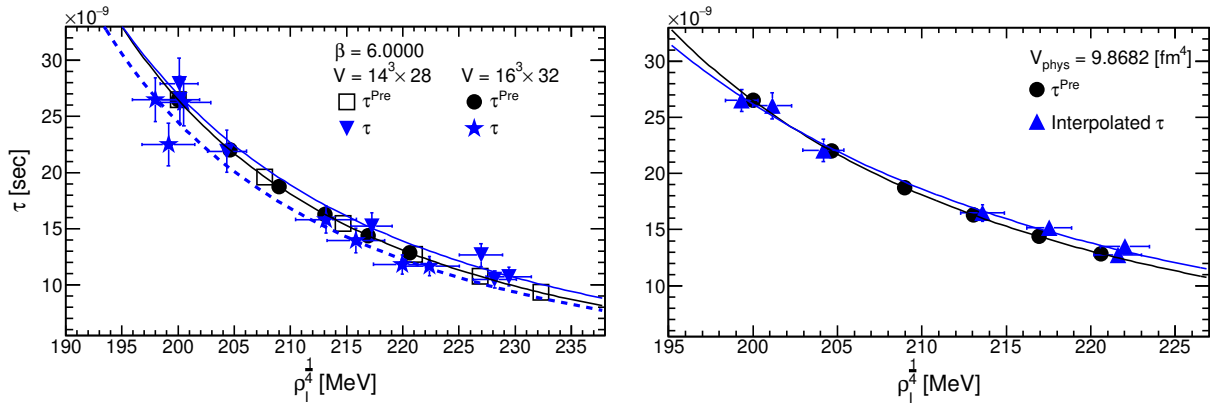


Fig. 18. Comparing the lifetime of the charged pion τ of the configurations of $\beta = 6.0000$, $V = 14^3 \times 28$ and $V = 16^3 \times 32$ (left) and the continuum limit (right) with the prediction τ^{Pre} . In the left figure, the black full line, the blue full line, and the blue dashed line indicate the fitting results of the predictions, the numerical results of $V = 14^3 \times 28$, and $V = 16^3 \times 32$, respectively. In the right figure, the full black line and blue line indicate the fitting results of the prediction and the interpolated results, respectively.

Table 25. The fitting results of the lifetime τ by the curve $\tau = (p_1 x^3 - p_2 x + \frac{p_3}{x})^{-1}$, ($x = \rho_I^{\frac{1}{4}}$ [MeV]). Pre1 stands for the fitting results of the prediction τ^{Pre1} .

Conf	p_1 [sec ⁻¹ ·MeV ⁻³]	p_2 [sec ⁻¹ ·MeV ⁻¹] $\times 10^6$	p_3 [sec ⁻¹ ·MeV] $\times 10^{10}$	FR: $\rho_I^{\frac{1}{4}}$ [MeV] $\times 10^2$	$\frac{\chi^2}{\text{dof}}$
Pre1	25.89(4)	1.187(3)	1.360(8)	1.99-2.33	0.0/3.0
$14^3 \times 28$	22.4(1.4)	0.98(1.4)	1.1(5)	1.99-2.30	1.8/4.0
$16^3 \times 32$	25(2)	1.04(17)	1.0(5)	1.97-2.23	1.7/4.0
Interp.	23.1(1.1)	1.05(8)	1.3(2)	1.97-2.23	1.5/4.0

pion is $\Gamma^{\text{Exp}} = 3.8413(7) \times 10^7$ [sec⁻¹]. The estimation coming from the numerical result is 1.9% larger than the experimental outcome; however, this result verifies that we can adequately estimate the partial decay width of the charged pion using formula (61) and the numerical results.

Next, we estimate the partial decay width by substituting the following numerical results and predictions into formula (61): (i) The numerical results of the lattice volumes $V = 14^3 \times 28$ and $V = 16^3 \times 32$ of $\beta = 6.0000$ and the predictions are in Table 51 in H. (ii) The interpolated results of the pion mass and pion decay constant are in Tables 17 and 18. The calculated results of the partial

decay width compared with the predictions are listed in Table 22.

We have confirmed that the increases in the pion mass and pion decay constant are directly proportional to the one-fourth root of the number density of the instantons and anti-instantons. Therefore, we make the following curve to fit the calculated results of the decay width:

$$\Gamma = p_1 x^3 - p_2 x + \frac{p_3}{x}, \quad x = \rho_I^{\frac{1}{4}} \text{ [MeV]}. \quad (63)$$

We fit this curve to the calculated results, as shown in Fig. 17, and list the fitting results in Table 23. The fit-

ting results of the parameters p_1 , p_2 , and p_3 are reasonably consistent with the fitting results of the prediction, as indicated in Table 23; thus, the finite lattice volume does not affect the results of the partial decay width of the charged pion. Figure 17 shows that the partial decay width becomes wider with increasing one-fourth root of number density of the instantons and anti-instantons, and the increases are consistent with the predictions.

The partial decay width of the charged pion into the muon and neutrino is almost 100%; therefore, finally, we estimate the lifetime τ of the charged pion from its inverse of the partial decay width and quantitatively demonstrate the catalytic effect caused by the monopole and instanton creations on the pion decay.

Similar to the decay width, we estimate the lifetime using the numerical results of the lattice volumes $V = 14^3 \times 28$ and $V = 16^3 \times 32$, interpolated results, and predictions. We compare the numerical results with the predictions in Table 24 and plot them in Fig. 18. To quantitatively evaluate the catalytic effect on the pion decay, we fit the inverse of the fitting curve (63)

$$\tau = \left(p_1 x^3 - p_2 x + \frac{p_3}{x} \right)^{-1}, \quad x = \rho_I^{\frac{1}{4}} [\text{MeV}] \quad (64)$$

to the computed results, as shown in Fig. 18. The fitting results of the lifetime are given in Table 25. The fitting results of the parameters p_1 , p_2 , and p_3 indicate no influence of the finite lattice volume, and they are reasonably consistent with the fitting results of the predictions and the partial decay width Γ .

These results demonstrate that the lifetime of the charged pion becomes shorter than the experimental result (62) by increasing the one-fourth root of the number density of the instantons and anti-instantons without the finite lattice volume influence. This is the catalytic effect caused by the monopole and instanton creations on the pion decay.

6 Summary and conclusions

We have performed the simulations to find the clues to observe the effects of the magnetic monopoles and instantons in the QCD by experiments. The primary purposes of this study were to inspect the influences of the finite lattice volume and discretization on the observables and quantitative relations, which we have obtained in our previous research, and to obtain the interpolated results at the continuum limit.

For these purposes, we prepared the standard configurations and the configurations of the following lattice volumes and parameter values in which the monopoles and anti-monopoles were added: (i) To inspect the influence of the finite lattice volume, $V = 14^3 \times 28$ and $V = 16^3 \times 32$ of the parameter value $\beta = 6.0000$. (ii) To inspect the influence of the discretization, $V = 12^3 \times 24$ of $\beta = 5.8124$, $V = 14^3 \times 28$ of $\beta = 5.9256$, and $V = 20^3 \times 40$ of $\beta = 6.1366$. We added the monopoles and anti-monopoles varying the magnetic charges from 0 to 5 to these configurations. We used the outcomes of the lattice of $V =$

$18^3 \times 32$ of $\beta = 6.0522$, which we have already been reported, to interpolate the results to the continuum limit by fitting the curves. We calculated the low-lying eigenvalues and eigenvectors of the overlap Dirac operator using these configurations, evaluated the observables using the low-lying eigenvalues and eigenvectors, and demonstrated the quantitative relations by comparing the observables with the predictions.

First, we confirmed that the additional monopoles and anti-monopoles do not affect the numerical results of the lattice spacing by computing the static potential. Then, we found minor effects of the finite lattice volume on the number density of the monopoles and anti-monopoles computed using the standard configurations.

We analyzed the effects of the additional monopoles and anti-monopoles. We found that the influences of the finite lattice volume appear when we add the monopoles and anti-monopoles with the magnetic charges m_c higher than 3 to the small lattice volume $V = 12^3 \times 24$ of the coarse lattice spacing $\beta = 5.8457$. Therefore, we calculated the numerical results using the lattices $V = 20^3 \times 40$ of $\beta = 6.1366$ of the magnetic charges 4 and 5 and interpolated the numerical results to the continuum limit instead of using the numerical results of the lattices $V = 12^3 \times 24$ of $\beta = 5.8457$ of the magnetic charges 4 and 5.

Next, similar to the calculations of the number density of the monopoles and anti-monopoles, we calculated the number density of the instantons and anti-instantons using the standard configurations. We confirmed that the outcomes of the number density of the instantons and anti-instantons do not vary even if we change the physical volumes fixing the values of the lattice spacing parameter, or we change the lattice volumes and values of the lattice spacing parameter fixing the physical volumes. Furthermore, these outcomes are reasonably consistent with the prediction of the phenomenological model concerning the instantons.

Our previous study showed that one pair of the additional monopole and anti-monopole of the magnetic charge $m_c = 1$ makes one instanton or anti-instanton. To inspect the influences of the finite lattice volume and the discretization on this quantitative relationship, we plotted the number of magnetic charges m_c of the additional monopole and anti-monopole to the horizontal axis and the number of instantons and anti-instantons N_I to the vertical axis, and we fitted the linear function to the numerical results. We confirmed that the fitting results were reasonably consistent with our previous outcomes and predictions, without the influence of the finite lattice volume or discretization. Therefore, we obtained the number density of the instantons and anti-instantons at the continuum limit by the interpolation.

This study analytically estimated the number of instantons and anti-instantons from the topological charges; therefore, we inspected the influence of the additional monopoles and anti-instantons, finite lattice volume, and discretization on the distributions of the topological charge by comparing them with the predicted distribution functions. We confirmed that the additional monopoles and

anti-monopoles add the topological charges without changing the vacuum structures; in addition, the finite lattice volume and discretization did not affect the distributions of the topological charges.

Next, to inspect the influences of the additional monopoles and anti-monopoles, finite lattice volume, and discretization on the low-lying eigenvalues of the overlap Dirac operator, we calculated the distributions of the nearest-neighbor spacing of the eigenvalues, the spectral rigidity, and ratios of the low-lying eigenvalues. We demonstrated that the numerical results are consistent with the predictions of the RMT. This result indicated that the additional monopoles and anti-monopoles, finite lattice volume, and discretization did not affect the fluctuations of the eigenvalues from the short to long-range or the ratios of the low-lying eigenvalues.

Our previous research has already demonstrated the effects caused by the instanton and anti-instanton creations on the renormalized chiral condensate and renormalized quark masses in the $\overline{\text{MS}}$ -scheme at 2 [GeV], light meson masses, and decay constants. In addition, the previous research revealed the quantitative relations among the number densities of the instantons and anti-instantons and the observables; however, this showed only the outcomes obtained using the lattice $V = 18^3 \times 32$ of $\beta = 6.0522$. Therefore, we inspected the influences of the finite lattice volume and discretization on these outcomes using the lattices (i) and (ii) mentioned above.

We first computed the correlation functions of the scalar density and the pseudoscalar density using the eigenvalues and eigenvectors. We then confirmed that the additional monopoles and anti-monopoles, finite lattice volume, and discretization do not affect the PCAC relation. We demonstrated that the interpolated results of the renormalization constant for the scalar density at the continuum limit are reasonably consistent.

It is well known that the instantons and anti-instantons are closely related to chiral symmetry breaking; therefore, we evaluated the renormalized chiral condensate in the $\overline{\text{MS}}$ -scheme at 2 [GeV] using the outcomes of the scale parameter of the eigenvalue distribution in chRMT and the renormalization constant for the scalar density. We demonstrated that the renormalized chiral condensate decreases in direct proportion to the square root of the number density of the instantons and anti-instantons. This result is consistent with the outcome in our previous study. However, the finite lattice volume influenced the renormalized chiral condensate. Furthermore, the interpolated results of the renormalized chiral condensate were not consistent with the prediction.

Therefore, we obtained the normalization factor by matching the numerical results with the experimental results and improved the computation method by using the normalization factor without suffering from uncertainties coming from the determinations of the lattice scales. By this computation, we could calculate the observables without any discretization influences. In addition, higher precision calculations than our previous study revealed the

quantitative relations among the observables and the number density of the instantons and anti-instantons.

First, to show that we could adequately calculate the observables using the normalization factor, we estimated the decay constant of the pseudoscalar at the chiral limit. We showed that the decay constant of the pseudoscalar meson at the chiral limit linearly increases with the one-fourth root of the number density of the instantons and anti-instantons. To evaluate the rise, we fitted the linear function and demonstrated that the fitting results of the slope are steeper than the predicted slope value; however, the decay constant of the pseudoscalar meson at the chiral limit increased in direct proportion to the one-fourth root of the number density of the instantons and anti-instantons, without any influences of the finite lattice volume or the discretization.

We have mentioned that the renormalized chiral condensate, which is estimated from the scale parameter of the eigenvalue distribution, shows the influence of the sizeable finite lattice volume, and the fitting result of the interpolated results is not consistent with the prediction. Therefore, we recalculated the renormalized chiral condensate in the $\overline{\text{MS}}$ -scheme at 2 [GeV], which is derived from the GMOR relation, using the normalization factor, and showed that the discretization does not influence the outcomes.

As a result, we demonstrated that the renormalized chiral condensate in the $\overline{\text{MS}}$ -scheme at 2 [GeV] decreases in direct proportion to the square root of the number density of the instantons and anti-instantons. Furthermore, the slope values obtained by the numerical computations were consistent with the predictions without the influences of the finite lattice volume. The phenomenological model cannot predict the average size of the instanton or anti-instanton; therefore, we estimated the inverse of the average size of the instanton or anti-instanton using the slope value of the interpolated results and confirmed the consistency with the phenomenological model.

These results indicated that the instantons and anti-instantons created by the additional monopoles and anti-monopoles induce chiral symmetry breaking, as explained in the phenomenological model. Therefore, we supposed that chiral symmetry breaking is induced by the instantons and anti-instantons created and affects the quark mass generation. We first confirmed that the discretization influence is negligible. We then estimated the increases in the renormalized average mass of the up and down quarks in the $\overline{\text{MS}}$ -scheme at 2 [GeV] to ensure this assumption. We revealed that the renormalized average mass of the up and down quarks in the $\overline{\text{MS}}$ -scheme at 2 [GeV] increases in direct proportion to the square root of the instantons and anti-instantons. We compared the fitting results of the slope value with the predictions to quantitatively evaluate the increases. The fitting results showed that the finite lattice volume does not affect the slope values; however, the fitting results of the slope were slightly steeper than the prediction.

The pion mass was composed of the up and down quarks, and we showed that the average mass of the up

and down quarks increases with the number density of the instantons and anti-instantons. Therefore, we estimated the impacts on the pion mass caused by increasing the average mass of the light quarks. We indicated that the slope of the PCAC relation is not affected by increases in the additional monopoles and anti-monopoles. Moreover, we demonstrated that the logarithmic divergence near the chiral limit does not appear and the linear relationship between the decay constant of the pseudoscalar and the square mass of the pseudoscalar holds.

Therefore, we supposed that the pion mass and pion decay constant increased in direct proportion to the one-fourth root of the number density of the instantons and anti-instantons. We evaluated these increases by comparing the fitting results of the slope values with the predictions after confirming that the discretization does not obviously affect the outcomes. We revealed that the numerical results are consistent with these assumptions without finite lattice volume influence.

However, the decrease and increases in the observables included uncertainties coming from the renormalization constant, normalization factor, and lattice scales; therefore, to remove these uncertainties, we calculated the ratios among the observables computed using the standard configurations and the observables computed using the configurations with the additional monopoles and anti-monopoles. We showed that the ratios of the numerical results are consistent with the prediction. Moreover, we did not observe any influences of the finite lattice volume on the computed ratios.

We quantitatively demonstrated that the pion mass and pion decay constant increase with the number density of the instantons and anti-instantons. Furthermore, these increases and the ratios among the observables were consistent with the predictions; therefore, we predicted that the pion decay is affected by the increases in the pion mass and pion decay constant.

Therefore, we focused on the charged pion decay and estimated the effects of the instanton and anti-instanton created on the partial decay width of the charged pion. We found that the partial decay width of the charged pion becomes wider than the experimental outcome when the one-fourth root of the number density of the instantons and anti-instantons increased. We quantitatively demonstrated that the increases in the partial decay width are consistent with the prediction by fitting the curve. Furthermore, we did not observe any influence of the finite lattice volume on these outcomes.

Finally, we estimated the lifetime of the charged pion from the inverse of the decay width because almost 100% of the charged pions decay into muons and neutrinos. We demonstrated the catalytic effect in which the number density of the instantons and anti-instantons increased with the number density of the additional monopoles and anti-monopoles, resulting in the lifetime of the charged pion becoming shorter than the experimental result. To quantitatively demonstrate the catalytic effect, we fitted the curve to the numerical results. Finally, we demonstrated that the fitting results of the numerical results are

consistent with the fitting results of the prediction without the influence of the finite lattice volume.

Acknowledgements

The author has started this research project with A. Di Giacomo and F. Pucci and appreciates the helpful discussion and advice. The author would like to thank M. D'Elia for the helpful discussions. Furthermore, the author received financial support for visiting the University of Pisa from the Istituto Nazionale di Fisica Nucleare at the University of Pisa and the Joint Institute for Nuclear Research. This research project was performed using the SX-series, computer clusters, and XC40 at the Research Center for Nuclear Physics and the Cybermedia Center at Osaka University and the Yukawa Institute for Theoretical Physics at Kyoto University. In addition, we have used the storage elements from the Japan Lattice Data Grid at the Research Center for Nuclear Physics at Osaka University. We sincerely appreciate the computer resources that they provided to us and their technical support.

A Lattice spacing

We do not diagonalize the SU(3) non-Abelian link variables under gauge conditions, and perform the smearing [69] to the spatial components of the SU(3) non-Abelian link variables to remove the statistical errors. The number of smearing procedures is n , and its weight parameter is α . We then calculate the static potential $V(R)$ from the Wilson loops using the smeared link variables. Suppose that the static potential $V(R)$ can be approximated by the following formula:

$$V(R) = V_0 + \sigma R - \frac{\alpha}{R}. \quad (65)$$

We fit this curve to the calculated results of $V(R)$ and obtain the fitting parameters σ and α . We improve the distance of the spatial direction of the Wilson loop R by the Green function [40,70] and indicate it as R_I . The lattice spacing $a^{(1)}$ is estimated from the Sommer scale $r_0 = 0.5$ [fm] and fitting results of σ and α . The lattice spacing $a^{(2)}$ is estimated using the formula $\sigma = 440$ [MeV] and fitting results of σ . The results of lattice spacing $a^{(1)}$ and $a^{(2)}$ are shown in Table 26.

Table 26. The computed results of the lattice spacing $a^{(1)}$ and $a^{(2)}$. The smearing parameters are (n, α) , the length of the temporal direction of the Wilson loops is T/a , and the fitting range is FR.

β	V	m_c	$a^{(1)}$ [fm]	$a^{(2)}$ [fm]	(n, α)	T/a	FR : R_I/a	$\frac{\chi^2}{\text{dof}}$	N_{conf}		
5.8457	$12^3 \times 24$	N. C.	0.1235(4)	0.1300(3)	(10, 0.4)	3	0.9-6.0	3.5/3.0	1100		
		0	0.1227(8)	0.1290(8)	(15, 0.4)	4	0.9-6.0	3.2/3.0	1040		
		1	0.125(4)	0.130(2)	(15, 0.4)	4	1.8-6.0	2.4/2.0	1040		
		2	0.127(2)	0.1324(10)	(10, 0.4)	3	1.8-5.0	0.5/2.0	1040		
		3	0.126(6)	0.1301(26)	(15, 0.3)	4	1.8-6.0	2.4/2.0	1040		
		4	0.1257(11)	0.1310(10)	(10, 0.5)	4	0.9-6.0	4.0/3.0	1040		
		5	0.1261(5)	0.1315(5)	(10, 0.4)	3	0.9-6.0	4.1/3.0	1030		
5.9256	$14^3 \times 28$	N. C.	0.1069(18)	0.1130(10)	(15, 0.4)	4	1.8-6.0	1.7/2.0	1100		
		0	0.1066(2)	0.1126(2)	(15, 0.4)	3	0.9-6.0	4.0/4.0	1000		
		1	0.1081(10)	0.1140(9)	(20, 0.3)	5	0.9-6.0	2.1/3.0	1000		
		2	0.107(2)	0.1121(9)	(20, 0.3)	4	1.8-7.0	2.4/3.0	1000		
		3	0.107(6)	0.110(2)	(15, 0.5)	5	1.8-7.0	2.1/3.0	1000		
		4	0.108(3)	0.1126(13)	(15, 0.5)	4	1.8-6.0	1.4/2.0	1000		
		5	0.108(3)	0.1127(13)	(15, 0.3)	4	1.8-6.0	0.6/2.0	1000		
6.0000	$14^3 \times 28$	N. C.	$9.293(13) \times 10^{-2}$	$9.775(6) \times 10^{-2}$	(20, 0.4)	4	1.8-7.0	2.1/3.0	1200		
		0	$9.408(7) \times 10^{-2}$	$9.949(6) \times 10^{-2}$	(25, 0.4)	5	0.9-6.0	2.5/3.0	1200		
		1	$9.566(7) \times 10^{-2}$	0.10118(6)	(25, 0.4)	5	0.9-6.0	4.1/3.0	1200		
		2	$9.57(3) \times 10^{-2}$	0.10021(14)	(20, 0.4)	4	1.8-7.0	2.5/3.0	1200		
		3	$9.61(4) \times 10^{-2}$	0.10000(19)	(25, 0.4)	5	1.8-6.0	1.9/2.0	1200		
		4	$9.637(17) \times 10^{-2}$	0.10067(7)	(20, 0.4)	4	1.8-7.0	2.9/3.0	1200		
		5	$9.535(19) \times 10^{-2}$	$9.892(7) \times 10^{-2}$	(20, 0.4)	4	1.8-7.0	2.1/3.0	1200		
	$16^3 \times 32$	N. C.	$9.38(5) \times 10^{-2}$	$9.93(4) \times 10^{-2}$	(25, 0.5)	5	0.9-7.0	3.8/4.0	1140		
		0	$9.28(13) \times 10^{-2}$	$9.74(6) \times 10^{-2}$	(20, 0.5)	4	1.8-6.0	0.9/2.0	1100		
		1	$9.46(5) \times 10^{-2}$	0.1000(4)	(25, 0.4)	5	0.9-7.0	3.4/4.0	1100		
		2	$9.52(10) \times 10^{-2}$	$9.99(4) \times 10^{-2}$	(20, 0.5)	4	1.8-8.0	4.0/4.0	1100		
		3	$9.6(2) \times 10^{-2}$	0.1010(10)	(25, 0.3)	5	1.8-8.0	3.3/4.0	1100		
		4	$9.5(3) \times 10^{-2}$	$9.83(15) \times 10^{-2}$	(25, 0.4)	5	1.8-6.0	1.6/2.0	1100		
		5	$9.4(3) \times 10^{-2}$	$9.79(16) \times 10^{-2}$	(25, 0.5)	5	1.8-6.0	1.4/2.0	1100		
		6.0522	$20^3 \times 40$	N. C.	$7.51(16) \times 10^{-2}$	$7.91(7) \times 10^{-2}$	(35, 0.4)	6	1.8-9.0	3.6/5.0	1000
				4	$7.6(2) \times 10^{-2}$	$8.01(12) \times 10^{-2}$	(30, 0.4)	6	1.8-6.0	0.8/2.0	1060
				5	$7.70(10) \times 10^{-2}$	$8.09(4) \times 10^{-2}$	(30, 0.5)	5	1.8-8.0	1.5/4.0	1070

B The monopole density and instanton density of the normal configuration

Table 27. The number density of the monopoles and anti-monopoles ρ_m^{long} of the standard configurations.

β	a/r_0	V	$V_{\text{phys}}^{\frac{3}{4}}$ [fm ³]	ρ_m^{long} [GeV ³]	N_{conf}
5.7887	0.2795	12 ⁴	4.7137	0.1054(15)	80
5.8124	0.2659	10 ⁴	2.3489	0.101(2)	80
		14 ⁴	6.4453	0.1084(13)	80
		16 ⁴	9.6210	0.1147(9)	80
5.8457	0.2484	12 ⁴	3.3106	0.1002(19)	80
		14 ⁴	5.2571	0.1066(17)	80
		12 ³ 24	5.5677	0.1027(15)	100
		16 ⁴	7.8473	0.1117(13)	80
		18 ⁴	11.173	0.1175(7)	80
5.8640	0.2395	14 ⁴	4.7137	0.1055(17)	80
5.9044	0.2216	12 ⁴	2.3489	0.099(3)	80
		16 ⁴	5.5677	0.1116(16)	80
5.9256	0.2129	14 ⁴	3.3106	0.107(2)	80
		16 ⁴	4.9417	0.1087(18)	80
		14 ³ 28	5.5677	0.1028(15)	100
		18 ⁴	7.0362	0.1044(16)	80
5.9341	0.2096	16 ⁴	4.7137	0.107(2)	80
5.9890	0.1899	14 ⁴	2.3489	0.103(2)	80
6.0000	0.1863	14 ⁴	2.2178	0.111(2)	80
		16 ⁴	3.3106	0.106(2)	80
		14 ³ 28	3.7299	0.1015(17)	100
		18 ⁴	4.7137	0.1037(19)	80
		16 ³ 32	5.5677	0.1068(17)	100
		20 ⁴	6.4660	0.1103(17)	80
		18 ³ 28	6.5656	0.111(2)	40
		18 ³ 32	7.2572	0.1093(15)	100
		24 ⁴	11.173	0.1169(14)	80
24 ³ 48	18.791	0.1237(12)	80		
6.0522	0.1705	18 ³ 32	5.5677	0.1077(15)	100
6.0625	0.1677	20 ⁴	4.7137	0.114(2)	55
6.0680	0.1662	16 ⁴	2.3489	0.111(2)	80
6.0701	0.1656	18 ⁴	3.3106	0.110(2)	80
6.1366	0.1490	20 ³ 40	5.5677	0.1128(19)	100
6.1424	0.1477	18 ⁴	2.3489	0.114(3)	55
6.1790	0.1397	24 ⁴	4.7137	0.121(3)	60

Table 28. The number density of the instantons and anti-instantons ρ_I of the standard configurations.

β	a/r_0	V	V_{phys} [fm ⁴]	$\rho_I \times 10^{-3}$ [GeV ⁴]	N_{conf}
5.7887	0.2795	12 ⁴	7.9034	1.60(7)	1000
5.8124	0.2659	10 ⁴	3.1224	1.66(7)	1204
		14 ⁴	11.995	1.56(14)	239
		16 ⁴	20.463	1.52(14)	247
5.8457	0.2484	12 ⁴	4.9341	1.67(13)	319
		12 ³ 24	9.8682	1.67(8)	900
		16 ⁴	15.594	1.67(14)	322
5.8640	0.2395	14 ⁴	7.9034	1.76(8)	1020
5.9044	0.2216	12 ⁴	3.1224	1.65(7)	1237
		16 ⁴	9.8682	1.61(7)	1022
5.9256	0.2129	14 ⁴	3.3106	1.74(12)	400
		14 ³ 28	9.8682	1.67(8)	850
		18 ⁴	13.480	1.43(11)	360
5.9341	0.2096	16 ⁴	7.9034	1.62(7)	1020
5.9890	0.1899	14 ⁴	3.1224	1.60(6)	1219
6.0000	0.1863	14 ⁴	2.8923	1.67(5)	2144
		16 ⁴	4.9341	1.68(7)	1045
		14 ³ 28	5.7845	1.60(6)	1720
		18 ⁴	7.9034	1.62(7)	1018
		16 ³ 32	9.8682	1.54(6)	1040
6.0522	0.1705	18 ³ 32	9.8682	1.48(7)	800
6.0680	0.1662	16 ⁴	3.1224	1.47(7)	1026
6.1366	0.1490	20 ³ 40	9.8682	1.49(10)	440
6.0701	0.1656	18 ⁴	3.3106	1.45(10)	303
6.1424	0.1477	18 ⁴	3.1224	1.44(12)	305

B.1 The number density of the monopoles and anti-monopoles ρ_m^{long} of the configurations of additional monopoles and anti-monopoles

Table 29. The calculated results of the number density of the additional monopole and anti-monopoles ρ_m^{long} .

β	V	m_c	ρ_m^{long} [GeV ³]	N_{conf}
5.8457	$12^3 \times 24$	N. C.	0.1027(15)	100
		0	0.1044(14)	100
		1	0.1185(13)	100
		2	0.1643(10)	100
		3	0.1973(10)	100
		4	0.2276(10)	100
		5	0.2512(9)	100
5.9256	$14^3 \times 28$	N. C.	0.1028(15)	100
		0	0.1012(17)	100
		1	0.1108(18)	100
		2	0.1601(13)	100
		3	0.1983(12)	100
		4	0.2397(11)	100
		5	0.2742(10)	100
6.0000	$14^3 \times 28$	N. C.	0.1015(17)	100
		0	0.0982(16)	100
		1	0.106(2)	100
		2	0.168(2)	100
		3	0.2232(16)	100
		4	0.2846(15)	100
		5	0.3385(13)	100
6.0000	$16^3 \times 32$	N. C.	0.1068(17)	100
		0	0.1064(16)	100
		1	0.1080(17)	100
		2	0.1583(15)	100
		3	0.1988(15)	100
		4	0.2468(13)	100
		5	0.2871(11)	100
6.0522	$18^3 \times 32$	N. C.	0.1077(15)	100
		0	0.1115(18)	100
		1	0.1126(19)	100
		2	0.1573(17)	100
		3	0.2001(14)	100
		4	0.2536(11)	100
		5	0.3010(11)	100
6.1366	$20^3 \times 40$	N. C.	0.1128(19)	100
		4	0.2412(17)	60
		5	0.2926(17)	60

C The number of observed zero modes N_Z , number of instantons N_I , and number density of instantons and anti-instantons $\frac{N_I}{V}$

Table 30. The number of observed zero modes $N_Z = |Q|$, number of instantons N_I , and number density of instantons and anti-instantons $\rho_I, \rho_I^{\frac{1}{2}}, \rho_I^{\frac{1}{4}}$, and their predictions. The predictions are indicated as Pre1 for the physical volume $V_{\text{phys}} = 5.7845$ [fm⁴] ($\beta = 6.0000, V = 14^3 \times 28$) and Pre2 for the physical volume $V_{\text{phys}} = 9.8582$ [fm⁴] (apart from $\beta = 6.0000, V = 16^3 \times 32$) in the column of β . These are calculated using the equations (8) and (9).

β	V	m_c	N_Z	N_I	ρ_I [GeV ⁴] $\times 10^{-3}$	$\rho_I^{\frac{1}{2}}$ [GeV ²] $\times 10^{-2}$	$\rho_I^{\frac{1}{4}}$ [MeV] $\times 10^2$	N_{conf}
Pre1	-	Normal conf	1.9713	6.1044	1.6000	4.0000	2.0000	-
		1	2.1306	7.1044	1.8621	4.3152	2.0773	-
		2	2.2777	8.1044	2.1242	4.6089	2.1468	-
		3	2.4153	9.1044	2.3863	4.8850	2.2102	-
		4	2.5450	10.104	2.6484	5.1463	2.2685	-
		5	2.6682	11.104	2.9105	5.3949	2.3227	-
Pre2	-	Normal conf	2.5748	10.414	1.6000	4.0000	2.0000	-
		1	2.6975	11.414	1.7536	4.1877	2.0464	-
		2	2.8144	12.414	1.9073	4.3672	2.0898	-
		3	2.9265	13.414	2.0609	4.5397	2.1307	-
		4	3.0343	14.414	2.2146	4.7059	2.1693	-
		5	3.1383	15.414	2.3682	4.8664	2.2060	-
5.8457	$12^3 \times 24$	Normal conf	2.61(7)	10.9(5)	1.67(8)	4.09(10)	2.02(2)	900
		0	2.51(6)	10.4(5)	1.60(7)	4.00(9)	2.00(2)	1100
		1	2.75(7)	12.0(6)	1.84(9)	4.29(10)	2.07(2)	950
		2	2.84(7)	12.9(6)	1.99(9)	4.46(10)	2.11(2)	1050
		3	2.96(7)	14.1(7)	2.16(10)	4.65(11)	2.16(3)	950
		4	3.05(8)	14.9(7)	2.29(11)	4.78(11)	2.19(3)	950
5.9256	$14^3 \times 28$	Normal conf	2.64(7)	10.9(5)	1.67(8)	4.09(9)	2.02(2)	850
		0	2.62(7)	11.0(5)	1.68(8)	4.10(10)	2.03(2)	868
		1	2.73(7)	11.9(6)	1.84(9)	4.28(10)	2.07(2)	950
		2	3.00(8)	14.4(7)	2.21(11)	4.70(11)	2.17(3)	852
		3	3.14(8)	15.2(7)	2.34(11)	4.83(12)	2.20(3)	802
		4	3.17(8)	15.7(8)	2.42(12)	4.92(12)	2.22(3)	800
6.0000	$14^3 \times 28$	Normal conf	1.93(4)	6.1(2)	1.60(6)	4.01(7)	2.002(1.7)	1720
		0	1.93(4)	6.1(2)	1.60(5)	4.00(7)	2.001(1.7)	1800
		1	2.05(4)	6.7(2)	1.74(6)	4.18(7)	2.043(1.7)	1710
		2	2.33(4)	8.5(3)	2.23(7)	4.72(8)	2.172(1.8)	1710
		3	2.52(5)	10.1(3)	2.65(9)	5.15(9)	2.270(1.9)	1720
		4	2.53(5)	10.6(4)	2.77(10)	5.26(9)	2.29(2)	1732
	$16^3 \times 32$	Normal conf	2.54(6)	10.0(4)	1.54(6)	3.92(8)	1.98(2)	1040
		0	2.55(7)	10.5(5)	1.62(8)	4.02(10)	2.01(2)	880
		1	2.54(7)	10.2(5)	1.57(7)	3.97(9)	1.99(2)	880
		2	2.88(8)	13.4(7)	2.07(10)	4.54(11)	2.13(3)	880
		3	2.95(8)	14.1(7)	2.17(10)	4.66(11)	2.16(3)	880
		4	3.13(8)	15.9(8)	2.44(12)	4.94(12)	2.22(3)	930
		5	3.13(8)	15.2(7)	2.34(11)	4.84(11)	2.20(3)	861
		6.1366	$20^3 \times 40$	Normal conf	2.49(9)	9.7(6)	1.49(10)	3.85(12)
4	3.21(11)			15.9(1.0)	2.44(16)	4.94(16)	2.22(4)	448
5	3.10(11)			14.9(1.0)	2.29(15)	4.78(15)	2.19(4)	450

D The numerical results of the scale parameter Σ_{RMT} and renormalized chiral condensate $\langle \bar{\psi}\psi \rangle_{\text{RMT}}^{\overline{\text{MS}}}$ in the $\overline{\text{MS}}$ -scheme at 2 [GeV]

Table 31. The scale parameter Σ_{RMT} of the distribution of the eigenvalues and renormalized chiral condensate $\langle \bar{\psi}\psi \rangle_{\text{RMT}}^{\overline{\text{MS}}}$ in the $\overline{\text{MS}}$ -scheme at 2 [GeV]. The renormalized chiral condensate of $\beta = 5.9044$, $V = 16^4$ is estimated using $\hat{Z}_S = 1.08(7)$ which is obtained by the interpolation of the numerical results of \hat{Z}_S .

β	V	m_c	$a^3 \Sigma_{\text{RMT}} \times 10^{-3}$	$\langle \bar{\psi}\psi \rangle_{\text{RMT}}^{\overline{\text{MS}}} [\text{GeV}^3] \times 10^{-2}$
5.8457	$12^3 \times 24$	N. C.	3.90(3)	-2.53(9)
		0	3.90(3)	-2.56(9)
		1	4.13(4)	-2.72(9)
		2	4.35(4)	-2.90(10)
		3	4.19(4)	-2.92(10)
5.9044	16^4	N. C.	2.833(18)	-2.40(16)
5.9256	$14^3 \times 28$	N. C.	2.77(3)	-2.58(9)
		0	2.69(2)	-2.58(9)
		1	2.92(2)	-2.53(9)
		2	3.15(3)	-2.70(9)
		3	3.24(3)	-2.94(10)
		4	3.21(3)	-3.04(11)
6.0000	$14^3 \times 28$	N. C.	1.820(11)	-2.21(7)
		0	1.794(9)	-2.16(7)
		1	1.928(11)	-2.41(8)
		2	2.213(13)	-2.68(9)
		3	2.350(15)	-2.81(10)
		4	2.411(14)	-2.98(10)
	$16^3 \times 32$	5	2.431(14)	-2.97(10)
		N. C.	2.023(18)	-2.58(9)
		0	1.982(17)	-2.57(9)
		1	2.026(17)	-2.62(9)
		2	2.273(19)	-2.89(10)
		3	2.41(2)	-3.04(10)
		4	2.414(19)	-3.07(10)
		5	2.41(2)	-3.09(11)
6.0522	$18^3 \times 32$	N. C.	1.535(13)	-2.45(8)
		0	1.529(13)	-2.44(8)
		1	1.629(14)	-2.62(9)
		2	1.781(15)	-2.84(10)
		3	1.921(18)	-3.03(10)
		4	2.018(18)	-3.20(11)
6.1366	$20^3 \times 40$	5	2.03(2)	-3.18(11)
		N. C.	1.064(14)	-2.48(9)
		4	1.381(17)	-3.11(11)
		5	1.50(2)	-3.39(12)

E The fitting results $a^4 G_{P-S}$ and am_{PS} and the numerical results of $(am_{PS})^2$ and af_{PS} **Table 32.** The fitting results of the correlation function C_{P-S} . The lattice is $\beta = 5.8457$, $V = 12^3 \times 24$. The normal configurations and configurations of $m_c = 0$ are used.

$\beta = 5.8457, V = 12^3 \times 24$							
Normal conf							
\bar{m}_{ud} [MeV]	$a\bar{m}_{ud}$ $\times 10^{-2}$	$a^4 G_{P-S}$ $\times 10^{-3}$	am_{PS}	$(am_{PS})^2$	af_{PS} $\times 10^{-2}$	FR: t/a	$\frac{\chi^2}{\text{dof}}$
40	2.5176	2.07(5)	0.2050(15)	$4.20(6) \times 10^{-2}$	5.45(14)	6-18	5.5/11.0
45	2.8324	2.18(4)	0.2187(14)	$4.78(6) \times 10^{-2}$	5.53(14)	6-18	8.6/11.0
50	3.1471	2.29(4)	0.2316(12)	$5.36(6) \times 10^{-2}$	5.62(12)	6-18	13.1/11.0
55	3.4618	2.56(6)	0.2484(16)	$6.17(8) \times 10^{-2}$	5.68(14)	7-17	2.3/9.0
60	3.7765	2.68(5)	0.2602(14)	$6.77(7) \times 10^{-2}$	5.77(13)	7-17	3.4/9.0
65	4.0912	2.79(5)	0.2713(13)	$7.36(7) \times 10^{-2}$	5.87(12)	7-17	4.9/9.0
70	4.4059	2.90(5)	0.2820(12)	$7.95(7) \times 10^{-2}$	5.97(11)	7-17	7.0/9.0
75	4.7206	3.01(4)	0.2922(11)	$8.54(7) \times 10^{-2}$	6.06(11)	7-17	9.7/9.0
80	5.0353	3.11(4)	0.3019(10)	$9.12(6) \times 10^{-2}$	6.16(10)	7-17	13.3/9.0
85	5.3500	3.43(7)	0.3160(15)	$9.98(9) \times 10^{-2}$	6.28(14)	8-16	1.4/7.0
90	5.6647	3.55(7)	0.3253(14)	0.1058(9)	6.38(13)	8-16	1.9/7.0
95	5.9794	3.68(6)	0.3342(13)	0.1117(9)	6.49(12)	8-16	2.7/7.0
100	6.2941	3.80(6)	0.3429(12)	0.1176(8)	6.60(11)	8-16	3.6/7.0
105	6.6088	3.92(6)	0.3512(12)	0.1233(8)	6.71(11)	8-16	4.8/7.0
110	6.9235	4.04(6)	0.3592(11)	0.1290(8)	6.82(10)	8-16	6.3/7.0
120	7.5529	4.27(5)	0.3743(10)	0.1401(7)	7.05(9)	8-16	10.6/7.0
130	8.1823	4.80(10)	0.3932(15)	0.1546(12)	7.33(16)	9-15	0.8/5.0
140	8.8117	5.06(9)	0.4066(14)	0.1654(11)	7.58(14)	9-15	1.3/5.0
150	9.4412	5.29(9)	0.4189(12)	0.1755(10)	7.82(13)	9-15	2.0/5.0
$m_c = 0$							
40	2.5176	2.05(5)	0.2028(16)	$4.11(7) \times 10^{-2}$	5.54(15)	6-18	5.5/11.0
45	2.8324	2.16(4)	0.2167(14)	$4.70(6) \times 10^{-2}$	5.61(15)	6-18	8.5/11.0
50	3.1471	2.27(4)	0.2298(13)	$5.28(6) \times 10^{-2}$	5.68(13)	6-18	12.6/11.0
55	3.4618	2.55(6)	0.2469(17)	$6.09(8) \times 10^{-2}$	5.73(15)	7-17	2.4/9.0
60	3.7765	2.66(5)	0.2588(15)	$6.70(8) \times 10^{-2}$	5.82(14)	7-17	3.4/9.0
65	4.0912	2.77(5)	0.2701(14)	$7.29(7) \times 10^{-2}$	5.91(12)	7-17	4.7/9.0
70	4.4059	2.88(5)	0.2808(13)	$7.89(7) \times 10^{-2}$	6.00(11)	7-17	6.6/9.0
75	4.7206	2.99(5)	0.2911(12)	$8.48(7) \times 10^{-2}$	6.09(10)	7-17	9.1/9.0
80	5.0353	3.09(4)	0.3010(11)	$9.06(6) \times 10^{-2}$	6.18(11)	7-17	12.4/9.0
85	5.3500	3.41(7)	0.3151(16)	$9.93(10) \times 10^{-2}$	6.29(14)	8-16	1.3/7.0
90	5.6647	3.54(7)	0.3245(15)	0.1053(9)	6.40(14)	8-16	1.8/7.0
95	5.9794	3.66(7)	0.3335(14)	0.1112(9)	6.50(13)	8-16	2.4/7.0
100	6.2941	3.78(6)	0.3422(13)	0.1171(9)	6.61(12)	8-16	3.2/7.0
105	6.6088	3.90(6)	0.3506(12)	0.1229(8)	6.72(11)	8-16	4.3/7.0
110	6.9235	4.02(6)	0.3587(11)	0.1286(8)	6.83(11)	8-16	5.7/7.0
120	7.5529	4.26(5)	0.3739(10)	0.1398(8)	7.05(10)	8-16	9.5/7.0
130	8.1823	4.79(10)	0.3928(16)	0.1543(12)	7.34(16)	9-15	0.7/5.0
140	8.8117	5.04(9)	0.4063(14)	0.1651(12)	7.58(15)	9-15	1.1/5.0
150	9.4412	5.27(9)	0.4186(13)	0.1753(11)	7.83(14)	9-15	1.8/5.0

Table 33. The fitting results of the correlation function \mathcal{C}_{P-S} . The lattice is $\beta = 5.8457$, $V = 12^3 \times 24$. The configurations of $m_c = 1$ and 2 are used.

$\beta = 5.8457, V = 12^3 \times 24$							
$m_c = 1$							
\bar{m}_{ud} [MeV]	$a\bar{m}_{ud}$ $\times 10^{-2}$	$a^4 G_{P-S}$ $\times 10^{-3}$	am_{PS}	$(am_{PS})^2$	af_{PS} $\times 10^{-2}$	FR: t/a	$\frac{\chi^2}{\text{dof}}$
40	2.5176	2.24(5)	0.2083(17)	$4.34(7) \times 10^{-2}$	5.49(15)	6-18	4.8/11.0
45	2.8324	2.35(5)	0.2217(15)	$4.91(6) \times 10^{-2}$	5.58(13)	6-18	7.6/11.0
50	3.1471	2.45(4)	0.2341(13)	$5.48(6) \times 10^{-2}$	5.68(13)	6-18	11.6/11.0
55	3.4618	2.54(4)	0.2458(12)	$6.04(6) \times 10^{-2}$	5.77(11)	6-18	17.1/11.0
60	3.7765	2.83(6)	0.2620(15)	$6.87(8) \times 10^{-2}$	5.85(14)	7-17	3.0/9.0
65	4.0912	2.93(6)	0.2729(14)	$7.45(8) \times 10^{-2}$	5.95(13)	7-17	4.3/9.0
70	4.4059	3.03(5)	0.2833(13)	$8.02(7) \times 10^{-2}$	6.05(12)	7-17	6.1/9.0
75	4.7206	3.13(5)	0.2932(12)	$8.60(7) \times 10^{-2}$	6.15(11)	7-17	8.4/9.0
80	5.0353	3.23(5)	0.3027(11)	$9.16(7) \times 10^{-2}$	6.25(11)	7-17	11.5/9.0
85	5.3500	3.55(8)	0.3165(16)	0.1002(10)	6.36(15)	8-16	1.2/7.0
90	5.6647	3.67(7)	0.3256(15)	0.1060(10)	6.47(14)	8-16	1.7/7.0
95	5.9794	3.78(7)	0.3344(14)	0.1118(9)	6.58(13)	8-16	2.2/7.0
100	6.2941	3.90(7)	0.3429(13)	0.1176(9)	6.68(13)	8-16	3.0/7.0
105	6.6088	4.01(7)	0.3511(13)	0.1233(9)	6.79(12)	8-16	4.0/7.0
110	6.9235	4.13(6)	0.3590(12)	0.1288(8)	6.90(11)	8-16	5.2/7.0
120	7.5529	4.34(6)	0.3739(11)	0.1398(8)	7.12(10)	8-16	8.7/7.0
130	8.1823	4.87(11)	0.3926(17)	0.1541(13)	7.41(17)	9-15	0.6/5.0
140	8.8117	5.11(10)	0.4059(15)	0.1647(12)	7.65(16)	9-15	1.0/5.0
150	9.4412	5.33(9)	0.4181(14)	0.1748(11)	7.89(15)	9-15	1.6/5.0
$m_c = 2$							
40	2.5176	2.22(5)	0.2052(16)	$4.21(7) \times 10^{-2}$	5.64(16)	6-18	5.3/11.0
45	2.8324	2.33(5)	0.2186(15)	$4.78(6) \times 10^{-2}$	5.73(15)	6-18	8.2/11.0
50	3.1471	2.43(4)	0.2310(13)	$5.34(6) \times 10^{-2}$	5.82(13)	6-18	12.1/11.0
55	3.4618	2.53(4)	0.2428(12)	$5.89(6) \times 10^{-2}$	5.91(13)	6-18	17.6/11.0
60	3.7765	2.82(6)	0.2591(16)	$6.71(8) \times 10^{-2}$	5.97(14)	7-17	3.1/9.0
65	4.0912	2.92(6)	0.2700(14)	$7.29(8) \times 10^{-2}$	6.07(13)	7-17	4.4/9.0
70	4.4059	3.03(5)	0.2804(13)	$7.86(7) \times 10^{-2}$	6.16(12)	7-17	6.2/9.0
75	4.7206	3.12(5)	0.2903(12)	$8.43(7) \times 10^{-2}$	6.26(11)	7-17	8.4/9.0
80	5.0353	3.22(5)	0.2998(11)	$8.99(7) \times 10^{-2}$	6.36(11)	7-17	11.5/9.0
85	5.3500	3.54(8)	0.3136(16)	$9.84(10) \times 10^{-2}$	6.47(15)	8-16	1.2/7.0
90	5.6647	3.65(7)	0.3227(15)	0.1041(10)	6.57(14)	8-16	1.7/7.0
95	5.9794	3.76(7)	0.3315(14)	0.1099(9)	6.68(14)	8-16	2.2/7.0
100	6.2941	3.87(7)	0.3399(13)	0.1155(9)	6.78(13)	8-16	3.0/7.0
105	6.6088	3.98(6)	0.3480(12)	0.1211(9)	6.89(12)	8-16	4.0/7.0
110	6.9235	4.09(6)	0.3559(12)	0.1266(8)	6.99(12)	8-16	5.2/7.0
120	7.5529	4.30(6)	0.3707(11)	0.1374(8)	7.21(10)	8-16	8.6/7.0
130	8.1823	4.81(11)	0.3893(16)	0.1515(13)	7.49(17)	9-15	0.6/5.0
140	8.8117	5.04(10)	0.4025(15)	0.1620(12)	7.72(16)	9-15	1.0/5.0
150	9.4412	5.25(9)	0.4146(14)	0.1719(11)	7.95(15)	9-15	1.6/5.0

Table 34. The fitting results of the correlation function \mathcal{C}_{P-S} . The lattice is $\beta = 5.8457$, $V = 12^3 \times 24$. The configurations of $m_c = 3$ and 4 are used.

$\beta = 5.8457, V = 12^3 \times 24$							
$m_c = 3$							
\bar{m}_{ud} [MeV]	$a\bar{m}_{ud}$ $\times 10^{-2}$	$a^4 G_{P-S}$ $\times 10^{-3}$	am_{PS}	$(am_{PS})^2$	af_{PS} $\times 10^{-2}$	FR: t/a	$\frac{\chi^2}{\text{dof}}$
40	2.5176	2.08(5)	0.2021(17)	$4.09(7) \times 10^{-2}$	5.63(16)	6-18	3.5/11.0
45	2.8324	2.19(5)	0.2154(15)	$4.64(6) \times 10^{-2}$	5.72(14)	6-18	5.8/11.0
50	3.1471	2.29(4)	0.2277(13)	$5.19(6) \times 10^{-2}$	5.81(14)	6-18	9.0/11.0
55	3.4618	2.38(4)	0.2393(12)	$5.73(6) \times 10^{-2}$	5.90(12)	6-18	13.5/11.0
60	3.7765	2.65(6)	0.2550(16)	$6.50(8) \times 10^{-2}$	5.97(15)	7-17	2.2/9.0
65	4.0912	2.74(5)	0.2658(14)	$7.06(8) \times 10^{-2}$	6.07(13)	7-17	3.2/9.0
70	4.4059	2.84(5)	0.2760(13)	$7.62(7) \times 10^{-2}$	6.17(12)	7-17	4.6/9.0
75	4.7206	2.94(5)	0.2858(12)	$8.17(7) \times 10^{-2}$	6.26(11)	7-17	6.5/9.0
80	5.0353	3.03(4)	0.2953(11)	$8.72(7) \times 10^{-2}$	6.36(11)	7-17	8.9/9.0
85	5.3500	3.12(4)	0.3043(11)	$9.26(6) \times 10^{-2}$	6.46(11)	7-17	12.2/9.0
90	5.6647	3.42(7)	0.3175(15)	0.1008(10)	6.57(15)	8-16	1.2/7.0
95	5.9794	3.53(7)	0.3262(14)	0.1064(9)	6.68(14)	8-16	1.7/7.0
100	6.2941	3.63(6)	0.3346(13)	0.1119(9)	6.78(13)	8-16	2.3/7.0
105	6.6088	3.74(6)	0.3427(13)	0.1174(9)	6.88(12)	8-16	3.1/7.0
110	6.9235	3.84(6)	0.3505(12)	0.1228(8)	6.99(12)	8-16	4.1/7.0
120	7.5529	4.04(6)	0.3652(11)	0.1334(8)	7.20(11)	8-16	6.9/7.0
130	8.1823	4.23(5)	0.3790(10)	0.1436(7)	7.41(10)	8-16	11.2/7.0
140	8.8117	4.72(10)	0.3967(15)	0.1574(12)	7.69(17)	9-15	0.8/5.0
150	9.4412	4.93(9)	0.4090(14)	0.1673(11)	7.92(15)	9-15	1.3/5.0

Table 35. The fitting results of the correlation function \mathcal{C}_{P-S} . The lattice is $\beta = 5.9256$, $V = 14^3 \times 28$. The normal configurations and configurations of $m_c = 0$ are used.

$\beta = 5.9256, V = 14^3 \times 28$							
Normal conf							
\bar{m}_{ud} [MeV]	$a\bar{m}_{ud}$ $\times 10^{-2}$	$a^4 G_{P-S}$ $\times 10^{-3}$	am_{PS}	$(am_{PS})^2$	af_{PS} $\times 10^{-2}$	FR: t/a	$\frac{\chi^2}{\text{dof}}$
35	1.8882	1.31(2)	0.1710(12)	$2.92(4) \times 10^{-2}$	4.67(11)	6-22	17.1/15.0
40	2.1580	1.48(3)	0.1878(13)	$3.53(5) \times 10^{-2}$	4.71(13)	7-21	6.3/13.0
45	2.4277	1.55(3)	0.1999(12)	$4.00(5) \times 10^{-2}$	4.78(11)	7-21	9.6/13.0
50	2.6975	1.62(3)	0.2113(10)	$4.46(4) \times 10^{-2}$	4.87(10)	7-21	14.4/13.0
55	2.9672	1.79(4)	0.2257(13)	$5.09(6) \times 10^{-2}$	4.93(11)	8-20	3.6/11.0
60	3.2370	1.87(3)	0.2360(12)	$5.57(5) \times 10^{-2}$	5.02(10)	8-20	5.2/11.0
65	3.5067	1.94(3)	0.2459(11)	$6.05(5) \times 10^{-2}$	5.11(9)	8-20	7.4/11.0
70	3.7765	2.01(3)	0.2553(10)	$6.52(5) \times 10^{-2}$	5.20(9)	8-20	10.5/11.0
75	4.0462	2.08(3)	0.2642(9)	$6.98(5) \times 10^{-2}$	5.29(8)	8-20	14.6/11.0
80	4.3160	2.28(4)	0.2764(12)	$7.64(7) \times 10^{-2}$	5.39(11)	9-19	2.5/9.0
85	4.5857	2.36(4)	0.2848(11)	$8.11(6) \times 10^{-2}$	5.49(10)	9-19	3.4/9.0
90	4.8555	2.44(4)	0.2930(10)	$8.58(6) \times 10^{-2}$	5.58(9)	9-19	4.7/9.0
95	5.1252	2.51(4)	0.3008(10)	$9.05(6) \times 10^{-2}$	5.68(9)	9-19	6.4/9.0
100	5.3949	2.59(4)	0.3082(9)	$9.50(6) \times 10^{-2}$	5.78(8)	9-19	8.5/9.0
105	5.6647	2.67(3)	0.3154(9)	$9.95(5) \times 10^{-2}$	5.88(9)	9-19	11.3/9.0
110	5.9344	2.89(5)	0.3257(12)	0.1061(8)	6.02(12)	10-18	1.2/7.0
120	6.4739	3.06(5)	0.3390(11)	0.1149(7)	6.23(11)	10-18	2.2/7.0
130	7.0134	3.22(5)	0.3512(10)	0.1233(7)	6.45(10)	10-18	3.6/7.0
140	7.5529	3.36(5)	0.3622(9)	0.1312(7)	6.67(9)	10-18	5.7/7.0
150	8.0924	3.47(4)	0.3722(8)	0.1385(6)	6.89(9)	10-18	8.5/7.0
$m_c = 0$							
35	1.8882	1.33(2)	0.1719(11)	$2.96(4) \times 10^{-2}$	4.66(11)	6-22	17.0/15.0
40	2.1580	1.49(3)	0.1884(13)	$3.55(5) \times 10^{-2}$	4.70(12)	7-21	5.8/13.0
45	2.4277	1.56(3)	0.2003(12)	$4.01(5) \times 10^{-2}$	4.78(11)	7-21	8.9/13.0
50	2.6975	1.63(3)	0.2115(10)	$4.47(4) \times 10^{-2}$	4.86(10)	7-21	13.3/13.0
55	2.9672	1.69(2)	0.2220(9)	$4.93(4) \times 10^{-2}$	4.95(9)	7-21	19.4/13.0
60	3.2370	1.86(3)	0.2358(12)	$5.56(6) \times 10^{-2}$	5.02(10)	8-20	4.5/11.0
65	3.5067	1.93(3)	0.2456(11)	$6.03(5) \times 10^{-2}$	5.11(9)	8-20	6.5/11.0
70	3.7765	2.00(3)	0.2549(10)	$6.50(5) \times 10^{-2}$	5.20(9)	8-20	9.2/11.0
75	4.0462	2.07(3)	0.2637(9)	$6.96(5) \times 10^{-2}$	5.29(9)	8-20	12.8/11.0
80	4.3160	2.25(4)	0.2757(12)	$7.60(7) \times 10^{-2}$	5.39(11)	9-19	2.0/9.0
85	4.5857	2.33(4)	0.2841(11)	$8.07(6) \times 10^{-2}$	5.49(10)	9-19	2.9/9.0
90	4.8555	2.41(4)	0.2922(10)	$8.54(6) \times 10^{-2}$	5.59(10)	9-19	4.0/9.0
95	5.1252	2.49(4)	0.2999(10)	$9.00(6) \times 10^{-2}$	5.68(9)	9-19	5.5/9.0
100	5.3949	2.56(4)	0.3074(9)	$9.45(6) \times 10^{-2}$	5.78(9)	9-19	7.4/9.0
105	5.6647	2.64(3)	0.3145(9)	$9.89(5) \times 10^{-2}$	5.88(9)	9-19	9.9/9.0
110	5.9344	2.71(3)	0.3214(8)	0.1033(5)	5.98(8)	9-19	13.1/9.0
120	6.4739	3.02(5)	0.3380(11)	0.1142(8)	6.23(11)	10-18	1.9/7.0
130	7.0134	3.18(5)	0.3502(10)	0.1226(7)	6.45(10)	10-18	3.2/7.0
140	7.5529	3.32(4)	0.3613(9)	0.1305(7)	6.66(10)	10-18	5.1/7.0
150	8.0924	3.43(4)	0.3713(8)	0.1378(6)	6.88(9)	10-18	7.7/7.0

Table 36. The fitting results of the correlation function \mathcal{C}_{P-S} . The lattice is $\beta = 5.9256$, $V = 14^3 \times 28$. The configurations of $m_c = 1$ and 2 are used.

$\beta = 5.9256, V = 14^3 \times 28$							
$m_c = 1$							
\bar{m}_{ud} [MeV]	$a\bar{m}_{ud}$ $\times 10^{-2}$	$a^4 G_{P-S}$ $\times 10^{-3}$	am_{PS}	$(am_{PS})^2$	af_{PS} $\times 10^{-2}$	FR: t/a	$\frac{\chi^2}{\text{dof}}$
35	1.8882	1.37(2)	0.1718(11)	$2.95(4) \times 10^{-2}$	4.73(11)	6-22	18.8/15.0
40	2.1580	1.55(3)	0.1889(12)	$3.57(5) \times 10^{-2}$	4.76(11)	7-21	7.0/13.0
45	2.4277	1.62(3)	0.2012(11)	$4.05(4) \times 10^{-2}$	4.84(10)	7-21	10.4/13.0
50	2.6975	1.70(3)	0.2126(10)	$4.52(4) \times 10^{-2}$	4.92(9)	7-21	15.8/13.0
55	2.9672	1.87(4)	0.2269(12)	$5.15(5) \times 10^{-2}$	4.99(11)	8-20	3.8/11.0
60	3.2370	1.95(3)	0.2373(11)	$5.63(5) \times 10^{-2}$	5.07(10)	8-20	5.6/11.0
65	3.5067	2.02(3)	0.2471(10)	$6.11(5) \times 10^{-2}$	5.16(9)	8-20	8.0/11.0
70	3.7765	2.09(3)	0.2565(9)	$6.58(5) \times 10^{-2}$	5.25(9)	8-20	11.4/11.0
75	4.0462	2.16(3)	0.2654(9)	$7.05(5) \times 10^{-2}$	5.34(8)	8-20	15.8/11.0
80	4.3160	2.36(4)	0.2775(11)	$7.70(6) \times 10^{-2}$	5.44(10)	9-19	2.6/9.0
85	4.5857	2.44(4)	0.2859(11)	$8.17(6) \times 10^{-2}$	5.54(10)	9-19	3.6/9.0
90	4.8555	2.52(4)	0.2940(10)	$8.64(6) \times 10^{-2}$	5.64(9)	9-19	5.0/9.0
95	5.1252	2.60(4)	0.3017(9)	$9.10(6) \times 10^{-2}$	5.74(9)	9-19	6.7/9.0
100	5.3949	2.67(3)	0.3091(9)	$9.56(5) \times 10^{-2}$	5.84(8)	9-19	9.0/9.0
105	5.6647	2.75(3)	0.3162(8)	0.1000(5)	5.94(8)	9-19	11.9/9.0
110	5.9344	2.97(5)	0.3264(12)	0.1066(8)	6.07(12)	10-18	1.3/7.0
120	6.4739	3.14(5)	0.3396(11)	0.1153(7)	6.29(11)	10-18	2.3/7.0
130	7.0134	3.29(5)	0.3517(10)	0.1237(7)	6.50(10)	10-18	3.8/7.0
140	7.5529	3.42(4)	0.3626(9)	0.1315(6)	6.72(9)	10-18	5.9/7.0
150	8.0924	3.53(4)	0.3725(8)	0.1388(6)	6.93(9)	10-18	8.8/7.0
$m_c = 2$							
35	1.8882	1.45(3)	0.1716(11)	$2.95(4) \times 10^{-2}$	4.87(12)	6-22	16.0/15.0
40	2.1580	1.62(3)	0.1883(13)	$3.55(5) \times 10^{-2}$	4.90(12)	7-21	5.7/13.0
45	2.4277	1.70(3)	0.2005(11)	$4.02(5) \times 10^{-2}$	4.98(11)	7-21	8.8/13.0
50	2.6975	1.77(3)	0.2118(10)	$4.49(4) \times 10^{-2}$	5.05(10)	7-21	13.2/13.0
55	2.9672	1.83(3)	0.2225(9)	$4.95(4) \times 10^{-2}$	5.13(9)	7-21	19.4/13.0
60	3.2370	2.02(4)	0.2363(11)	$5.58(5) \times 10^{-2}$	5.20(10)	8-20	4.6/11.0
65	3.5067	2.09(3)	0.2461(10)	$6.06(5) \times 10^{-2}$	5.29(9)	8-20	6.6/11.0
70	3.7765	2.16(3)	0.2555(10)	$6.53(5) \times 10^{-2}$	5.37(9)	8-20	9.3/11.0
75	4.0462	2.23(3)	0.2644(9)	$6.99(5) \times 10^{-2}$	5.46(9)	8-20	13.0/11.0
80	4.3160	2.42(4)	0.2763(12)	$7.63(7) \times 10^{-2}$	5.56(11)	9-19	2.1/9.0
85	4.5857	2.50(4)	0.2847(11)	$8.11(6) \times 10^{-2}$	5.65(10)	9-19	3.0/9.0
90	4.8555	2.58(4)	0.2928(10)	$8.57(6) \times 10^{-2}$	5.75(10)	9-19	4.1/9.0
95	5.1252	2.65(4)	0.3005(10)	$9.03(6) \times 10^{-2}$	5.84(9)	9-19	5.6/9.0
100	5.3949	2.73(4)	0.3080(9)	$9.48(6) \times 10^{-2}$	5.94(9)	9-19	7.5/9.0
105	5.6647	2.80(4)	0.3151(9)	$9.93(5) \times 10^{-2}$	6.04(9)	9-19	10.0/9.0
110	5.9344	2.87(3)	0.3219(8)	0.1036(5)	6.13(8)	9-19	13.1/9.0
120	6.4739	3.18(5)	0.3385(11)	0.1145(8)	6.38(11)	10-18	1.9/7.0
130	7.0134	3.33(5)	0.3506(10)	0.1229(7)	6.59(11)	10-18	3.2/7.0
140	7.5529	3.46(5)	0.3616(9)	0.1308(7)	6.80(10)	10-18	5.1/7.0
150	8.0924	3.57(4)	0.3716(8)	0.1381(6)	7.00(9)	10-18	7.8/7.0

Table 37. The fitting results of the correlation function \mathcal{C}_{P-S} . The lattice is $\beta = 5.9256$, $V = 14^3 \times 28$. The configurations of $m_c = 3$ and 4 are used.

$\beta = 5.9256, V = 14^3 \times 28$							
$m_c = 3$							
\bar{m}_{ud} [MeV]	$a\bar{m}_{ud}$ $\times 10^{-2}$	$a^4 G_{P-S}$ $\times 10^{-3}$	am_{PS}	$(am_{PS})^2$	af_{PS} $\times 10^{-2}$	FR: t/a	$\frac{\chi^2}{\text{dof}}$
35	1.8882	1.51(3)	0.1737(12)	$3.02(4) \times 10^{-2}$	4.86(12)	6-22	16.4/15.0
40	2.1580	1.69(4)	0.1900(13)	$3.61(5) \times 10^{-2}$	4.91(12)	7-21	6.0/13.0
45	2.4277	1.76(3)	0.2018(12)	$4.07(5) \times 10^{-2}$	5.00(12)	7-21	9.2/13.0
50	2.6975	1.83(3)	0.2128(10)	$4.53(4) \times 10^{-2}$	5.09(10)	7-21	13.8/13.0
55	2.9672	2.00(4)	0.2268(13)	$5.14(6) \times 10^{-2}$	5.16(12)	8-20	3.5/11.0
60	3.2370	2.07(4)	0.2369(12)	$5.61(5) \times 10^{-2}$	5.25(11)	8-20	5.0/11.0
65	3.5067	2.14(3)	0.2465(11)	$6.07(5) \times 10^{-2}$	5.34(10)	8-20	7.1/11.0
70	3.7765	2.21(3)	0.2556(10)	$6.54(5) \times 10^{-2}$	5.43(10)	8-20	9.9/11.0
75	4.0462	2.27(3)	0.2644(9)	$6.99(5) \times 10^{-2}$	5.52(9)	8-20	13.7/11.0
80	4.3160	2.47(5)	0.2763(12)	$7.63(7) \times 10^{-2}$	5.62(11)	9-19	2.4/9.0
85	4.5857	2.54(4)	0.2846(11)	$8.10(6) \times 10^{-2}$	5.71(11)	9-19	3.3/9.0
90	4.8555	2.62(4)	0.2926(10)	$8.56(6) \times 10^{-2}$	5.80(10)	9-19	4.4/9.0
95	5.1252	2.69(4)	0.3002(10)	$9.01(6) \times 10^{-2}$	5.90(9)	9-19	6.0/9.0
100	5.3949	2.76(4)	0.3076(9)	$9.46(6) \times 10^{-2}$	5.99(9)	9-19	8.0/9.0
105	5.6647	2.83(4)	0.3147(9)	$9.90(5) \times 10^{-2}$	6.09(9)	9-19	10.5/9.0
110	5.9344	2.90(3)	0.3214(8)	0.1033(5)	6.19(8)	9-19	13.7/9.0
120	6.4739	3.21(5)	0.3380(11)	0.1142(8)	6.43(12)	10-18	2.1/7.0
130	7.0134	3.36(5)	0.3501(10)	0.1226(7)	6.63(11)	10-18	3.4/7.0
140	7.5529	3.49(5)	0.3611(9)	0.1304(7)	6.84(10)	10-18	5.3/7.0
150	8.0924	3.59(4)	0.3711(8)	0.1377(6)	7.04(9)	10-18	7.9/7.0
$m_c = 4$							
35	1.8882	1.45(3)	0.1708(12)	$2.92(4) \times 10^{-2}$	4.93(12)	6-22	13.4/15.0
40	2.1580	1.53(2)	0.1835(10)	$3.37(4) \times 10^{-2}$	5.01(10)	6-22	22.5/15.0
45	2.4277	1.70(3)	0.1992(12)	$3.97(5) \times 10^{-2}$	5.05(12)	7-21	7.6/13.0
50	2.6975	1.77(3)	0.2104(10)	$4.43(4) \times 10^{-2}$	5.13(10)	7-21	11.7/13.0
55	2.9672	1.84(3)	0.2210(9)	$4.88(4) \times 10^{-2}$	5.21(9)	7-21	17.4/13.0
60	3.2370	2.02(4)	0.2346(12)	$5.50(5) \times 10^{-2}$	5.28(11)	8-20	4.2/11.0
65	3.5067	2.09(3)	0.2444(11)	$5.97(5) \times 10^{-2}$	5.37(10)	8-20	6.1/11.0
70	3.7765	2.16(3)	0.2537(10)	$6.44(5) \times 10^{-2}$	5.45(10)	8-20	8.7/11.0
75	4.0462	2.23(3)	0.2626(9)	$6.90(5) \times 10^{-2}$	5.54(9)	8-20	12.1/11.0
80	4.3160	2.29(3)	0.2711(8)	$7.35(5) \times 10^{-2}$	5.63(8)	8-20	16.7/11.0
85	4.5857	2.49(4)	0.2828(11)	$8.00(6) \times 10^{-2}$	5.73(11)	9-19	2.9/9.0
90	4.8555	2.57(4)	0.2908(10)	$8.46(6) \times 10^{-2}$	5.82(10)	9-19	3.9/9.0
95	5.1252	2.65(4)	0.2986(10)	$8.92(6) \times 10^{-2}$	5.91(9)	9-19	5.3/9.0
100	5.3949	2.72(4)	0.3060(9)	$9.36(6) \times 10^{-2}$	6.01(9)	9-19	7.1/9.0
105	5.6647	2.79(4)	0.3131(9)	$9.81(5) \times 10^{-2}$	6.10(9)	9-19	9.4/9.0
110	5.9344	2.86(3)	0.3200(8)	0.1024(5)	6.20(9)	9-19	12.2/9.0
120	6.4739	3.16(5)	0.3365(11)	0.1132(8)	6.43(12)	10-18	1.8/7.0
130	7.0134	3.30(5)	0.3486(10)	0.1215(7)	6.63(11)	10-18	3.0/7.0
140	7.5529	3.43(5)	0.3597(9)	0.1294(7)	6.84(10)	10-18	4.6/7.0
150	8.0924	3.54(5)	0.3698(9)	0.1368(6)	7.04(10)	10-18	6.8/7.0

Table 38. The fitting results of the correlation function \mathcal{C}_{P-S} . The lattice is $V = 14^3 \times 28$, $\beta = 5.9256$ and the magnetic charge is $m_c = 5$.

$\beta = 5.9256, V = 14^3 \times 28$							
$m_c = 5$							
\bar{m}_{ud} [MeV]	$a\bar{m}_{ud}$ $\times 10^{-2}$	$a^4 G_{P-S}$ $\times 10^{-3}$	am_{PS}	$(am_{PS})^2$	af_{PS} $\times 10^{-2}$	FR: t/a	$\frac{\chi^2}{\text{dof}}$
35	1.8882	1.44(3)	0.1710(11)	$2.92(4) \times 10^{-2}$	4.90(11)	6-22	17.0/15.0
40	2.1580	1.61(3)	0.1875(13)	$3.52(5) \times 10^{-2}$	4.93(12)	7-21	5.9/13.0
45	2.4277	1.69(3)	0.1996(11)	$3.98(4) \times 10^{-2}$	5.01(11)	7-21	9.1/13.0
50	2.6975	1.76(3)	0.2108(10)	$4.44(4) \times 10^{-2}$	5.09(10)	7-21	13.5/13.0
55	2.9672	1.83(3)	0.2214(9)	$4.90(4) \times 10^{-2}$	5.17(9)	7-21	19.6/13.0
60	3.2370	2.00(4)	0.2350(11)	$5.52(5) \times 10^{-2}$	5.25(10)	8-20	4.6/11.0
65	3.5067	2.07(3)	0.2448(10)	$5.99(5) \times 10^{-2}$	5.33(10)	8-20	6.5/11.0
70	3.7765	2.14(3)	0.2540(10)	$6.45(5) \times 10^{-2}$	5.41(9)	8-20	9.1/11.0
75	4.0462	2.21(3)	0.2628(9)	$6.91(5) \times 10^{-2}$	5.50(9)	8-20	12.5/11.0
80	4.3160	2.40(4)	0.2746(12)	$7.54(6) \times 10^{-2}$	5.60(11)	9-19	2.0/9.0
85	4.5857	2.47(4)	0.2829(11)	$8.00(6) \times 10^{-2}$	5.69(11)	9-19	2.8/9.0
90	4.8555	2.54(4)	0.2909(10)	$8.46(6) \times 10^{-2}$	5.79(10)	9-19	3.9/9.0
95	5.1252	2.62(4)	0.2986(10)	$8.92(6) \times 10^{-2}$	5.88(9)	9-19	5.1/9.0
100	5.3949	2.69(4)	0.3060(9)	$9.36(6) \times 10^{-2}$	5.97(9)	9-19	6.8/9.0
105	5.6647	2.75(4)	0.3131(9)	$9.80(5) \times 10^{-2}$	6.07(8)	9-19	9.0/9.0
110	5.9344	2.82(3)	0.3198(8)	0.1023(5)	6.16(9)	9-19	11.7/9.0
120	6.4739	3.12(5)	0.3362(11)	0.1130(8)	6.39(12)	10-18	1.6/7.0
130	7.0134	3.26(5)	0.3483(10)	0.1213(7)	6.60(11)	10-18	2.7/7.0
140	7.5529	3.38(5)	0.3594(9)	0.1292(7)	6.80(10)	10-18	4.3/7.0
150	8.0924	3.49(4)	0.3695(9)	0.1365(6)	7.00(9)	10-18	6.4/7.0

Table 39. The fitting results of the correlation function \mathcal{C}_{P-S} . The lattice is $V = 14^3 \times 28$, $\beta = 6.0000$, and the normal configurations are used.

$\beta = 6.0000, V = 14^3 \times 28$							
Normal conf							
\bar{m}_{ud} [MeV]	$a\bar{m}_{ud}$ $\times 10^{-2}$	$a^4 G_{P-S}$ $\times 10^{-3}$	am_{PS}	$(am_{PS})^2$	af_{PS} $\times 10^{-2}$	FR: t/a	$\frac{\chi^2}{\text{dof}}$
35	1.6522	0.901(16)	0.1580(10)	$2.50(3) \times 10^{-2}$	3.97(9)	6-22	8.9/15.0
40	1.8882	0.968(14)	0.1706(9)	$2.91(3) \times 10^{-2}$	4.04(8)	6-22	17.2/15.0
45	2.1243	1.094(19)	0.1857(11)	$3.45(4) \times 10^{-2}$	4.07(8)	7-21	5.1/13.0
50	2.3603	1.161(17)	0.1969(9)	$3.88(4) \times 10^{-2}$	4.15(7)	7-21	8.7/13.0
55	2.5963	1.224(16)	0.2073(9)	$4.30(4) \times 10^{-2}$	4.26(7)	7-21	14.2/13.0
60	2.8324	1.36(2)	0.2203(11)	$4.85(5) \times 10^{-2}$	4.30(8)	8-20	2.8/11.0
65	3.0684	1.42(2)	0.2298(10)	$5.28(4) \times 10^{-2}$	4.39(8)	8-20	4.5/11.0
70	3.3044	1.49(2)	0.2389(9)	$5.71(4) \times 10^{-2}$	4.47(7)	8-20	6.9/11.0
75	3.5404	1.558(19)	0.2475(8)	$6.13(4) \times 10^{-2}$	4.56(6)	8-20	10.2/11.0
80	3.7765	1.623(18)	0.2557(8)	$6.54(4) \times 10^{-2}$	4.65(6)	8-20	14.8/11.0
85	4.0125	1.78(3)	0.2669(10)	$7.12(6) \times 10^{-2}$	4.75(8)	9-19	2.1/9.0
90	4.2485	1.85(3)	0.2747(10)	$7.55(5) \times 10^{-2}$	4.85(8)	9-19	3.0/9.0
95	4.4846	1.93(3)	0.2822(9)	$7.96(5) \times 10^{-2}$	4.94(7)	9-19	4.4/9.0
100	4.7206	2.00(3)	0.2894(9)	$8.38(5) \times 10^{-2}$	5.04(7)	9-19	6.2/9.0
105	4.9566	2.07(3)	0.2963(8)	$8.78(5) \times 10^{-2}$	5.14(7)	9-19	8.5/9.0
110	5.1926	2.25(4)	0.3059(12)	$9.36(7) \times 10^{-2}$	5.26(10)	10-18	0.8/7.0
120	5.6647	2.41(4)	0.3189(10)	0.1017(7)	5.46(9)	10-18	1.5/7.0
130	6.1368	2.56(4)	0.3309(9)	0.1095(6)	5.67(9)	10-18	2.7/7.0
140	6.6088	2.71(3)	0.3420(8)	0.1169(6)	5.89(8)	10-18	4.6/7.0
150	7.0809	2.85(3)	0.3521(8)	0.1240(5)	6.10(7)	10-18	7.4/7.0

Table 40. The fitting results of the correlation function \mathcal{C}_{P-S} . The lattice is $\beta = 6.0000$, $V = 14^3 \times 28$. The configurations of $m_c = 0$ and 1 are used.

$\beta = 6.0000, V = 14^3 \times 28$							
$m_c = 0$							
\bar{m}_{ud} [MeV]	$a\bar{m}_{ud}$ $\times 10^{-2}$	$a^4 G_{P-S}$ $\times 10^{-3}$	am_{PS}	$(am_{PS})^2$	af_{PS} $\times 10^{-2}$	FR: t/a	$\frac{\chi^2}{\text{dof}}$
35	1.6522	0.933(16)	0.1607(10)	$2.58(3) \times 10^{-2}$	3.91(9)	6-22	12.1/15.0
40	1.8882	0.995(14)	0.1729(9)	$2.99(3) \times 10^{-2}$	3.98(7)	6-22	21.0/15.0
45	2.1243	1.120(19)	0.1878(10)	$3.53(4) \times 10^{-2}$	4.03(8)	7-21	6.09/13.0
50	2.3603	1.182(17)	0.1987(9)	$3.95(4) \times 10^{-2}$	4.11(7)	7-21	9.6/13.0
55	2.5963	1.242(16)	0.2089(8)	$4.36(4) \times 10^{-2}$	4.19(7)	7-21	14.9/13.0
60	2.8324	1.37(2)	0.2217(11)	$4.92(5) \times 10^{-2}$	4.27(8)	8-20	2.8/11.0
65	3.0684	1.44(2)	0.2311(10)	$5.34(4) \times 10^{-2}$	4.36(7)	8-20	4.3/11.0
70	3.3044	1.50(2)	0.2401(9)	$5.76(4) \times 10^{-2}$	4.44(7)	8-20	6.4/11.0
75	3.5404	1.568(19)	0.2487(8)	$6.18(4) \times 10^{-2}$	4.53(6)	8-20	9.4/11.0
80	3.7765	1.632(18)	0.2569(8)	$6.60(4) \times 10^{-2}$	4.62(6)	8-20	13.5/11.0
85	4.0125	1.78(3)	0.2678(10)	$7.17(5) \times 10^{-2}$	4.72(8)	9-19	1.7/9.0
90	4.2485	1.86(3)	0.2756(10)	$7.59(5) \times 10^{-2}$	4.82(8)	9-19	2.4/9.0
95	4.4846	1.93(3)	0.2831(9)	$8.01(5) \times 10^{-2}$	4.92(7)	9-19	3.5/9.0
100	4.7206	2.00(3)	0.2903(8)	$8.43(5) \times 10^{-2}$	5.01(7)	9-19	5.0/9.0
105	4.9566	2.07(2)	0.2972(8)	$8.83(5) \times 10^{-2}$	5.11(7)	9-19	6.9/9.0
110	5.1926	2.15(2)	0.3038(8)	$9.23(5) \times 10^{-2}$	5.21(6)	9-19	9.5/9.0
120	5.6647	2.40(4)	0.3195(10)	0.1021(7)	5.44(9)	10-18	1.1/7.0
130	6.1368	2.56(4)	0.3315(9)	0.1099(6)	5.65(9)	10-18	2.0/7.0
140	6.6088	2.71(3)	0.3426(8)	0.1174(6)	5.86(8)	10-18	3.5/7.0
150	7.0809	2.85(3)	0.3527(8)	0.1244(5)	6.08(7)	10-18	5.7/7.0
$m_c = 1$							
35	1.6522	0.965(17)	0.1599(10)	$2.56(3) \times 10^{-2}$	4.02(9)	6-22	14.6/15.0
40	1.8882	1.09(2)	0.1755(12)	$3.08(4) \times 10^{-2}$	4.05(10)	7-21	4.9/13.0
45	2.1243	1.16(2)	0.1870(11)	$3.50(4) \times 10^{-2}$	4.13(9)	7-21	7.8/13.0
50	2.3603	1.218(18)	0.1978(10)	$3.91(4) \times 10^{-2}$	4.21(8)	7-21	12.0/13.0
55	2.5963	1.278(17)	0.2080(9)	$4.33(4) \times 10^{-2}$	4.29(7)	7-21	18.0/13.0
60	2.8324	1.42(2)	0.2212(11)	$4.89(5) \times 10^{-2}$	4.36(8)	8-20	4.0/11.0
65	3.0684	1.48(2)	0.2306(10)	$5.32(5) \times 10^{-2}$	4.44(8)	8-20	5.9/11.0
70	3.3044	1.55(2)	0.2396(9)	$5.74(4) \times 10^{-2}$	4.53(7)	8-20	8.5/11.0
75	3.5404	1.61(2)	0.2481(8)	$6.16(4) \times 10^{-2}$	4.61(7)	8-20	12.0/11.0
80	3.7765	1.674(19)	0.2563(8)	$6.57(4) \times 10^{-2}$	4.70(7)	8-20	16.8/11.0
85	4.0125	1.84(3)	0.2676(10)	$7.16(6) \times 10^{-2}$	4.80(9)	9-19	2.5/9.0
90	4.2485	1.91(3)	0.2754(10)	$7.58(5) \times 10^{-2}$	4.89(8)	9-19	3.6/9.0
95	4.4846	1.98(3)	0.2829(9)	$8.00(5) \times 10^{-2}$	4.99(8)	9-19	5.0/9.0
100	4.7206	2.05(3)	0.2901(9)	$8.41(5) \times 10^{-2}$	5.08(7)	9-19	6.8/9.0
105	4.9566	2.12(3)	0.2970(8)	$8.82(5) \times 10^{-2}$	5.18(7)	9-19	9.2/9.0
110	5.1926	2.19(2)	0.3036(8)	$9.22(5) \times 10^{-2}$	5.27(7)	9-19	12.3/9.0
120	5.6647	2.46(4)	0.3196(10)	0.1022(7)	5.50(9)	10-18	1.6/7.0
130	6.1368	2.62(4)	0.3316(9)	0.1100(6)	5.71(9)	10-18	2.9/7.0
140	6.6088	2.76(4)	0.3426(8)	0.1174(6)	5.92(8)	10-18	4.9/7.0
150	7.0809	2.90(3)	0.3527(8)	0.1244(5)	6.13(7)	10-18	7.7/7.0

Table 41. The fitting results of the correlation function \mathcal{C}_{P-S} . The lattice is $\beta = 6.0000$, $V = 14^3 \times 28$. The configurations of $m_c = 2$ and 3 are used.

$\beta = 6.0000, V = 14^3 \times 28$							
$m_c = 2$							
\bar{m}_{ud} [MeV]	$a\bar{m}_{ud}$ $\times 10^{-2}$	$a^4 G_{P-S}$ $\times 10^{-3}$	am_{PS}	$(am_{PS})^2$	af_{PS} $\times 10^{-2}$	FR: t/a	$\frac{\chi^2}{\text{dof}}$
35	1.6522	1.045(17)	0.1599(10)	$2.56(3) \times 10^{-2}$	4.18(9)	6-22	11.9/15.0
40	1.8882	1.110(15)	0.1721(9)	$2.96(3) \times 10^{-2}$	4.25(8)	6-22	20.9/15.0
45	2.1243	1.24(2)	0.1869(10)	$3.49(4) \times 10^{-2}$	4.29(9)	7-21	6.8/13.0
50	2.3603	1.308(19)	0.1978(9)	$3.91(4) \times 10^{-2}$	4.37(8)	7-21	10.9/13.0
55	2.5963	1.369(17)	0.2079(8)	$4.32(3) \times 10^{-2}$	4.44(7)	7-21	16.7/13.0
60	2.8324	1.51(3)	0.2209(10)	$4.88(5) \times 10^{-2}$	4.51(8)	8-20	3.7/11.0
65	3.0684	1.58(2)	0.2303(9)	$5.30(4) \times 10^{-2}$	4.59(8)	8-20	5.6/11.0
70	3.3044	1.64(2)	0.2392(9)	$5.72(4) \times 10^{-2}$	4.68(7)	8-20	8.2/11.0
75	3.5404	1.70(2)	0.2478(8)	$6.14(4) \times 10^{-2}$	4.76(7)	8-20	11.7/11.0
80	3.7765	1.77(2)	0.2560(7)	$6.55(4) \times 10^{-2}$	4.85(7)	8-20	16.5/11.0
85	4.0125	1.93(3)	0.2671(10)	$7.13(5) \times 10^{-2}$	4.94(8)	9-19	2.5/9.0
90	4.2485	2.00(3)	0.2748(9)	$7.55(5) \times 10^{-2}$	5.03(8)	9-19	3.6/9.0
95	4.4846	2.07(3)	0.2823(9)	$7.97(5) \times 10^{-2}$	5.12(7)	9-19	5.0/9.0
100	4.7206	2.14(3)	0.2895(8)	$8.38(5) \times 10^{-2}$	5.21(7)	9-19	6.9/9.0
105	4.9566	2.21(3)	0.2964(8)	$8.78(5) \times 10^{-2}$	5.31(7)	9-19	9.4/9.0
110	5.1926	2.28(3)	0.3030(7)	$9.18(4) \times 10^{-2}$	5.40(7)	9-19	12.5/9.0
120	5.6647	2.54(4)	0.3189(10)	0.1017(6)	5.62(9)	10-18	1.7/7.0
130	6.1368	2.69(4)	0.3309(9)	0.1095(6)	5.82(8)	10-18	3.0/7.0
140	6.6088	2.84(3)	0.3420(8)	0.1169(6)	6.02(8)	10-18	5.0/7.0
150	7.0809	2.97(3)	0.3521(7)	0.1240(5)	6.22(7)	10-18	8.0/7.0
$m_c = 3$							
35	1.6522	1.126(19)	0.1625(10)	$2.64(3) \times 10^{-2}$	4.20(10)	6-22	9.5/15.0
40	1.8882	1.195(17)	0.1748(9)	$3.06(3) \times 10^{-2}$	4.27(8)	6-22	17.3/15.0
45	2.1243	1.33(2)	0.1894(10)	$3.59(4) \times 10^{-2}$	4.32(9)	7-21	5.5/13.0
50	2.3603	1.40(2)	0.2003(9)	$4.01(4) \times 10^{-2}$	4.40(8)	7-21	9.0/13.0
55	2.5963	1.460(19)	0.2105(9)	$4.43(4) \times 10^{-2}$	4.48(7)	7-21	14.0/13.0
60	2.8324	1.60(3)	0.2231(11)	$4.98(5) \times 10^{-2}$	4.55(9)	8-20	3.1/11.0
65	3.0684	1.67(3)	0.2325(10)	$5.40(5) \times 10^{-2}$	4.63(8)	8-20	4.6/11.0
70	3.3044	1.73(2)	0.2414(9)	$5.83(4) \times 10^{-2}$	4.72(7)	8-20	6.8/11.0
75	3.5404	1.79(2)	0.2499(8)	$6.24(4) \times 10^{-2}$	4.80(7)	8-20	9.8/11.0
80	3.7765	1.86(2)	0.2580(8)	$6.65(4) \times 10^{-2}$	4.89(7)	8-20	13.9/11.0
85	4.0125	2.02(3)	0.2688(10)	$7.23(6) \times 10^{-2}$	4.99(9)	9-19	2.1/9.0
90	4.2485	2.09(3)	0.2765(10)	$7.65(5) \times 10^{-2}$	5.08(8)	9-19	2.9/9.0
95	4.4846	2.16(3)	0.2839(9)	$8.06(5) \times 10^{-2}$	5.17(8)	9-19	4.1/9.0
100	4.7206	2.22(3)	0.2910(9)	$8.47(5) \times 10^{-2}$	5.26(7)	9-19	5.7/9.0
105	4.9566	2.29(3)	0.2978(8)	$8.87(5) \times 10^{-2}$	5.35(7)	9-19	7.7/9.0
110	5.1926	2.36(3)	0.3044(8)	$9.27(5) \times 10^{-2}$	5.44(7)	9-19	10.4/9.0
120	5.6647	2.62(4)	0.3200(10)	0.1024(7)	5.66(10)	10-18	1.4/7.0
130	6.1368	2.77(4)	0.3319(9)	0.1102(6)	5.86(9)	10-18	2.4/7.0
140	6.6088	2.90(4)	0.3429(9)	0.1176(6)	6.06(8)	10-18	4.1/7.0
150	7.0809	3.03(4)	0.3530(8)	0.1246(6)	6.25(8)	10-18	6.5/7.0

Table 42. The fitting results of the correlation function \mathcal{C}_{P-S} . The lattice is $\beta = 6.0000$, $V = 14^3 \times 28$. The configurations of $m_c = 4$ and 5 are used.

$\beta = 6.0000, V = 14^3 \times 28$							
$m_c = 4$							
\bar{m}_{ud} [MeV]	$a\bar{m}_{ud}$ $\times 10^{-2}$	$a^4 G_{P-S}$ $\times 10^{-3}$	am_{PS}	$(am_{PS})^2$	af_{PS} $\times 10^{-2}$	FR: t/a	$\frac{\chi^2}{\text{dof}}$
35	1.6522	1.149(19)	0.1621(10)	$2.63(3) \times 10^{-2}$	4.27(9)	6-22	8.8/15.0
40	1.8882	1.216(17)	0.1742(9)	$3.03(3) \times 10^{-2}$	4.34(8)	6-22	15.8/15.0
45	2.1243	1.35(2)	0.1885(10)	$3.55(4) \times 10^{-2}$	4.39(9)	7-21	4.5/13.0
50	2.3603	1.41(2)	0.1993(9)	$3.97(4) \times 10^{-2}$	4.47(8)	7-21	7.4/13.0
55	2.5963	1.48(2)	0.2095(8)	$4.39(3) \times 10^{-2}$	4.54(7)	7-21	11.7/13.0
60	2.8324	1.534(17)	0.2190(8)	$4.80(3) \times 10^{-2}$	4.62(7)	7-21	18.0/13.0
65	3.0684	1.67(2)	0.2312(9)	$5.35(4) \times 10^{-2}$	4.70(8)	8-20	3.5/11.0
70	3.3044	1.74(2)	0.2402(9)	$5.77(4) \times 10^{-2}$	4.78(7)	8-20	5.3/11.0
75	3.5404	1.80(2)	0.2487(8)	$6.18(4) \times 10^{-2}$	4.86(7)	8-20	7.8/11.0
80	3.7765	1.87(2)	0.2569(7)	$6.60(4) \times 10^{-2}$	4.94(7)	8-20	11.3/11.0
85	4.0125	1.93(2)	0.2647(7)	$7.01(4) \times 10^{-2}$	5.03(6)	8-20	16.0/11.0
90	4.2485	2.09(3)	0.2752(9)	$7.57(5) \times 10^{-2}$	5.12(8)	9-19	2.1/9.0
95	4.4846	2.16(3)	0.2827(9)	$7.99(5) \times 10^{-2}$	5.21(8)	9-19	3.1/9.0
100	4.7206	2.23(3)	0.2898(8)	$8.40(5) \times 10^{-2}$	5.30(7)	9-19	4.4/9.0
105	4.9566	2.29(3)	0.2968(8)	$8.81(5) \times 10^{-2}$	5.39(7)	9-19	6.1/9.0
110	5.1926	2.36(3)	0.3034(7)	$9.21(4) \times 10^{-2}$	5.48(6)	9-19	8.3/9.0
120	5.6647	2.61(4)	0.3189(10)	0.1017(6)	5.69(10)	10-18	1.0/7.0
130	6.1368	2.76(4)	0.3310(9)	0.1095(6)	5.89(9)	10-18	1.8/7.0
140	6.6088	2.90(4)	0.3422(8)	0.1171(6)	6.08(8)	10-18	3.1/7.0
150	7.0809	3.03(3)	0.3525(8)	0.1242(5)	6.28(8)	10-18	5.1/7.0
$m_c = 5$							
35	1.6522	1.137(18)	0.1613(10)	$2.60(3) \times 10^{-2}$	4.28(9)	6-22	7.1/15.0
40	1.8882	1.208(17)	0.1737(9)	$3.02(3) \times 10^{-2}$	4.35(8)	6-22	13.5/15.0
45	2.1243	1.269(15)	0.1848(8)	$3.42(3) \times 10^{-2}$	4.43(7)	6-22	23.3/15.0
50	2.3603	1.41(2)	0.1988(9)	$3.95(4) \times 10^{-2}$	4.48(8)	7-21	5.5/13.0
55	2.5963	1.467(18)	0.2089(8)	$4.37(3) \times 10^{-2}$	4.56(7)	7-21	9.1/13.0
60	2.8324	1.529(17)	0.2186(7)	$4.78(3) \times 10^{-2}$	4.63(7)	7-21	14.4/13.0
65	3.0684	1.66(2)	0.2306(9)	$5.32(4) \times 10^{-2}$	4.71(8)	8-20	2.2/11.0
70	3.3044	1.73(2)	0.2396(9)	$5.74(4) \times 10^{-2}$	4.79(7)	8-20	3.5/11.0
75	3.5404	1.79(2)	0.2482(8)	$6.16(4) \times 10^{-2}$	4.87(7)	8-20	5.5/11.0
80	3.7765	1.86(2)	0.2564(7)	$6.58(4) \times 10^{-2}$	4.95(6)	8-20	8.2/11.0
85	4.0125	1.921(19)	0.2643(7)	$6.99(4) \times 10^{-2}$	5.03(6)	8-20	12.1/11.0
90	4.2485	2.07(3)	0.2746(9)	$7.54(5) \times 10^{-2}$	5.13(8)	9-19	1.2/9.0
95	4.4846	2.14(3)	0.2821(9)	$7.96(5) \times 10^{-2}$	5.21(7)	9-19	1.9/9.0
100	4.7206	2.21(3)	0.2894(8)	$8.37(5) \times 10^{-2}$	5.30(7)	9-19	2.8/9.0
105	4.9566	2.28(3)	0.2964(8)	$8.79(4) \times 10^{-2}$	5.39(7)	9-19	4.0/9.0
110	5.1926	2.35(3)	0.3032(7)	$9.19(4) \times 10^{-2}$	5.48(6)	9-19	5.7/9.0
120	5.6647	2.49(2)	0.3160(6)	$9.98(4) \times 10^{-2}$	5.66(6)	9-19	10.6/9.0
130	6.1368	2.74(4)	0.3307(9)	0.1094(6)	5.88(9)	10-18	1.0/7.0
140	6.6088	2.89(4)	0.3421(8)	0.1170(6)	6.07(8)	10-18	1.9/7.0
150	7.0809	3.03(3)	0.3527(7)	0.1244(5)	6.26(7)	10-18	3.4/7.00

Table 43. The fitting results of the correlation function \mathcal{C}_{P-S} . The lattice is $\beta = 6.0000$, $V = 16^3 \times 32$. The normal configurations and configurations of $m_c = 0$ are used.

$\beta = 6.0000, V = 16^3 \times 32$							
Normal conf							
\bar{m}_{ud} [MeV]	$a\bar{m}_{ud}$ $\times 10^{-2}$	$a^4 G_{P-S}$ $\times 10^{-3}$	am_{PS}	$(am_{PS})^2$	af_{PS} $\times 10^{-2}$	FR: t/a	$\frac{\chi^2}{\text{dof}}$
30	1.4162	0.916(17)	0.1472(10)	$2.17(3) \times 10^{-2}$	3.96(9)	7-25	14.7/17.0
35	1.6522	0.970(14)	0.1597(8)	$2.55(3) \times 10^{-2}$	4.04(9)	7-25	24.8/17.0
40	1.8882	1.080(18)	0.1742(9)	$3.04(3) \times 10^{-2}$	4.09(8)	8-24	10.5/15.0
45	2.1243	1.130(16)	0.1850(8)	$3.42(3) \times 10^{-2}$	4.17(7)	8-24	16.1/15.0
50	2.3603	1.24(2)	0.1977(9)	$3.91(4) \times 10^{-2}$	4.25(8)	9-23	5.1/13.0
55	2.5963	1.287(19)	0.2074(8)	$4.30(4) \times 10^{-2}$	4.33(8)	9-23	7.5/13.0
60	2.8324	1.337(18)	0.2165(8)	$4.69(3) \times 10^{-2}$	4.42(7)	9-23	10.9/13.0
65	3.0684	1.385(16)	0.2252(7)	$5.07(3) \times 10^{-2}$	4.50(6)	9-23	15.6/13.0
70	3.3044	1.50(2)	0.2361(9)	$5.57(4) \times 10^{-2}$	4.60(8)	10-22	3.5/11.0
75	3.5404	1.56(2)	0.2442(8)	$5.96(4) \times 10^{-2}$	4.68(7)	10-22	5.0/11.0
80	3.7765	1.61(2)	0.2519(8)	$6.35(4) \times 10^{-2}$	4.77(7)	10-22	7.1/11.0
85	4.0125	1.66(2)	0.2593(7)	$6.73(4) \times 10^{-2}$	4.87(7)	10-22	9.8/11.0
90	4.2485	1.715(19)	0.2664(7)	$7.10(3) \times 10^{-2}$	4.96(6)	10-22	13.5/11.0
95	4.4846	1.85(3)	0.2757(9)	$7.60(5) \times 10^{-2}$	5.07(8)	11-21	2.2/9.0
100	4.7206	1.91(3)	0.2824(8)	$7.97(5) \times 10^{-2}$	5.17(8)	11-21	3.0/9.0
105	4.9566	1.96(3)	0.2887(8)	$8.34(4) \times 10^{-2}$	5.27(7)	11-21	4.1/9.0
110	5.1926	2.02(3)	0.2948(7)	$8.69(4) \times 10^{-2}$	5.37(7)	11-21	5.5/9.0
120	5.6647	2.12(2)	0.3062(6)	$9.37(4) \times 10^{-2}$	5.56(7)	11-21	9.4/9.0
130	6.1368	2.31(4)	0.3189(9)	0.1017(6)	5.80(10)	12-20	1.3/7.0
140	6.6088	2.40(3)	0.3284(8)	0.1078(5)	6.01(9)	12-20	2.1/7.0
150	7.0809	2.47(3)	0.3367(7)	0.1134(5)	6.21(8)	12-20	3.2/7.0
$m_c = 0$							
30	1.4162	0.892(17)	0.1454(10)	$2.11(3) \times 10^{-2}$	4.00(10)	7-25	9.4/17.0
35	1.6522	0.945(15)	0.1580(9)	$2.49(3) \times 10^{-2}$	4.07(8)	7-25	16.6/17.0
40	1.8882	1.048(19)	0.1723(10)	$2.97(3) \times 10^{-2}$	4.12(9)	8-24	6.5/15.0
45	2.1243	1.097(17)	0.1831(9)	$3.35(3) \times 10^{-2}$	4.20(8)	8-24	10.5/15.0
50	2.3603	1.144(15)	0.1933(8)	$3.74(3) \times 10^{-2}$	4.27(7)	8-24	16.5/15.0
55	2.5963	1.25(2)	0.2055(9)	$4.22(4) \times 10^{-2}$	4.35(8)	9-23	4.7/13.0
60	2.8324	1.300(19)	0.2148(8)	$4.61(4) \times 10^{-2}$	4.43(7)	9-23	7.1/13.0
65	3.0684	1.349(17)	0.2235(8)	$5.00(3) \times 10^{-2}$	4.51(7)	9-23	10.5/13.0
70	3.3044	1.398(16)	0.2319(7)	$5.38(3) \times 10^{-2}$	4.59(6)	9-23	15.4/13.0
75	3.5404	1.52(2)	0.2425(9)	$5.88(4) \times 10^{-2}$	4.69(8)	10-22	3.2/11.0
80	3.7765	1.57(2)	0.2503(8)	$6.27(4) \times 10^{-2}$	4.78(7)	10-22	4.7/11.0
85	4.0125	1.62(2)	0.2578(8)	$6.65(4) \times 10^{-2}$	4.87(7)	10-22	6.7/11.0
90	4.2485	1.68(2)	0.2650(7)	$7.02(4) \times 10^{-2}$	4.96(7)	10-22	9.4/11.0
95	4.4846	1.730(19)	0.2718(7)	$7.39(4) \times 10^{-2}$	5.05(6)	10-22	13.0/11.0
100	4.7206	1.87(3)	0.2809(9)	$7.89(5) \times 10^{-2}$	5.17(9)	11-21	2.0/9.0
105	4.9566	1.92(3)	0.2874(9)	$8.26(5) \times 10^{-2}$	5.26(8)	11-21	2.8/9.0
110	5.1926	1.98(3)	0.2935(8)	$8.62(5) \times 10^{-2}$	5.36(8)	11-21	3.8/9.0
120	5.6647	2.08(3)	0.3050(7)	$9.30(4) \times 10^{-2}$	5.56(7)	11-21	6.7/9.0
130	6.1368	2.18(2)	0.3154(7)	$9.95(4) \times 10^{-2}$	5.76(7)	11-21	11.1/9.0
140	6.6088	2.37(4)	0.3274(9)	0.1072(6)	6.00(10)	12-20	1.5/7.0
150	7.0809	2.44(3)	0.3358(8)	0.1128(6)	6.20(9)	12-20	2.3/7.0

Table 44. The fitting results of the correlation function \mathcal{C}_{P-S} . The lattice is $\beta = 6.0000$, $V = 16^3 \times 32$. The configurations of $m_c = 1$ and 2 are used.

$\beta = 6.0000, V = 16^3 \times 32$							
$m_c = 1$							
\bar{m}_{ud} [MeV]	$a\bar{m}_{ud}$ $\times 10^{-2}$	$a^4 G_{P-S}$ $\times 10^{-3}$	am_{PS}	$(am_{PS})^2$	af_{PS} $\times 10^{-2}$	FR: t/a	$\frac{\chi^2}{\text{dof}}$
30	1.4162	0.903(18)	0.1434(10)	$2.06(3) \times 10^{-2}$	4.14(12)	7-25	11.1/17.0
35	1.6522	1.01(2)	0.1591(11)	$2.53(4) \times 10^{-2}$	4.16(12)	8-24	5.0/15.0
40	1.8882	1.12(3)	0.1733(13)	$3.00(5) \times 10^{-2}$	4.20(12)	9-23	1.7/13.0
45	2.1243	1.17(3)	0.1846(11)	$3.41(4) \times 10^{-2}$	4.27(10)	9-23	2.7/13.0
50	2.3603	1.23(2)	0.1951(10)	$3.81(4) \times 10^{-2}$	4.35(9)	9-23	4.0/13.0
55	2.5963	1.28(2)	0.2051(9)	$4.21(4) \times 10^{-2}$	4.42(8)	9-23	6.0/13.0
60	2.8324	1.333(19)	0.2145(8)	$4.60(4) \times 10^{-2}$	4.50(8)	9-23	8.7/13.0
65	3.0684	1.383(18)	0.2234(8)	$4.99(3) \times 10^{-2}$	4.57(7)	9-23	12.5/13.0
70	3.3044	1.432(17)	0.2318(7)	$5.37(3) \times 10^{-2}$	4.65(6)	9-23	17.8/13.0
75	3.5404	1.56(2)	0.2426(9)	$5.88(4) \times 10^{-2}$	4.75(8)	10-22	4.1/11.0
80	3.7765	1.61(2)	0.2504(8)	$6.27(4) \times 10^{-2}$	4.83(7)	10-22	5.8/11.0
85	4.0125	1.66(2)	0.2580(8)	$6.65(4) \times 10^{-2}$	4.93(7)	10-22	8.1/11.0
90	4.2485	1.72(2)	0.2651(7)	$7.03(4) \times 10^{-2}$	5.02(7)	10-22	11.0/11.0
95	4.4846	1.77(2)	0.2720(7)	$7.40(4) \times 10^{-2}$	5.10(7)	10-22	14.8/11.0
100	4.7206	1.820(19)	0.2786(6)	$7.76(4) \times 10^{-2}$	5.19(6)	10-22	19.7/11.0
105	4.9566	1.97(3)	0.2877(9)	$8.28(5) \times 10^{-2}$	5.31(8)	11-21	3.4/9.0
110	5.1926	2.02(3)	0.2939(8)	$8.64(5) \times 10^{-2}$	5.41(8)	11-21	4.5/9.0
120	5.6647	2.12(3)	0.3053(7)	$9.32(4) \times 10^{-2}$	5.60(7)	11-21	7.6/9.0
130	6.1368	2.21(2)	0.3157(7)	$9.96(4) \times 10^{-2}$	5.80(7)	11-21	12.2/9.0
140	6.6088	2.41(4)	0.3277(9)	0.1074(6)	6.04(10)	12-20	1.7/7.0
150	7.0809	2.48(4)	0.3362(8)	0.1130(6)	6.23(9)	12-20	2.6/7.0
$m_c = 2$							
30	1.4162	1.012(19)	0.1466(10)	$2.15(3) \times 10^{-2}$	4.19(10)	7-25	14.6/17.0
35	1.6522	1.067(17)	0.1591(9)	$2.53(3) \times 10^{-2}$	4.26(10)	7-25	24.0/17.0
40	1.8882	1.18(2)	0.1737(10)	$3.02(3) \times 10^{-2}$	4.31(9)	8-24	10.6/15.0
45	2.1243	1.233(18)	0.1845(8)	$3.41(3) \times 10^{-2}$	4.38(8)	8-24	15.8/15.0
50	2.3603	1.35(2)	0.1974(10)	$3.90(4) \times 10^{-2}$	4.45(9)	9-23	5.3/13.0
55	2.5963	1.40(2)	0.2072(9)	$4.29(4) \times 10^{-2}$	4.52(9)	9-23	7.6/13.0
60	2.8324	1.45(2)	0.2164(8)	$4.68(4) \times 10^{-2}$	4.60(8)	9-23	10.8/13.0
65	3.0684	1.495(19)	0.2251(7)	$5.07(3) \times 10^{-2}$	4.68(7)	9-23	15.2/13.0
70	3.3044	1.62(3)	0.2361(9)	$5.57(4) \times 10^{-2}$	4.77(9)	10-22	3.7/11.0
75	3.5404	1.67(2)	0.2442(9)	$5.97(4) \times 10^{-2}$	4.85(8)	10-22	5.1/11.0
80	3.7765	1.73(2)	0.2520(8)	$6.35(4) \times 10^{-2}$	4.94(7)	10-22	7.1/11.0
85	4.0125	1.78(2)	0.2595(7)	$6.73(4) \times 10^{-2}$	5.03(7)	10-22	9.8/11.0
90	4.2485	1.83(2)	0.2666(7)	$7.11(4) \times 10^{-2}$	5.11(7)	10-22	13.2/11.0
95	4.4846	1.97(3)	0.2760(9)	$7.62(5) \times 10^{-2}$	5.22(9)	11-21	2.3/9.0
100	4.7206	2.03(3)	0.2827(9)	$7.99(5) \times 10^{-2}$	5.32(8)	11-21	3.1/9.0
105	4.9566	2.08(3)	0.2892(8)	$8.36(5) \times 10^{-2}$	5.41(8)	11-21	4.2/9.0
110	5.1926	2.14(3)	0.2953(8)	$8.72(5) \times 10^{-2}$	5.51(8)	11-21	5.6/9.0
120	5.6647	2.24(3)	0.3067(7)	$9.41(4) \times 10^{-2}$	5.70(7)	11-21	9.3/9.0
130	6.1368	2.44(4)	0.3196(9)	0.1022(6)	5.93(10)	12-20	1.4/7.0
140	6.6088	2.52(4)	0.3292(9)	0.1084(6)	6.13(10)	12-20	2.2/7.0
150	7.0809	2.59(4)	0.3377(8)	0.1140(5)	6.32(9)	12-20	3.3/7.0

Table 45. The fitting results of the correlation function \mathcal{C}_{P-S} . The lattice is $\beta = 6.0000$, $V = 16^3 \times 32$. The configurations of $m_c = 3$ and 4 are used.

$\beta = 6.0000, V = 16^3 \times 32$							
$m_c = 3$							
\bar{m}_{ud} [MeV]	$a\bar{m}_{ud}$ $\times 10^{-2}$	$a^4 G_{P-S}$ $\times 10^{-3}$	am_{PS}	$(am_{PS})^2$	af_{PS} $\times 10^{-2}$	FR: t/a	$\frac{\chi^2}{\text{dof}}$
30	1.4162	1.08(2)	0.1481(10)	$2.19(3) \times 10^{-2}$	4.25(10)	7-25	13.4/17.0
35	1.6522	1.139(18)	0.1606(9)	$2.58(3) \times 10^{-2}$	4.32(10)	7-25	22.4/17.0
40	1.8882	1.26(2)	0.1750(10)	$3.06(3) \times 10^{-2}$	4.37(10)	8-24	10.3/15.0
45	2.1243	1.31(2)	0.1858(9)	$3.45(3) \times 10^{-2}$	4.45(8)	8-24	15.4/15.0
50	2.3603	1.42(3)	0.1986(10)	$3.94(4) \times 10^{-2}$	4.52(9)	9-23	5.4/13.0
55	2.5963	1.47(2)	0.2083(9)	$4.34(4) \times 10^{-2}$	4.60(9)	9-23	7.7/13.0
60	2.8324	1.52(2)	0.2174(8)	$4.73(4) \times 10^{-2}$	4.67(8)	9-23	10.9/13.0
65	3.0684	1.57(2)	0.2261(8)	$5.11(3) \times 10^{-2}$	4.75(7)	9-23	15.1/13.0
70	3.3044	1.69(3)	0.2370(9)	$5.62(4) \times 10^{-2}$	4.84(9)	10-22	3.9/11.0
75	3.5404	1.75(3)	0.2451(9)	$6.01(4) \times 10^{-2}$	4.93(8)	10-22	5.3/11.0
80	3.7765	1.80(3)	0.2529(8)	$6.39(4) \times 10^{-2}$	5.01(8)	10-22	7.3/11.0
85	4.0125	1.85(2)	0.2602(8)	$6.77(4) \times 10^{-2}$	5.10(8)	10-22	9.9/11.0
90	4.2485	1.90(2)	0.2673(7)	$7.15(4) \times 10^{-2}$	5.18(7)	10-22	13.3/11.0
95	4.4846	2.04(3)	0.2767(9)	$7.65(5) \times 10^{-2}$	5.29(9)	11-21	2.5/9.0
100	4.7206	2.10(3)	0.2833(9)	$8.03(5) \times 10^{-2}$	5.38(9)	11-21	3.3/9.0
105	4.9566	2.15(3)	0.2897(8)	$8.39(5) \times 10^{-2}$	5.49(8)	11-21	4.4/9.0
110	5.1926	2.20(3)	0.2958(8)	$8.75(5) \times 10^{-2}$	5.57(8)	11-21	5.7/9.0
120	5.6647	2.30(3)	0.3071(7)	$9.43(4) \times 10^{-2}$	5.76(8)	11-21	9.5/9.0
130	6.1368	2.50(4)	0.3200(10)	0.1024(6)	5.99(11)	12-20	1.5/7.0
140	6.6088	2.58(4)	0.3295(9)	0.1086(6)	6.18(10)	12-20	2.3/7.0
150	7.0809	2.64(4)	0.3379(8)	0.1142(5)	6.37(9)	12-20	3.4/7.0
$m_c = 4$							
30	1.4162	1.10(2)	0.1484(10)	$2.20(3) \times 10^{-2}$	4.26(10)	7-25	10.4/17.0
35	1.6522	1.152(17)	0.1610(8)	$2.59(3) \times 10^{-2}$	4.33(8)	7-25	17.9/17.0
40	1.8882	1.26(2)	0.1752(9)	$3.07(3) \times 10^{-2}$	4.38(9)	8-24	7.4/15.0
45	2.1243	1.314(19)	0.1860(8)	$3.46(3) \times 10^{-2}$	4.45(8)	8-24	11.5/15.0
50	2.3603	1.360(17)	0.1961(7)	$3.85(3) \times 10^{-2}$	4.53(7)	8-24	17.4/15.0
55	2.5963	1.47(2)	0.2082(9)	$4.33(4) \times 10^{-2}$	4.60(8)	9-23	5.3/13.0
60	2.8324	1.52(2)	0.2174(8)	$4.73(3) \times 10^{-2}$	4.67(8)	9-23	7.9/13.0
65	3.0684	1.57(19)	0.2261(7)	$5.11(3) \times 10^{-2}$	4.75(7)	9-23	11.5/13.0
70	3.3044	1.616(18)	0.2344(7)	$5.50(3) \times 10^{-2}$	4.83(6)	9-23	16.5/13.0
75	3.5404	1.74(3)	0.2448(8)	$5.99(4) \times 10^{-2}$	4.92(8)	10-22	3.9/11.0
80	3.7765	1.79(2)	0.2526(8)	$6.38(4) \times 10^{-2}$	5.01(7)	10-22	5.5/11.0
85	4.0125	1.84(2)	0.2601(7)	$6.76(4) \times 10^{-2}$	5.09(7)	10-22	7.8/11.0
90	4.2485	1.89(2)	0.2672(7)	$7.14(4) \times 10^{-2}$	5.18(7)	10-22	10.9/11.0
95	4.4846	1.94(2)	0.2740(6)	$7.51(3) \times 10^{-2}$	5.27(6)	10-22	15.0/11.0
100	4.7206	2.08(3)	0.2830(8)	$8.01(5) \times 10^{-2}$	5.38(8)	11-21	2.6/9.0
105	4.9566	2.14(3)	0.2894(8)	$8.38(4) \times 10^{-2}$	5.47(8)	11-21	3.7/9.0
110	5.1926	2.19(3)	0.2955(7)	$8.73(4) \times 10^{-2}$	5.56(7)	11-21	4.9/9.0
120	5.6647	2.29(3)	0.3069(7)	$9.42(4) \times 10^{-2}$	5.75(7)	11-21	8.6/9.0
130	6.1368	2.48(4)	0.3197(9)	0.1022(6)	5.98(10)	12-20	1.3/7.0
140	6.6088	2.56(4)	0.3292(8)	0.1084(5)	6.17(9)	12-20	2.1/7.0
150	7.0809	2.62(3)	0.3377(7)	0.1140(5)	6.36(9)	12-20	3.2/7.0

Table 46. The fitting results of the correlation function \mathcal{C}_{P-S} . The lattice is $\beta = 6.0000$, $V = 16^3 \times 32$, and the configurations of magnetic charge $m_c = 5$ are used.

$\beta = 6.0000, V = 16^3 \times 32$							
$m_c = 5$							
\bar{m}_{ud} [MeV]	$a\bar{m}_{ud}$ $\times 10^{-2}$	$a^4 G_{P-S}$ $\times 10^{-3}$	am_{PS}	$(am_{PS})^2$	af_{PS} $\times 10^{-2}$	FR: t/a	$\frac{\chi^2}{\text{dof}}$
30	1.4162	1.020(15)	0.1450(8)	$2.10(2) \times 10^{-2}$	4.30(9)	6-26	28.2/19.0
35	1.6522	1.138(17)	0.1603(9)	$2.57(3) \times 10^{-2}$	4.34(9)	7-25	14.7/17.0
40	1.8882	1.190(15)	0.1718(7)	$2.95(3) \times 10^{-2}$	4.41(7)	7-25	25.0/17.0
45	2.1243	1.304(19)	0.1852(8)	$3.43(3) \times 10^{-2}$	4.47(8)	8-24	10.1/15.0
50	2.3603	1.353(17)	0.1954(7)	$3.82(3) \times 10^{-2}$	4.55(7)	8-24	15.9/15.0
55	2.5963	1.46(2)	0.2074(9)	$4.30(4) \times 10^{-2}$	4.62(8)	9-23	4.9/13.0
60	2.8324	1.52(2)	0.2166(8)	$4.69(3) \times 10^{-2}$	4.70(8)	9-23	7.5/13.0
65	3.0684	1.564(19)	0.2254(7)	$5.08(3) \times 10^{-2}$	4.78(7)	9-23	11.1/13.0
70	3.3044	1.611(18)	0.2337(7)	$5.46(3) \times 10^{-2}$	4.86(6)	9-23	16.2/13.0
75	3.5404	1.73(3)	0.2441(8)	$5.96(4) \times 10^{-2}$	4.95(8)	10-22	3.8/11.0
80	3.7765	1.79(2)	0.2518(8)	$6.34(4) \times 10^{-2}$	5.03(7)	10-22	5.5/11.0
85	4.0125	1.84(2)	0.2593(7)	$6.72(4) \times 10^{-2}$	5.12(7)	10-22	7.8/11.0
90	4.2485	1.89(2)	0.2664(7)	$7.10(4) \times 10^{-2}$	5.20(7)	10-22	10.9/11.0
95	4.4846	1.94(2)	0.2732(6)	$7.46(3) \times 10^{-2}$	5.29(6)	10-22	14.9/11.0
100	4.7206	2.07(3)	0.2821(8)	$7.96(5) \times 10^{-2}$	5.40(8)	11-21	2.6/9.0
105	4.9566	2.13(3)	0.2885(8)	$8.33(5) \times 10^{-2}$	5.49(8)	11-21	3.6/9.0
110	5.1926	2.18(3)	0.2947(7)	$8.68(4) \times 10^{-2}$	5.58(8)	11-21	4.8/9.0
120	5.6647	2.27(3)	0.3061(7)	$9.37(4) \times 10^{-2}$	5.76(7)	11-21	8.3/9.0
130	6.1368	2.35(2)	0.3164(6)	0.1001(4)	5.95(7)	11-21	13.4/9.0
140	6.6088	2.54(4)	0.3284(8)	0.1078(5)	6.18(9)	12-20	2.0/7.0
150	7.0809	2.60(3)	0.3369(8)	0.1135(5)	6.36(9)	12-20	3.0/7.0

Table 47. The fitting results of the correlation function \mathcal{C}_{P-S} . The lattice is $\beta = 6.1366$, $V = 20^3 \times 40$, and the normal configurations are used.

$\beta = 6.1366, V = 20^3 \times 40$							
Normal conf							
\bar{m}_{ud}	$a\bar{m}_{ud}$	$a^4 G_{P-S}$	am_{PS}	$(am_{PS})^2$	af_{PS}	FR: t/a	$\frac{\chi^2}{\text{dof}}$
30	1.1329	0.438 (8)	0.1211(8)	$1.466(16) \times 10^{-2}$	3.23(8)	8-32	15.8/23.0
35	1.3218	0.464 (7)	0.1314(7)	$1.726(18) \times 10^{-2}$	3.30(7)	8-32	28.3/23.0
40	1.5106	0.512 (8)	0.1430(7)	$2.05(2) \times 10^{-2}$	3.34(6)	9-31	16.8/21.0
45	1.6994	0.536 (7)	0.1520(6)	$2.31(2) \times 10^{-2}$	3.41(6)	9-31	27.3/21.0
50	1.8882	0.587 (9)	0.1624(7)	$2.64(2) \times 10^{-2}$	3.47(6)	10-30	13.5/19.0
55	2.0771	0.611 (8)	0.1705(6)	$2.91(2) \times 10^{-2}$	3.54(5)	10-30	20.9/19.0
60	2.2659	0.664 (10)	0.1800(7)	$3.24(3) \times 10^{-2}$	3.61(6)	11-29	8.7/17.0
65	2.4547	0.690 (9)	0.1873(6)	$3.51(2) \times 10^{-2}$	3.68(6)	11-29	13.1/17.0
70	2.6435	0.716 (9)	0.1942(6)	$3.77(2) \times 10^{-2}$	3.75(5)	11-29	19.3/17.0
75	2.8324	0.773 (11)	0.2027(7)	$4.11(3) \times 10^{-2}$	3.84(6)	12-28	6.8/15.0
80	3.0212	0.801 (11)	0.2091(6)	$4.37(3) \times 10^{-2}$	3.91(6)	12-28	9.9/15.0
85	3.2100	0.829 (10)	0.2151(6)	$4.63(3) \times 10^{-2}$	3.99(5)	12-28	14.0/15.0
90	3.3988	0.855 (10)	0.2209(6)	$4.88(2) \times 10^{-2}$	4.07(5)	12-28	19.6/15.0
95	3.5876	0.919 (13)	0.2284(7)	$5.21(3) \times 10^{-2}$	4.17(6)	13-27	5.7/13.0
100	3.7765	0.946 (12)	0.2337(6)	$5.46(3) \times 10^{-2}$	4.25(6)	13-27	7.9/13.0
105	3.9653	0.973 (12)	0.2388(6)	$5.70(3) \times 10^{-2}$	4.34(6)	13-27	10.7/13.0
110	4.1541	0.997 (11)	0.2436(6)	$5.93(3) \times 10^{-2}$	4.42(6)	13-27	14.2/13.0
120	4.5318	1.087 (15)	0.2544(7)	$6.47(3) \times 10^{-2}$	4.62(7)	14-26	4.3/11.0
130	4.9094	1.129 (14)	0.2624(6)	$6.89(3) \times 10^{-2}$	4.79(6)	14-26	7.0/11.0
140	5.2871	1.160 (13)	0.2695(5)	$7.26(3) \times 10^{-2}$	4.96(6)	14-26	10.5/11.0
150	5.6647	1.179 (12)	0.2755(5)	$7.59(3) \times 10^{-2}$	5.12(6)	14-26	14.8/11.0

Table 48. The fitting results of the correlation function \mathcal{C}_{P-S} . The lattice is $\beta = 6.1366$, $V = 20^3 \times 40$. The configurations of $m_c = 4$ and 5 are used.

$\beta = 6.1366, V = 20^3 \times 40$							
$m_c = 4$							
\bar{m}_{ud} [MeV]	$a\bar{m}_{ud}$ $\times 10^{-2}$	$a^4 G_{P-S}$ $\times 10^{-3}$	am_{PS}	$(am_{PS})^2$ $\times 10^{-2}$	af_{PS} $\times 10^{-2}$	FR: t/a	$\frac{\chi^2}{\text{dof}}$
30	1.1329	0.526(8)	0.1230(7)	1.512(17)	3.43(7)	7-33	28.7/25.0
35	1.3218	0.575(8)	0.1351(7)	1.826(18)	3.47(7)	8-32	21.3/23.0
40	1.5106	0.625(10)	0.1465(7)	2.15(2)	3.52(7)	9-31	13.5/21.0
45	1.6994	0.650(9)	0.1555(6)	2.42(2)	3.58(6)	9-31	22.5/21.0
50	1.8882	0.701(10)	0.1657(7)	2.75(2)	3.64(6)	10-30	11.8/19.0
55	2.0771	0.726(9)	0.1738(6)	3.02(2)	3.71(6)	10-30	18.5/19.0
60	2.2659	0.780(11)	0.1832(7)	3.35(3)	3.77(6)	11-29	8.2/17.0
65	2.4547	0.807(11)	0.1905(6)	3.63(2)	3.84(6)	11-29	12.4/17.0
70	2.6435	0.832(10)	0.1974(6)	3.90(2)	3.91(5)	11-29	18.4/17.0
75	2.8324	0.892(13)	0.2058(7)	4.24(3)	3.99(7)	12-28	6.9/15.0
80	3.0212	0.920(12)	0.2122(6)	4.50(3)	4.07(6)	12-28	10.1/15.0
85	3.2100	0.947(12)	0.2183(6)	4.77(3)	4.14(6)	12-28	14.3/15.0
90	3.3988	0.972(11)	0.2241(6)	5.02(3)	4.22(5)	12-28	19.9/15.0
95	3.5876	1.040(15)	0.2315(7)	5.36(3)	4.32(7)	13-27	6.3/13.0
100	3.7765	1.067(14)	0.2369(6)	5.61(3)	4.40(6)	13-27	8.7/13.0
105	3.9653	1.092(13)	0.2419(6)	5.85(3)	4.48(6)	13-27	11.7/13.0
110	4.1541	1.115(13)	0.2467(6)	6.09(3)	4.56(6)	13-27	15.4/13.0
120	4.5318	1.207(17)	0.2575(7)	6.63(3)	4.75(7)	14-26	5.2/11.0
130	4.9094	1.244(16)	0.2654(6)	7.04(3)	4.92(7)	14-26	8.2/11.0
140	5.2871	1.267(15)	0.2723(6)	7.41(3)	5.08(6)	14-26	12.1/11.0
150	5.6647	1.33(2)	0.2801(7)	7.85(4)	5.27(8)	15-25	2.7/9.0
$m_c = 5$							
30	1.1329	0.555(8)	0.1233(6)	1.521(16)	3.51(7)	7-33	34.7/25.0
35	1.3218	0.605(8)	0.1355(6)	1.836(17)	3.54(7)	8-32	25.5/23.0
40	1.5106	0.656(9)	0.1469(7)	2.16(2)	3.59(6)	9-31	15.7/21.0
45	1.6994	0.679(8)	0.1558(6)	2.428(19)	3.65(6)	9-31	25.8/21.0
50	1.8882	0.731(10)	0.1661(6)	2.76(2)	3.70(6)	10-30	13.1/19.0
55	2.0771	0.754(9)	0.1740(6)	3.03(2)	3.77(5)	10-30	20.6/19.0
60	2.2659	0.808(11)	0.1834(7)	3.36(2)	3.83(6)	11-29	8.7/17.0
65	2.4547	0.834(10)	0.1906(6)	3.63(2)	3.90(6)	11-29	13.5/17.0
70	2.6435	0.858(10)	0.1975(5)	3.90(2)	3.97(5)	11-29	20.2/17.0
75	2.8324	0.917(12)	0.2059(6)	4.24(3)	4.05(6)	12-28	7.3/15.0
80	3.0212	0.944(11)	0.2123(6)	4.51(3)	4.12(6)	12-28	10.8/15.0
85	3.2100	0.969(11)	0.2183(6)	4.77(2)	4.19(5)	12-28	15.6/15.0
90	3.3988	0.994(10)	0.2241(5)	5.02(2)	4.27(5)	12-28	21.9/15.0
95	3.5876	1.061(14)	0.2315(6)	5.36(3)	4.36(6)	13-27	6.8/13.0
100	3.7765	1.087(13)	0.2368(6)	5.61(3)	4.44(6)	13-27	9.4/13.0
105	3.9653	1.111(13)	0.2418(6)	5.85(3)	4.52(6)	13-27	12.9/13.0
110	4.1541	1.133(12)	0.2466(5)	6.08(3)	4.60(5)	13-27	17.1/13.0
120	4.5318	1.223(16)	0.2574(6)	6.62(3)	4.79(7)	14-26	5.7/11.0
130	4.9094	1.258(15)	0.2653(6)	7.04(3)	4.95(6)	14-26	9.2/11.0
140	5.2871	1.280(14)	0.2722(5)	7.41(3)	5.11(6)	14-26	13.9/11.0
150	5.6647	1.344(19)	0.2800(7)	7.84(4)	5.30(8)	15-25	3.2/9.0

F Numerical results of PCAC relation and renormalization constant \hat{Z}_S **Table 49.** The fitting results of the slopes $aA_{\text{PCAC}}^{(1)}$, $aA_{\text{PCAC}}^{(2)}$ and intercept a^2B_{PCAC} by the functions $(am_\pi)^2 = a^2A_{\text{PCAC}}^{(1)}\bar{m}_{ud} + a^2B_{\text{PCAC}}$ and $(am_\pi)^2 = a^2A_{\text{PCAC}}^{(2)}\bar{m}_{ud}$. The calculated results of the renormalization constant \hat{Z}_S for the scalar density.

β	V	m_c	$aA_{\text{PCAC}}^{(1)}$	a^2B_{PCAC} $\times 10^{-3}$	$aA_{\text{PCAC}}^{(2)}$	FR: $a\bar{m}_{ud}$ $\times 10^{-2}$	$\frac{\chi^2}{\text{dof}}$ $(aA^{(1)}, a^2B)$	$\frac{\chi^2}{\text{dof}}$ $(aA^{(2)})$	\hat{Z}_S
5.8457	$12^3 \times 24$	Normal conf	1.955(18)	-6.0(1.0)	1.854(4)	3.7-8.9	11.7/12.0	46.2/12.0	1.16(4)
		0	1.99(2)	-8.6(1.3)	1.833(5)	3.7-7.0	8.4/9.0	52.8/10.0	1.18(4)
		1	1.987(15)	-7.7(7)	1.825(4)	2.5-7.0	13.0/13.0	139.2/14.0	1.18(4)
		2	1.944(16)	-7.1(8)	1.802(4)	2.8-7.0	12.0/12.0	94.1/13.0	1.20(4)
		3	1.89(2)	-7.5(9)	1.728(5)	2.8-6.3	9.6/10.0	75.8/11.0	1.25(4)
		4	1.87(2)	-7.4(1.0)	1.704(5)	2.8-6.3	9.9/10.0	70.3/11.0	1.27(4)
		5	1.83(4)	-7.3(1.4)	1.641(7)	2.8-5.1	6.0/6.0	31.8/7.0	1.32(4)
5.9256	$14^3 \times 28$	Normal conf	1.839(18)	-4.0(8)	1.756(4)	3.2-6.5	10.1/10.0	32.4/11.0	1.05(4)
		0	1.81(2)	-3.2(1.0)	1.743(4)	3.2-5.7	7.6/8.0	17.8/9.0	1.06(4)
		1	1.832(16)	-3.0(7)	1.766(3)	2.9-6.5	11.2/11.0	29.7/12.0	1.05(3)
		2	1.82(2)	-3.1(1.0)	1.750(4)	3.2-5.7	7.9/8.0	17.6/9.0	1.06(4)
		3	1.828(19)	-3.5(8)	1.744(4)	2.6-5.4	9.0/9.0	29.9/10.0	1.06(4)
		4	1.838(16)	-5.2(6)	1.708(4)	2.4-5.4	9.8/10.0	81.3/11.0	1.08(4)
		5	1.835(14)	-4.5(5)	1.710(4)	2.1-5.4	11.1/11.0	94.9/12.0	1.08(4)
6.0000	$14^3 \times 28$	Normal conf	1.862(15)	-4.3(6)	1.761(3)	2.8-6.2	10.7/11.0	59.2/12.0	0.92(3)
		0	1.857(16)	-3.6(7)	1.775(3)	3.0-6.6	9.6/10.0	36.6/11.0	0.91(3)
		1	1.88(2)	-4.9(6)	1.711(5)	1.8-3.8	7.2/7.0	65.7/8.0	0.95(3)
		2	1.853(14)	-3.9(6)	1.764(3)	2.8-6.2	11.4/11.0	52.8/12.0	0.92(3)
		3	1.852(19)	-2.9(8)	1.784(3)	3.0-5.7	9.0/9.0	22.1/10.0	0.91(3)
		4	1.85(2)	-4.0(6)	1.726(4)	2.1-4.1	7.2/7.0	47.4/8.0	0.94(3)
		5	1.880(19)	-5.1(7)	1.750(3)	2.8-5.0	8.0/8.0	55.9/9.0	0.93(3)
	$16^3 \times 32$	Normal conf	1.711(14)	-1.4(5)	1.676(3)	2.5-5.2	10.2/10.0	17.1/11.0	0.97(3)
		0	1.725(11)	-3.0(4)	1.644(3)	2.1-5.2	11.9/12.0	70.0/13.0	0.98(3)
		1	1.711(9)	-2.5(3)	1.644(3)	1.6-5.2	14.6/14.0	69.9/15.0	0.99(3)
		2	1.725(17)	-1.8(7)	1.679(3)	2.6-5.2	9.5/9.0	17.5/10.0	0.96(3)
		3	1.718(17)	-1.2(7)	1.689(3)	2.8-5.2	9.4/9.0	12.4/10.0	0.96(3)
		4	1.713(17)	-1.3(6)	1.679(3)	2.5-4.8	8.0/8.0	12.0/9.0	0.96(3)
		5	1.710(18)	-1.6(7)	1.670(3)	2.8-5.0	7.9/8.0	13.2/9.0	0.97(3)
		6.1366	$20^3 \times 40$	Normal conf	1.505(15)	-2.0(4)	1.434(3)	1.7-3.6	8.1/8.0
4	1.518(15)			-1.1(4)	1.482(3)	2.0-3.8	8.0/8.0	13.8/9.0	0.87(3)
5	1.514(12)			-9(3)	1.482(3)	1.8-3.8	9.3/9.0	16.8/10.0	0.87(3)

G Fitting results of aF_{PS} and $(am_{PS})^2$ and the computed results of intersections aF_{PS}^π and am_{PS}^π

Table 50. The fitting results of the slope $a^{-1}A_{PS}$ and intercept aB_{PS} by the function $aF_{PS} = a^{-1}A_{PS}x + aB_{PS}$, [$x = (am_{PS})^2$] together with the computed results of the intersections aF_{PS}^π and am_{PS}^π .

β	V	m_c	$a^{-1}A_{PS}$	aB_{PS} $\times 10^{-2}$	$FR : (am_{PS})^2$ $\times 10^{-2}$	$\frac{\chi^2}{\text{dof}}$	aF_{PS}^π $\times 10^{-2}$	am_{PS}^π $\times 10^{-2}$		
5.8457	$12^3 \times 24$	N. C.	0.174(9)	4.60(9)	4.2-17.6	3.9/17.0	4.69(9)	7.09(14)		
		0	0.171(8)	4.66(9)	4.7-17.6	5.2/16.0	4.75(9)	7.19(14)		
		1	0.174(9)	4.69(10)	4.8-17.6	3.1/16.0	4.79(10)	7.24(15)		
		2	0.170(10)	4.85(10)	4.2-16.2	1.9/16.0	4.94(11)	7.47(16)		
		3	0.174(10)	4.87(10)	4.0-15.8	1.3/16.0	4.96(10)	7.51(15)		
5.9256	$14^3 \times 28$	N. C.	0.205(7)	3.89(6)	2.9-13.9	11.0/18.0	3.96(7)	6.00(10)		
		0	0.206(7)	3.90(6)	2.9-13.8	9.6/18.0	3.97(6)	6.01(10)		
		1	0.197(8)	3.99(6)	2.9-13.2	8.0/17.0	4.07(7)	6.15(10)		
		2	0.191(8)	4.17(7)	2.9-13.1	6.5/17.0	4.24(7)	6.42(11)		
		3	0.192(10)	4.20(8)	3.0-12.3	2.2/16.0	4.28(8)	6.47(12)		
		4	0.188(8)	4.28(7)	2.9-13.0	5.1/17.0	4.36(7)	6.60(11)		
6.0000	$14^3 \times 28$	N. C.	0.218(7)	3.26(5)	2.9-12.4	12.1/17.0	3.31(5)	5.01(8)		
		0	0.214(7)	3.24(5)	2.9-9.8	6.8/16.0	3.29(6)	4.98(8)		
		1	0.211(8)	3.34(6)	3.0-9.8	4.8/16.0	3.39(6)	5.13(9)		
		2	0.209(7)	3.50(5)	2.9-12.4	9.9/17.0	3.57(5)	5.39(8)		
		3	0.197(8)	3.60(6)	2.6-9.1	3.6/16.0	3.66(6)	5.54(9)		
		4	0.192(8)	3.70(5)	2.6-9.0	3.0/16.0	3.76(6)	5.69(9)		
	$16^3 \times 32$	N. C.	0.240(7)	3.30(5)	2.1-9.4	15.6/19.0	3.37(5)	5.09(7)		
		0	0.242(8)	3.31(5)	2.5-9.3	10.4/17.0	3.37(6)	5.10(9)		
		1	0.240(8)	3.37(6)	2.9-9.4	8.8/17.0	3.44(6)	5.20(10)		
		2	0.230(8)	3.53(5)	2.5-9.5	12.2/18.0	3.60(6)	5.45(9)		
		3	0.229(8)	3.60(6)	2.5-9.5	10.5/18.0	3.67(6)	5.55(9)		
		4	0.211(8)	3.70(5)	2.2-10.3	5.6/17.0	3.77(6)	5.70(8)		
		5	0.219(8)	3.69(5)	2.5-10.8	7.9/17.0	3.76(5)	5.69(8)		
		6.1366	$20^3 \times 40$	N. C.	0.292(8)	2.69(4)	1.4-7.3	18.9/18.0	2.74(4)	4.15(6)
				4	0.265(9)	2.92(4)	1.5-7.1	12.2/17.0	2.98(4)	4.50(7)
5	0.260(9)			3.00(4)	1.5-7.1	13.7/17.0	3.05(4)	4.62(6)		

H The numerical results of the observables

Table 51. The outcomes of the decay constant F_0 , renormalized chiral condensate $\langle\bar{\psi}\psi\rangle^{\overline{\text{MS}}}$ and average mass of light quarks $\hat{m}_{ud}^{\overline{\text{MS}}}$ in the $\overline{\text{MS}}$ -scheme at 2 [GeV], pion mass m_π and decay constant F_π , and ratios of the decay constants $\frac{F_\pi}{F_0}$. The predictions of these observables are indicated as Pre1 for $V_{\text{phys}} = 5.7845$ [fm⁴] and Pre2 for $V_{\text{phys}} = 9.8582$ [fm⁴] in the column of β .

β	V	m_c	F_0 [MeV]	$\langle\bar{\psi}\psi\rangle^{\overline{\text{MS}}}$ [GeV ³] $\times 10^{-2}$	$\hat{m}_{ud}^{\overline{\text{MS}}}$ [MeV]	m_π [MeV] $\times 10^2$	F_π [MeV]	$\frac{F_\pi}{F_0}$
Pre1	-	N. C.	85.366	-2.0280	$3.5_{-0.7}^{+0.3}$	1.395706(2)	92.28(8)	1.0810(9)
		1	88.666	-2.1878	$3.8_{-0.8}^{+0.3}$	1.449656(2)	95.84(9)	1.0809(10)
		2	91.634	-2.3367	$4.0_{-0.8}^{+0.3}$	1.498178(2)	99.05(9)	1.0809(10)
		3	94.338	-2.4766	$4.3_{-0.9}^{+0.4}$	1.542397(2)	101.98(9)	1.0810(10)
		4	96.828	-2.6091	$4.5_{-0.9}^{+0.4}$	1.583109(2)	104.67(10)	1.0810(10)
		5	99.140	-2.7352	$4.7_{-0.9}^{+0.4}$	1.620903(2)	107.17(10)	1.0810(10)
Pre2	-	N. C.	85.366	-2.0280	$3.5_{-0.7}^{+0.3}$	1.395706(2)	92.28(9)	1.0810(11)
		1	87.345	-2.1231	$3.7_{-0.3}^{+0.7}$	1.428069(2)	94.42(9)	1.0810(10)
		2	89.199	-2.2142	$3.8_{-0.3}^{+0.8}$	1.458370(2)	96.42(9)	1.0810(10)
		3	90.943	-2.3016	$4.0_{-0.3}^{+0.8}$	1.486892(2)	98.31(9)	1.0810(10)
		4	92.593	-2.3859	$4.1_{-0.4}^{+0.8}$	1.513862(2)	100.09(9)	1.0810(10)
		5	94.159	-2.4672	$4.3_{-0.4}^{+0.9}$	1.539462(2)	101.78(9)	1.0809(10)
5.8457	$12^3 \times 24$	N. C.	91(3)	-1.95(13)	4.1(3)	1.40(4)	92(3)	1.02(3)
		0	92(3)	-2.01(13)	4.2(3)	1.42(4)	94(3)	1.02(3)
		1	93(3)	-2.03(14)	4.3(3)	1.43(4)	94(3)	1.02(3)
		2	95(3)	-2.17(14)	4.6(3)	1.47(4)	97(3)	1.02(3)
		3	96(3)	-2.19(14)	4.6(3)	1.48(4)	98(3)	1.02(3)
		5.9256	$14^3 \times 28$	N. C.	91(2)	-1.95(11)	4.1(2)	1.40(3)
0	91(2)	-1.96(11)		4.1(2)	1.40(3)	92(2)	1.02(2)	
1	93(2)	-2.05(12)		4.3(3)	1.43(3)	95(2)	1.02(2)	
2	97(2)	-2.24(13)		4.7(3)	1.49(4)	99(2)	1.02(2)	
3	98(2)	-2.27(14)		4.8(3)	1.51(4)	100(3)	1.02(3)	
4	100(2)	-2.36(13)		5.0(3)	1.54(4)	102(2)	1.02(2)	
6.0000	$14^3 \times 28$	N. C.	91(2)	-1.96(11)	4.1(2)	1.40(3)	92(2)	1.02(2)
		0	90(2)	-1.94(11)	4.0(2)	1.39(3)	92(2)	1.02(2)
		1	93(2)	-2.06(12)	4.3(3)	1.43(3)	95(2)	1.02(3)
		2	98(2)	-2.27(12)	4.7(3)	1.50(3)	99(2)	1.02(2)
		3	100(2)	-2.40(13)	5.0(3)	1.54(4)	102(2)	1.02(2)
		4	103(2)	-2.52(14)	5.3(3)	1.58(3)	105(2)	1.02(2)
		5	103(2)	-2.54(13)	5.3(3)	1.59(3)	105(2)	1.017(18)
	$16^3 \times 32$	N. C.	90.6(1.8)	-1.95(10)	4.1(2)	1.40(3)	92(2)	1.02(2)
		0	91(2)	-1.96(11)	4.1(2)	1.40(3)	92(2)	1.02(2)
		1	92(2)	-2.03(12)	4.3(2)	1.42(3)	94(2)	1.02(3)
		2	97(2)	-2.23(12)	4.7(3)	1.49(3)	99(2)	1.02(2)
		3	99(2)	-2.31(12)	4.9(3)	1.52(3)	101(2)	1.02(2)
		4	101(2)	-2.47(13)	5.1(3)	1.56(3)	103(2)	1.02(2)
		5	101(2)	-2.44(13)	5.1(3)	1.56(3)	103(2)	1.02(2)
6.1366	$20^3 \times 40$	N. C.	90.6(1.8)	-1.95(10)	4.1(2)	1.40(3)	92.3(1.9)	1.02(2)
		4	98(2)	-2.30(12)	4.8(3)	1.51(3)	100(2)	1.02(2)
		5	101(2)	-2.42(12)	5.1(3)	1.55(3)	103(2)	1.02(2)

References

1. Millennium Problems, 2000. Clay Mathematics Institute, Peterborough, New Hampshire, USA, <http://www.claymath.org/millennium-problems>.
2. S. Mandelstam. II. Vortices and quark confinement in non-Abelian gauge theories. *Phys. Rep.*, 23:245, 1976.
3. G. 't Hooft. 1976. in Proceedings of the EPS International, edited by A. Zichichi, p. 1225.
4. A. S. Kronfeld, G. Schierholz, and U. -J. Wiese. Topology and dynamics of the confinement mechanism. *Nucl. Phys. B*, 293:461, 1987.
5. S. Maedan and T. Suzuki. An Infrared Effective Theory of Quark Confinement Based on Monopole Condensation. *Prog. Theor. Phys.*, 81(1):229, 1989.
6. F. Brandstaeter, G. Schierholz, and U. -J. Wiese. Color confinement, abelian dominance and the dynamics of magnetic monopoles in SU (3) gauge theory. *Phys. Lett.*, B272:319, 1991.
7. S. Hioki, S. Kitahara, S. Kiura, Y. Matsubara, O. Miyamura, S. Ohno, and T. Suzuki. Abelian dominance in SU (2) color confinement. *Phys. Lett.*, B272:326, 1991.
8. V. Bornyakov and G. Schierholz. Instantons or monopoles? Dyons. *Phys. Lett.*, B384:190, 1996.
9. A. Di Giacomo and G. Paffuti. A disorder parameter for dual superconductivity in gauge theories. *Phys. Rev. D*, 56:6816, 1997.
10. S. Kitahara, Y. Matsubara, and T. Suzuki. Deconfinement Transition and Monopoles in $T \neq 0$ SU(2) QCD. *Prog. Theor. Phys.*, 93:1, 1995.
11. S. Sasaki and O. Miyamura. Lattice Study of $U_A(1)$ Anomaly: The Role of QCD-Monopoles. *Phys. Lett.*, B443:331, 1998.
12. S. Sasaki and O. Miyamura. Topological Aspect of Abelian Projected SU(2) Lattice Gauge Theory. *Phys. Rev. D*, 59:094507, 1999.
13. A. Di Giacomo, B. Lucini, L. Montesi, and G. Paffuti. Colour confinement and dual superconductivity of the vacuum - I. *Phys. Rev. D*, 61:034503, 2000.
14. A. Di Giacomo, B. Lucini, L. Montesi, and G. Paffuti. Colour confinement and dual superconductivity of the vacuum - II. *Phys. Rev. D*, 61:034504, 2000.
15. V. G. Bornyakov, H. Ichie, Y. Koma, Y. Mori, Y. Nakamura, D. Pleiter, M. I. Polikarpov, G. Schierholz, T. Streuer, H. Stüben, and T. Suzuki. Dynamics of Monopoles and Flux Tubes in Two-Flavor Dynamical QCD. *Phys. Rev. D*, 70:074511, 2004.
16. M. W. Ray, E. Ruokokoski, S. Kandel, M. Möttönen, and D. S. Hall. Observation of Dirac monopoles in a synthetic magnetic field. *Nature*, 505:657, 2014.
17. M. W. Ray, E. Ruokokoski, K. Tiurev, M. Möttönen, and D. S. Hall. Observation of isolated monopoles in a quantum field. *Science*, 348(6234):544, 2015.
18. B. Acharya, and et. al. Search for magnetic monopoles with the MoEDAL prototype trapping detector in 8 TeV proton-proton collisions at the LHC. *J. of High Energy Phys.*, 08:067, 2016.
19. B. Acharya, and et. al. Search for Magnetic Monopoles with the MoEDAL Forward Trapping Detector in 13 TeV Proton-Proton Collisions at the LHC. *Phys. Rev. Lett.*, 118:061801, 2017.
20. Y. Nambu. Quasi-Particles and Gauge Invariance in the Theory of Superconductivity. *Phys. Rev.*, 117:648, 1960.
21. Y. Nambu and G. Jona-Lasinio. Dynamical Model of Elementary Particles Based on an Analogy with Superconductivity. I. *Phys. Rev.*, 122:345, 1961.
22. J. Goldstone. Field theories with Superconductor solutions. *Nuovo Cim.*, 19:154, 1961.
23. J. Goldstone, A. Salam, and S. Weinberg. Broken Symmetries. *Phys. Rev.*, 127:965, 1962.
24. D. J. Gross and A. Neveu. Dynamical symmetry breaking in asymptotically free field theories. *Phys. Rev. D*, 10:3235, 1974.
25. T. Kugo. *The quantum theory of the gauge field I, II*. Baifukan, 2002. The textbook written in Japanese.
26. S. Weinberg. PION SCATTERING LENGTHS. *Phys. Rev. Lett.*, 17:616, 1966.
27. A. A. Belavin, A. M. Polyakov, A. S. Schwartz, and Yu. S. Tyupkin. Pseudoparticle solutions of the Yang-Mills equations. *Phys. Lett.*, B59:85, 1975.
28. D. Diakonov. Instantons at work. *Prog. Particle and Nuclear Physics*, 51:173, 2003.
29. T. Schäfer and E. V. Shuryak. Instantons in QCD. *Rev. Mod. Phys.*, 70(2):323, 1998.
30. D. I. Dyakonov and V. Yu. Petrov. CHIRAL CONDENSATE IN THE INSTANTON VACUUM. *Phys. Lett.*, 147B(4, 5):351, 1984.
31. D. I. D'yakonov and V. Yu. Petrov. Meson-current correlation function in instanton vacuum. *Sov. Phys. JETP*, 62(3):431, 1985.
32. D. I. D'yakonov and V. Yu. Petrov. Quark propagator and chiral condensate in an instanton vacuum. *Sov. Phys. JETP*, 62(2):204, 1985.
33. D. I. Dyakonov and V. Yu. Petrov. A theory of light quarks in the instanton vacuum. *Nucl. Phys. B*, 272:457, 1986.
34. P. H. Ginsparg and K. G. Wilson. A remnant of chiral symmetry on the lattice. *Phys. Rev. D*, 25:2649, 1982.
35. H. Neuberger. Exactly massless quarks on the lattice. *Phys. Lett. B*, 417:141, 1998.
36. H. Neuberger. More about exactly massless quarks on the lattice. *Phys. Lett. B*, 427:353, 1998.
37. M. Lüscher. Exact chiral symmetry on the lattice and the Ginsparg-Wilson relation. *Phys. Lett.*, B428:342, 1998.
38. S. Chandrasekharan. Lattice QCD with Ginsparg-Wilson fermions. *Phys. Rev. D*, 60:074503, 1999.
39. A. Di Giacomo and M. Hasegawa. Instantons and monopoles. *Phys. Rev. D*, 91:054512, 2015.
40. S. Necco and R. Sommer. The $N_f=0$ heavy quark potential from short to intermediate distances. *Nucl. Phys. B*, 622:328, 2002.
41. M. Hasegawa. Monopole and instanton effects in QCD. *J. High Energy Phys.*, 09(113), 2020.
42. A. Di Giacomo and M. Hasegawa. Chiral symmetry breaking, instantons, and monopoles. 2015. *Proc. Sci.*, Lat2015, 313, [hep-lat/1512.00359].
43. M. Hasegawa. Instanton effects on chiral symmetry breaking and hadron spectroscopy. *arXiv: 2201.00431*, 2022.
44. G. 't Hooft. TOPOLOGY OF THE GAUGE CONDITION AND NEW CONFINEMENT PHASES IN NON-ABELIAN GAUGE THEORIES. *Nucl. Phys. B*, 190:455, 1981.
45. A. Bode, T. Lippert, and K. Schilling. Monopole clusters and critical dynamics in four-dimensional U(1). *Nucl. Phys. B, Proc. Suppl.*, 34:549, 1994.
46. T. A. DeGrand and D. Toussaint. Topological excitations and Monte Carlo simulation of Abelian gauge theory. *Phys. Rev. D*, 22:2478, 1980.

47. S. Kitahara, O. Miyamura, T. Okude, F. Shoji, and T. Suzuki. Monopoles and hadron spectrum in quenched QCD. *Nucl. Phys. B*, 533:576, 1998.
48. L. Giusti, C. Hölbling, M. Lüscher, and H. Wittig. Numerical techniques for lattice QCD in the ϵ -regime. *Comp. Phys. Comm.*, 153:31, 2003.
49. L. Giusti, M. Lüscher, P. Weisz, and H. Wittig. Lattice QCD in the ϵ -regime and random matrix theory. *J. High Energy Phys.*, 11:023, 2003.
50. E. P. Wigner. Group Theory and its Application to the Quantum Mechanics of Atomic Spectra. *Academic press, New York*, 1959.
51. F. J. Dyson and M. L. Mehta. Statistical Theory of the Energy Levels of Complex Systems. IV. *J. Math. Phys.*, 4:701, 1963.
52. S. Capitani, C. Gökeler, R. Horsley, P. E. L. Rakow, and G. Schierholz. Operator improvement for Ginsparg–Wilson fermions. *Phys. Lett. B*, 468:150, 1999.
53. T. Guhr, J.-Z. Ma, S. Meyer, and T. Wilke. Statistical analysis and the equivalent of a Thouless energy in lattice QCD Dirac spectra. *Phys. Rev. D*, 59:054501, 1999.
54. T. Guhr, A. Müller–Groeling, and H. A. Weidenmüller. Random-matrix theories in quantum physics: common concepts. *Physics Reports*, 299:189–428, 1998.
55. O. Bohigas and M. J. Giannoni. Chaotic motion and random matrix theories. *Mathematical and Computational Methods in Nuclear Physics*, 209(Part of the Lecture Notes in Physics book series):1–99, 1984 (First Online: 31 May 2005).
56. P. H. Damgaard S. M. Nishigaki and T. Wettig. Smallest Dirac eigenvalue distribution from random matrix theory. *Phys. Rev. D*, 58:087704, 1998.
57. S. M. Nishigaki, P. H. Damgaard, and T. Wettig. Smallest Dirac eigenvalue distribution from random matrix theory. *Phys. Rev. D*, 58:087704, 1998.
58. T. Blum, P. Chen, N. Christ, C. Cristian, C. Dawson, G. Fleming, A. Kaehler, X. Liao, G. Liu, C. Malureanu, R. Mawhinney, S. Ohta, G. Siebert, A. Soni, C. Sui, P. Vranas, M. Wingate, L. Wu, and Y. Zhestkov. Quenched lattice QCD with domain wall fermions and the chiral limit. *Phys. Rev. D*, 69:074502, 2004.
59. L. Giusti, C. Hölbling, and C. Rebbi. Light quark masses with overlap fermions in quenched QCD. *Phys. Rev. D*, 64:114508, 2001. Erratum, *Phys. Rev. D* **65**, 079903(E) (2002).
60. P. Hernández, K. Jansen, L. Lellouch, and H. Wittig. Non-perturbative renormalization of the quark condensate in Ginsparg–Wilson regularizations. *J. High Energy Phys.*, 07:018, 2001.
61. J. Wennekers and H. Wittig. On the renormalized scalar density in quenched QCD. *J. High Energy Phys.*, 09:059, 2005.
62. C. R. Allton, V. Giménez, L. Giusti, and F. Rapuano. Light quenched hadron spectrum and decay constants on different lattices. *Nucl. Phys. B*, 489:427, 1997.
63. G. Colangelo and E. Pallante. Quenched chiral perturbation theory to one loop. *Nucl. Phys. B*, 520:433, 1998.
64. L. Giusti, P. Hernández, M. Laine, P. Weisz, and H. Wittig. Low-energy couplings of QCD from current correlations near the chiral limit. *J. High Energy Phys.*, 04:013, 2004.
65. L. Giusti, P. Hernández, S. Necco, C. Pena, J. Wennekers, and H. Wittig. Testing chiral effective theory with quenched lattice QCD. *J. High Energy Phys.*, 05:024, 2008.
66. C. Patrignani et al., (Particle Data Group). REVIEW OF PARTICLE PHYSICS. *Chin. Phys. C*, 40:100001, 2016. updated in 2017.
67. Murray Gell-Mann, R. J. Oakes, and B. Renner. Behavior of Current Divergences under $SU_3 \times SU_3$. *Phys. Rev.*, 175:2195, 1968.
68. G. Colangelo and S. Dürr. The pion mass in finite volume. *Eur. Phys. J. C*, 33:543, 2004.
69. Ape Collaboration, M. Albanese, and et al. Glueball masses and string tension in lattice QCD. *Phys. Lett.*, B 192:163, 1987.
70. S. Necco. *The static quark potential and scaling behavior of $SU(3)$ lattice Yang-Mills theory*. Ph. D. thesis, Humboldt Universität zu Berlin, DESY, Platanenallee 6, D-15738 Zeuthen, Germany, June 2003. [hep-lat/0306005].

